Measurement of neutrino and antineutrino oscillations by the T2K experiment including a new additional sample of ν_e interactions at the far detector

K. Abe,[45] J. Amey,[15] C. Andreopoulos,[43,25] M. Antonova,[20] S. Aoki,[22] A. Ariga,[1] Y. Ashida,[23] S. Ban,[23] M. Barbi,[37] G. J. Barker,[53] G. Barr,[33] C. Barry,[25] M. Batkiewicz,[11] V. Berardi,[16] S. Berkman,[3,49] S. Bhadra,[57] S. Bienstock,[34] A. Blondel,[10] S. Bolognesi,[5] S. Bordoni,[13,*] S. B. Boyd,[53] D. Brailsford,[24] A. Bravar,[10] C. Bronner,[45] M. Buizza Avanzini,[9] R. G. Calland,[21] T. Campbell,[7] S. Cao,[12] S. L. Cartwright,[41] M. G. Catanesi,[16] A. Cervera,[14] A. Chappell,[53] C. Checchia,[18] D. Cherdack,[7] N. Chikuma,[44] G. Christodoulou,[25] J. Coleman,[25] G. Collazuol,[18] D. Coplowe,[33] A. Cudd,[27] A. Dabrowska,[11] G. De Rosa,[17] T. Dealtry,[24] P. F. Denner,[53] S. R. Dennis,[25] C. Densham,[43] F. Di Lodovico,[36] S. Dolan,[33] O. Drapier,[9] K. E. Duffy,[33] J. Dumarchez,[34] P. Dunne,[15] S. Emery-Schrenk,[5] A. Ereditato,[1] T. Feusels,[3,49] A. J. Finch,[24] G. A. Fiorentini,[57] G. Fiorillo,[17] M. Friend,[12,†] Y. Fujii,[12,†] D. Fukuda,[31] Y. Fukuda,[28] A. Garcia,[13] C. Giganti,[34] F. Gizzarelli,[5] T. Golan,[55] M. Gonin,[9] D. R. Hadley,[53] L. Haegel,[10] J. T. Haigh,[53] D. Hansen,[35] J. Harada,[32] M. Hartz,[21,49] T. Hasegawa,[12,†] N. C. Hastings,[37] T. Hayashino,[23] Y. Hayato,[45,21] A. Hillairet,[50] T. Hiraki,[23] A. Hiramoto,[23] S. Hirota,[23] M. Hogan,[7] J. Holeczek,[42] F. Hosomi,[44] K. Huang,[23] A. K. Ichikawa,[23] M. Ikeda,[45] J. Imber,[9] J. Insler,[26] R. A. Intonti,[16] T. Ishida,[12,†] T. Ishii,[12,†] E. Iwai,[12] K. Iwamoto,[44] A. Izmaylov,[14,20] B. Jamieson,[54] M. Jiang,[23] S. Johnson,[6] P. Jonsson,[15] C. K. Jung,[30,‡] M. Kabirnezhad,[29] A. C. Kaboth,[39,43] T. Kajita,[46,‡] H. Kakuno,[47] J. Kameda,[45] D. Karlen,[50,49] T. Katori,[36] E. Kearns,[2,21,‡] M. Khabibullin,[20] A. Khotjantsev,[20] H. Kim,[32] J. Kim,[3,49] S. King,[36] J. Kisiel,[42] A. Knight,[53] A. Knox,[24] T. Kobayashi,[12,†] L. Koch,[40] T. Koga,[44] P. P. Koller,[1] A. Konaka,[49] L. L. Kormos,[24] Y. Koshio,[31,‡] K. Kowalik,[29] Y. Kudenko,[20,§] R. Kurjata,[52] T. Kutter,[26] J. Lagoda,[29] I. Lamont,[24] M. Lamoureux,[5] P. Lasorak,[36] M. Laveder,[18] M. Lawe,[24] M. Licciardi,[9] T. Lindner,[49] Z. J. Liptak,[6] R. P. Litchfield,[15] X. Li,[30] A. Longhin,[18] J. P. Lopez,[6] T. Lou,[44] L. Ludovici,[19] X. Lu,[33] L. Magaletti,[16] K. Mahn,[27] M. Malek,[41] S. Manly,[38] L. Maret,[10] A. D. Marino,[6] J. F. Martin,[48] P. Martins,[36] S. Martynenko,[30] T. Maruyama,[12,†] V. Matveev,[20] K. Mavrokoridis,[25] W. Y. Ma,[15] E. Mazzucato,[5] M. McCarthy,[57] N. McCauley,[25] K. S. McFarland,[38] C. McGrew,[30] A. Mefodiev,[20] C. Metelko,[25] M. Mezzetto,[18] A. Minamino,[56] O. Mineev,[20] S. Mine,[4] A. Missert,[6] M. Miura,[45,‡] S. Moriyama,[45,‡] J. Morrison,[27] Th. A. Mueller,[9] T. Nakadaira,[12,†] M. Nakahata,[45,21] K. G. Nakamura,[23] K. Nakamura,[21,12,†] K. D. Nakamura,[23] Y. Nakanishi,[23] S. Nakayama,[45,‡] T. Nakaya,[23,21] K. Nakayoshi,[12,†] C. Nantais,[48] C. Nielsen,[3,49] K. Nishikawa,[12,†] Y. Nishimura,[46] P. Novella,[14] J. Nowak,[24] H. M. O'Keeffe,[24] K. Okumura,[46,21] T. Okusawa,[32] W. Oryszczak,[51] S. M. Oser,[3,49] T. Ovsyannikova,[20] R. A. Owen,[36] Y. Oyama,[12,†] V. Palladino,[17] J. L. Palomino,[30] V. Paolone,[35] N. D. Patel,[23] P. Paudyal,[25] M. Pavin,[34] D. Payne,[25] Y. Petrov,[3,49] L. Pickering,[15] E. S. Pinzon Guerra,[57] C. Pistillo,[1] B. Popov,[34,‖] M. Posiadala-Zezula,[51] J.-M. Poutissou,[49] A. Pritchard,[25] P. Przewlocki,[29] B. Quilain,[23] T. Radermacher,[40] E. Radicioni,[16] P. N. Ratoff,[24] M. A. Rayner,[10] E. Reinherz-Aronis,[7] C. Riccio,[17] P. A. Rodrigues,[38] E. Rondio,[29] B. Rossi,[17] S. Roth,[40] A. C. Ruggeri,[17] A. Rychter,[52] K. Sakashita,[12,†] F. Sánchez,[13] E. Scantamburlo,[10] K. Scholberg,[8,‡] J. Schwehr,[7] M. Scott,[49] Y. Seiya,[32] T. Sekiguchi,[12,†] H. Sekiya,[45,21,‡] D. Sgalaberna,[10] R. Shah,[43,33] A. Shaikhiev,[20] F. Shaker,[54] D. Shaw,[24] M. Shiozawa,[45,21] T. Shirahige,[31] M. Smy,[4] J. T. Sobczyk,[55] H. Sobel,[4,21] J. Steinmann,[40] T. Stewart,[43] P. Stowell,[41] Y. Suda,[44] S. Suvorov,[20] A. Suzuki,[22] S. Y. Suzuki,[12,†] Y. Suzuki,[21] R. Tacik,[37,49] M. Tada,[12,†] A. Takeda,[45] Y. Takeuchi,[22,21] R. Tamura,[44] H. K. Tanaka,[45,‡] H. A. Tanaka,[48,49,¶] T. Thakore,[26] L. F. Thompson,[41] S. Tobayama,[3,49] W. Toki,[7] T. Tomura,[45] T. Tsukamoto,[12,†] M. Tzanov,[26] M. Vagins,[21,4] Z. Vallari,[30] G. Vasseur,[5] C. Vilela,[30] T. Vladisavljevic,[33,21] T. Wachala,[11] C. W. Walter,[8,‡] D. Wark,[43,33] M. O. Wascko,[15] A. Weber,[43,33] R. Wendell,[23,‡] M. J. Wilking,[30] C. Wilkinson,[1] J. R. Wilson,[36] R. J. Wilson,[7] C. Wret,[15] Y. Yamada,[12,†] K. Yamamoto,[32] C. Yanagisawa,[30,**] T. Yano,[22] S. Yen,[49] N. Yershov,[20] M. Yokoyama,[44,‡] M. Yu,[57] A. Zalewska,[11] J. Zalipska,[29] L. Zambelli,[12,†] K. Zaremba,[52] M. Ziembicki,[52] E. D. Zimmerman,[6] and M. Zito[5]

(The T2K Collaboration)

[1]*University of Bern, Albert Einstein Center for Fundamental Physics, Laboratory for High Energy Physics (LHEP), Bern, Switzerland*
[2]*Boston University, Department of Physics, Boston, Massachusetts, USA*
[3]*University of British Columbia, Department of Physics and Astronomy, Vancouver, British Columbia, Canada*
[4]*University of California, Irvine, Department of Physics and Astronomy, Irvine, California, USA*
[5]*IRFU, CEA Saclay, Gif-sur-Yvette, France*

[6]*University of Colorado at Boulder, Department of Physics, Boulder, Colorado, USA*
[7]*Colorado State University, Department of Physics, Fort Collins, Colorado, USA*
[8]*Duke University, Department of Physics, Durham, North Carolina, USA*
[9]*Ecole Polytechnique, IN2P3-CNRS, Laboratoire Leprince-Ringuet, Palaiseau, France*
[10]*University of Geneva, Section de Physique, DPNC, Geneva, Switzerland*
[11]*H. Niewodniczanski Institute of Nuclear Physics PAN, Cracow, Poland*
[12]*High Energy Accelerator Research Organization (KEK), Tsukuba, Ibaraki, Japan*
[13]*Institut de Fisica d'Altes Energies (IFAE), The Barcelona Institute of Science and Technology, Campus UAB, Bellaterra (Barcelona) Spain*
[14]*IFIC (CSIC & University of Valencia), Valencia, Spain*
[15]*Imperial College London, Department of Physics, London, United Kingdom*
[16]*INFN Sezione di Bari and Università e Politecnico di Bari, Dipartimento Interuniversitario di Fisica, Bari, Italy*
[17]*INFN Sezione di Napoli and Università di Napoli, Dipartimento di Fisica, Napoli, Italy*
[18]*INFN Sezione di Padova and Università di Padova, Dipartimento di Fisica, Padova, Italy*
[19]*INFN Sezione di Roma and Università di Roma "La Sapienza", Roma, Italy*
[20]*Institute for Nuclear Research of the Russian Academy of Sciences, Moscow, Russia*
[21]*Kavli Institute for the Physics and Mathematics of the Universe (WPI), The University of Tokyo Institutes for Advanced Study, University of Tokyo, Kashiwa, Chiba, Japan*
[22]*Kobe University, Kobe, Japan*
[23]*Kyoto University, Department of Physics, Kyoto, Japan*
[24]*Lancaster University, Physics Department, Lancaster, United Kingdom*
[25]*University of Liverpool, Department of Physics, Liverpool, United Kingdom*
[26]*Louisiana State University, Department of Physics and Astronomy, Baton Rouge, Louisiana, USA*
[27]*Michigan State University, Department of Physics and Astronomy, East Lansing, Michigan, USA*
[28]*Miyagi University of Education, Department of Physics, Sendai, Japan*
[29]*National Centre for Nuclear Research, Warsaw, Poland*
[30]*State University of New York at Stony Brook, Department of Physics and Astronomy, Stony Brook, New York, USA*
[31]*Okayama University, Department of Physics, Okayama, Japan*
[32]*Osaka City University, Department of Physics, Osaka, Japan*
[33]*Oxford University, Department of Physics, Oxford, United Kingdom*
[34]*UPMC, Université Paris Diderot, CNRS/IN2P3, Laboratoire de Physique Nucléaire et de Hautes Energies (LPNHE), Paris, France*
[35]*University of Pittsburgh, Department of Physics and Astronomy, Pittsburgh, Pennsylvania, USA*
[36]*Queen Mary University of London, School of Physics and Astronomy, London, United Kingdom*
[37]*University of Regina, Department of Physics, Regina, Saskatchewan, Canada*
[38]*University of Rochester, Department of Physics and Astronomy, Rochester, New York, USA*
[39]*Royal Holloway University of London, Department of Physics, Egham, Surrey, United Kingdom*
[40]*RWTH Aachen University, III. Physikalisches Institut, Aachen, Germany*
[41]*University of Sheffield, Department of Physics and Astronomy, Sheffield, United Kingdom*
[42]*University of Silesia, Institute of Physics, Katowice, Poland*
[43]*STFC, Rutherford Appleton Laboratory, Harwell Oxford, and Daresbury Laboratory, Warrington, United Kingdom*
[44]*University of Tokyo, Department of Physics, Tokyo, Japan*
[45]*University of Tokyo, Institute for Cosmic Ray Research, Kamioka Observatory, Kamioka, Japan*
[46]*University of Tokyo, Institute for Cosmic Ray Research, Research Center for Cosmic Neutrinos, Kashiwa, Japan*
[47]*Tokyo Metropolitan University, Department of Physics, Tokyo, Japan*
[48]*University of Toronto, Department of Physics, Toronto, Ontario, Canada*
[49]*TRIUMF, Vancouver, British Columbia, Canada*
[50]*University of Victoria, Department of Physics and Astronomy, Victoria, British Columbia, Canada*
[51]*University of Warsaw, Faculty of Physics, Warsaw, Poland*
[52]*Warsaw University of Technology, Institute of Radioelectronics, Warsaw, Poland*
[53]*University of Warwick, Department of Physics, Coventry, United Kingdom*
[54]*University of Winnipeg, Department of Physics, Winnipeg, Manitoba, Canada*

[55]Wroclaw University, Faculty of Physics and Astronomy, Wroclaw, Poland
[56]Yokohama National University, Faculty of Engineering, Yokohama, Japan
[57]York University, Department of Physics and Astronomy, Toronto, Ontario, Canada
(Received 5 July 2017; published 21 November 2017)

The T2K experiment reports an updated analysis of neutrino and antineutrino oscillations in appearance and disappearance channels. A sample of electron neutrino candidates at Super-Kamiokande in which a pion decay has been tagged is added to the four single-ring samples used in previous T2K oscillation analyses. Through combined analyses of these five samples, simultaneous measurements of four oscillation parameters, $|\Delta m^2_{32}|$, $\sin^2\theta_{23}$, $\sin^2\theta_{13}$, and δ_{CP} and of the mass ordering are made. A set of studies of simulated data indicates that the sensitivity to the oscillation parameters is not limited by neutrino interaction model uncertainty. Multiple oscillation analyses are performed, and frequentist and Bayesian intervals are presented for combinations of the oscillation parameters with and without the inclusion of reactor constraints on $\sin^2\theta_{13}$. When combined with reactor measurements, the hypothesis of CP conservation ($\delta_{\mathrm{CP}} = 0$ or π) is excluded at 90% confidence level. The 90% confidence region for δ_{CP} is $[-2.95, -0.44]$ ($[-1.47, -1.27]$) for normal (inverted) ordering. The central values and 68% confidence intervals for the other oscillation parameters for normal (inverted) ordering are $\Delta m^2_{32} = 2.54 \pm 0.08 (2.51 \pm 0.08) \times 10^{-3}$ eV$^2/c^4$ and $\sin^2\theta_{23} = 0.55^{+0.05}_{-0.09}$ ($0.55^{+0.05}_{-0.08}$), compatible with maximal mixing. In the Bayesian analysis, the data weakly prefer normal ordering (Bayes factor 3.7) and the upper octant for $\sin^2\theta_{23}$ (Bayes factor 2.4).

DOI: 10.1103/PhysRevD.96.092006

I. INTRODUCTION

Neutrino oscillations have been firmly established by multiple experiments. Super-Kamiokande (SK) observed an energy and path length dependent deficit in the atmospheric muon neutrino flux [1], and Sudbury Neutrino Observatory resolved the long-standing solar neutrino problem by demonstrating that the previously observed deficit of electron neutrinos from the Sun was due to flavor transitions [2]. These two experiments, together with accelerator-based (K2K [3] and MINOS [4]) and reactor-based (KamLAND [5]) long-baseline experiments measured the two mass-squared differences between mass eigenstates and two of the three mixing angles in the Pontecorvo-Maki-Nakagawa-Sakata (PMNS) matrix.

The mixing angle, θ_{13}, has been measured as nonzero by T2K [6,7], by reactor experiments [8–10], and more recently by NOνA [11]. Establishing that all three mixing angles are nonzero opens a way to study CP violation in the leptonic sector through neutrino oscillations. CP violation in neutrino oscillations arises from δ_{CP}, an irreducible CP-odd phase in the PMNS matrix. This phase introduces a difference in the appearance probability between neutrinos and antineutrinos. To investigate this phenomenon, after taking data with a beam predominantly composed of muon neutrinos in order to observe the appearance of electron neutrinos at the far detector, T2K switched to taking data with a beam predominantly composed of muon antineutrinos. A direct measurement of CP violation can then be obtained by comparing $\nu_\mu \to \nu_e$ and $\bar{\nu}_\mu \to \bar{\nu}_e$ channels.

To produce neutrinos, protons extracted from the Japan Proton Accelerator Research Complex (J-PARC) main ring strike a target producing hadrons which are then focused and selected by charge with a system of magnetic horns. The hadrons decay in flight, producing an intense neutrino beam. A beam predominantly composed of neutrinos or antineutrinos can be produced by choosing the direction of the current in the magnetic horn. T2K uses the so-called off-axis technique with the beam axis directed 2.5° away from SK in order to produce a narrow-band neutrino beam, peaked at an energy of 600 MeV, where the effect of neutrino oscillations is maximum for a baseline of 295 km. Neutrinos are also observed at a near detector complex, installed 280 m from the target, comprising an on-axis detector (INGRID), which provides day-to-day monitoring of the beam profile and direction, and a magnetized off-axis detector (ND280), at the same off-axis angle as SK, which measures neutrino interaction rates before oscillation.

The analyses described in this paper are based on an exposure of 7.482×10^{20} protons on target (POT) in the

[*]Now at CERN.
[†]Also at J-PARC, Tokai, Japan.
[‡]Affiliated member at Kavli IPMU (WPI), the University of Tokyo, Japan.
[§]Also at National Research Nuclear University "MEPhI" and Moscow Institute of Physics and Technology, Moscow, Russia.
[‖]Also at JINR, Dubna, Russia.
[¶]Also at Institute of Particle Physics, Canada.
[**]Also at BMCC/CUNY, Science Department, New York, New York, USA.

TABLE I. T2K data-taking periods and collected POT used in the analyses presented in this paper.

Run period	Dates	ν-mode POT ($\times 10^{20}$)	$\bar{\nu}$-mode POT ($\times 10^{20}$)
Run 1	Jan. 2010–Jun. 2010	0.323	···
Run 2	Nov. 2010–Mar. 2011	1.108	···
Run 3	Mar. 2012–Jun. 2012	1.579	···
Run 4	Oct. 2012–May 2013	3.560	···
Run 5	May 2014–Jun. 2014	0.242	0.506
Run 6	Nov. 2014–Jun. 2015	0.190	3.505
Run 7	Feb. 2016–May 2016	0.480	3.460
Total	Jan. 2010–May 2016	7.482	7.471

neutrino mode (ν-mode) and 7.471×10^{20} POT in the antineutrino mode ($\bar{\nu}$-mode) collected at SK during seven physics runs as detailed in Table I. The neutrino oscillation parameters are measured by combining ν_μ and $\bar{\nu}_\mu$ disappearance channels with ν_e and $\bar{\nu}_e$ appearance channels, using the same analysis techniques described in Ref. [12]. The analyzed data set is the same as in Ref. [12], but an additional SK sample is included in the oscillation analysis. Previously, for the appearance channel, only the SK single-ring e-like interactions without additional activity in the detector were used for the oscillation analysis. The analysis presented in this paper includes an additional sample enriched in ν_e interactions in which the e-like ring is accompanied by a delayed Michel electron due to the decay chain $\pi^+ \to \mu^+ \to e^+$ of π^+'s produced in the neutrino interactions. This sample is currently only used in the ν mode and increases the statistics of the ν_e sample in SK by roughly 10%.

The paper is organized as follows. The neutrino beam and the modeling of the neutrino fluxes are described in Sec. II. The neutrino interaction model developed for this analysis will then be described in Sec. III, followed by the selection of neutrinos in the near detector complex in Sec. IV. The neutrino flux and neutrino interaction inputs and the near detector selections are combined to reduce flux and cross section uncertainties at the far detector as will be shown in Sec. V. The far detector selections are described in Sec. VI. The neutrino oscillations and the T2K oscillation analyses frameworks are then described in Secs. VII and in VIII respectively. Section IX is dedicated to a description of the impact of the uncertainties of the neutrino interaction model on the T2K oscillation analyses. Finally, the results of the oscillation analyses are presented in Secs. X and in XI, and some concluding remarks are given in Sec. XII.

II. T2K BEAM

The neutrino beam is produced by the interaction of 30 GeV protons from the J-PARC main ring accelerator on a 1.9 interaction-length graphite target. Secondary hadrons, mainly pions and kaons, leaving the target pass through three electromagnetic horns [13], which are operated at a current of either +250 kA or −250 kA to focus positively or negatively charged particles respectively. The outgoing hadrons decay in a 96-m-long decay volume, where a relatively pure beam of muon neutrinos is produced by the decay of positively charged hadrons in the positive focusing mode (ν mode), and a beam mostly composed of muon antineutrinos is produced in the negative focusing mode $\bar{\nu}$ mode). Protons and undecayed hadrons are stopped in a beam dump, while muons above 5 GeV pass through and are detected in a muon monitor (MUMON [14]) and are used to monitor the secondary beam stability. The T2K beamline hardware has been described in detail elsewhere [15].

The T2K neutrino flux at the near and far detectors in case of no neutrino oscillation is predicted by a simulation which has been described in detail in Ref. [16]. Interactions of the primary proton beam, the profile of which is measured for each run period by a suite of proton beam monitors, as well as subsequently produced pions and kaons, are simulated within the graphite target by the FLUKA2011 package [17,18]. The predicted hadron production rates inside and outside the target are then adjusted based on the results from the latest analysis of the full 2009 thin-target data set by the NA61/SHINE experiment [19–21] as well as other hadron production experiments [22–24]. Particles which exit the target and subsequently decay are tracked through the horns and decay volume by a GEANT3 [25] simulation using the GCALOR [26] package. The predicted (anti)neutrino fluxes at the far detector for T2K Run 1–7 is shown for both ν and $\bar{\nu}$ modes in Fig. 1.

Most of the "right-sign" ν_μ flux (i.e. ν's in the ν mode and $\bar{\nu}$'s in the $\bar{\nu}$ mode) comes from mesons produced inside the target, dominantly right-sign (focused) pion and kaon production, which subsequently decay to produce muons. Interactions producing right-sign ν_e's also predominantly come from interactions in the target, with a larger fraction of ν_e produced by kaon (rather than pion) decays. Interactions producing the "wrong-sign" ν_μ flux have a higher fractional rate of out-of-target interactions, which are dominated by protons, neutrons, and pions scattering in the horns and decay volume walls. Interactions producing the wrong-sign ν_e flux have a significant fraction of K^0 production from proton or neutron interactions as well as charged kaon production.

In general, the ν- and $\bar{\nu}$-mode fluxes are similar at low energy, although the right-sign ν_μ (and ν_e) flux in the ν mode is ∼15% higher around the flux peak than the right-sign $\bar{\nu}_\mu$ (and $\bar{\nu}_e$) flux in the $\bar{\nu}$ mode. The wrong-sign background $\bar{\nu}$ flux is also lower in the ν mode compared to the ν flux in the $\bar{\nu}$ mode, especially at high energy. These differences are due to the higher production multiplicities of positive, rather than negative, parent particles.

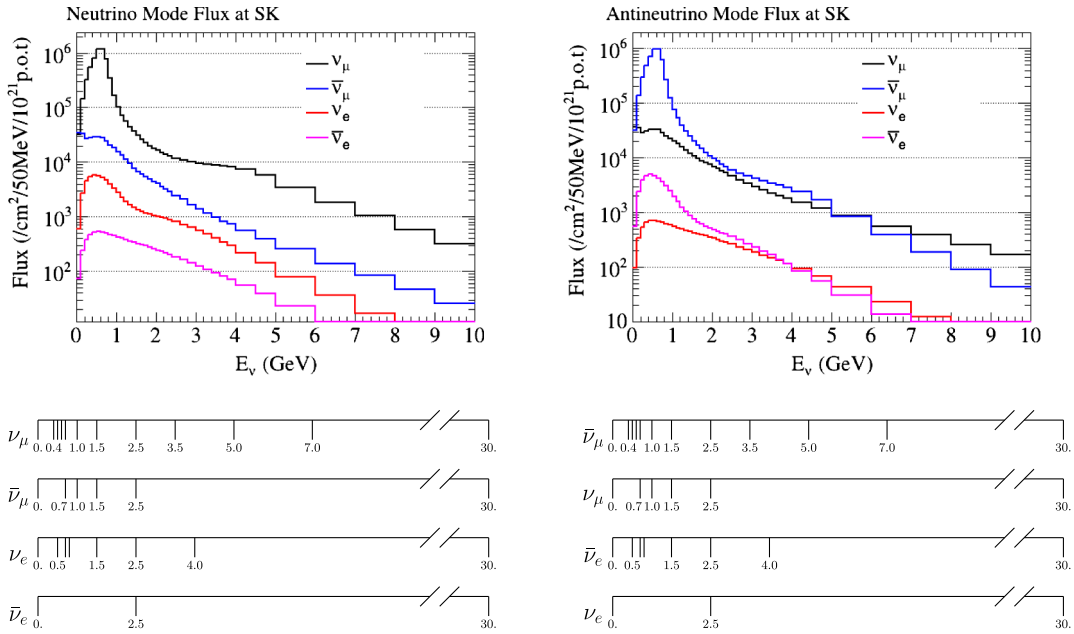

FIG. 1. The T2K unoscillated neutrino flux prediction at SK for ν (left) and $\bar{\nu}$ (right) modes. The binning used for the flux systematic parameters is also shown.

Uncertainties in the neutrino flux prediction arise from the hadron production model, proton beam profile, off-axis angle, horn current, horn alignment, and other factors. For each source of error, the underlying parameters in the model are varied to evaluate the effect on the flux prediction in bins of neutrino energy for each neutrino flavor as described in detail elsewhere [16]. The uncertainties on the unoscillated ν_μ and $\bar{\nu}_\mu$ beam fluxes at the far detector are shown in Fig. 2 and are currently dominated by uncertainties on hadron production. The uncertainties on the background ν_e and $\bar{\nu}_e$ fluxes from the beam are 7%–10% in the relevant region.

III. NEUTRINO INTERACTION MODEL

The neutrino interaction model used in this analysis is based on NEUT [28] version 5.3.2, which includes many significant improvements over the old version 5.1.4.2, used in previous T2K oscillation analyses (described in detail in Ref. [27]). This model is constrained where possible by external experiments that are used to provide initial cross section parameter uncertainties. Such uncertainties are reduced using ND280 data, as explained in Sec. V. Alternative models are used to build simulated data sets to test the robustness of the T2K analysis against model-dependent assumptions, as explained in Sec. IX. This section describes the updated NEUT interaction model and alternative models used for the oscillation analyses.

A. Neutrino interaction model used in the oscillation analyses

The interaction rate at T2K energies is dominated by charged current quasielastic (CCQE) events, $\nu_l n \to l^- p$ ($\bar{\nu}_{lp} \to l^+ n$). Because CCQE is a two-body process and the neutrino direction is known, the neutrino energy can be reconstructed from the outgoing lepton kinematics alone. However, nuclear effects and other processes, which have the same experimental signature of a single muon and no final state pions (CC0π or CCQE-like), are indistinguishable from CCQE and can affect the reconstructed neutrino energy and thus the oscillation result if not accounted for [29–34]. The T2K cross section modeling has been updated to include recent theoretical models of these processes (full details can be found in Ref. [35]). In previous analyses, the CCQE model was based on the Llewellyn-Smith neutrino-nucleon scattering model [36] with a dipole axial form factor and BBBA05 vector form factors [37] and used the Smith-Moniz relativistic Fermi gas (RFG) model [38] to account for the fact that the nucleons are bound in a nucleus. The main improvements available in NEUT version 5.3.2 are the inclusion of the spectral function (SF) model from Ref. [39], which provides a more sophisticated description of the initial state of the nucleus than the RFG, the inclusion of the multinucleon interaction (2p2h) model from Refs. [40,41], and the implementation of the random phase approximation (RPA) correction from Ref. [40]. The 2p2h model includes interactions with more than one nucleon bound within the nucleus, which contribute considerable strength to the CCQE-like cross section and add significant smearing to the reconstructed neutrino energy distribution (as it is not a two-body process). RPA is a nuclear screening effect due to long-range nucleon-nucleon correlations which modifies the interaction strength as a function of four-momentum transfer, Q^2. The models make different physical assumptions,

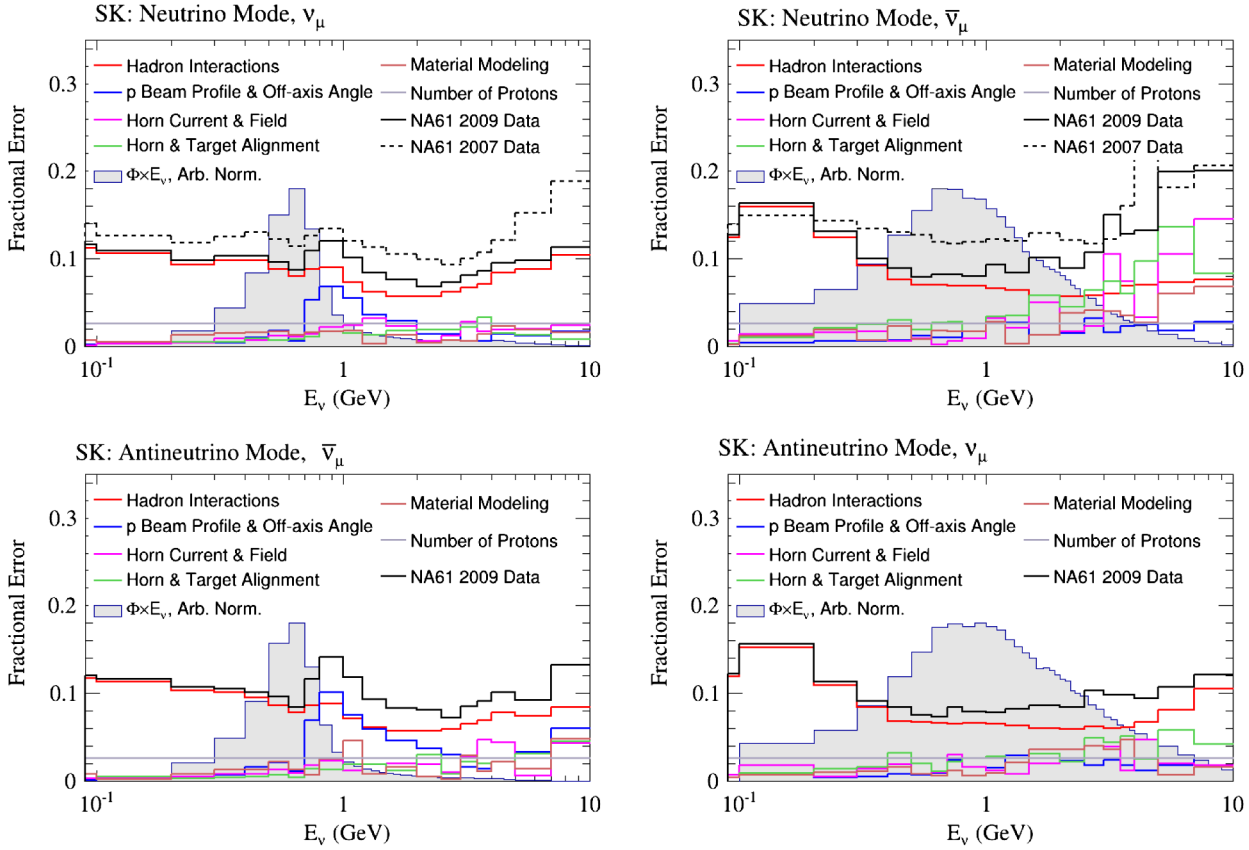

FIG. 2. The T2K fractional systematic uncertainties on the SK flux arising from the beamline configuration and hadron production prior to constraints from near detector data. Uncertainties are given for ν's in a ν-mode beam (top left), $\bar{\nu}$'s in a ν-mode beam (top right), $\bar{\nu}$'s in an $\bar{\nu}$-mode beam (bottom left), and ν's in an $\bar{\nu}$-mode beam (bottom right). For the ν-mode plots, the total current uncertainties (NA61 2009 data) are compared to the total uncertainties estimated for the previous T2K results (NA61 2007 data) [27].

so they cannot be combined arbitrarily. Two candidate models were considered for the default model: SF and RFG + RPA + 2p2h. RFG + RPA + 2p2h was selected as the default because it was most consistently able to describe the available MiniBooNE [42,43] and MINERvA [44,45] CCQE-like data (see Ref. [35] for details).

Various parameters have been introduced to describe the theoretical uncertainties and approximations in the RFG + RPA + 2p2h model, which are constrained using the near detector data. The variable parameters are the axial mass, M_A; the Fermi momentum, p_F; the binding energy, E_b; and the 2p2h cross section normalization. Given the poor agreement between the MINERvA and MiniBooNE data sets [35] and slight inconsistencies between the signal definitions from the two experiments, no external constraints are applied on the variable parameters prior to the ND280 fit. Given the absence of firm predictions on the scaling of various nuclear effects with the nucleus mass number, the Fermi momentum, binding energy, and 2p2h normalization are treated as uncorrelated between ^{12}C and ^{16}O. The 2p2h normalization is also considered to be uncorrelated between neutrino and antineutrino interactions. All of these parameters can be separately constrained by the T2K near detector data with the inclusion of samples with interactions on both ^{12}C and on ^{16}O, with ν- and $\bar{\nu}$-mode data.

The NEUT model for resonant pion production is based on the Rein-Sehgal model [46] with updated nucleon form factors [47] and with the invariant hadronic mass restricted to be $W \leq 2$ GeV to avoid double-counting pions produced through deep inelastic scattering (DIS). Three variable model parameters are considered: the resonant axial mass, M_A^{RES}; the value of the axial form factor at zero transferred 4-momentum, C_5^A; and the normalization of the isospin nonresonant component predicted in the Rein-Sehgal model, $I\frac{1}{2}$. Initial central values and uncertainties for these parameters are obtained in a fit to low energy neutrino-deuterium single pion production data from Argonne National Laboratory [48] and Brookhaven National Laboratory [49] for the resonant pion production channels $\nu_\mu p \to \mu^- p\pi^+$, $\nu_\mu n \to \mu^- p\pi^0$ and $\nu_\mu n \to \mu^- n\pi^+$. For the dominant production channel, $\nu_\mu p \to \mu^- p\pi^+$, the reanalyzed data set from Ref. [50] was used. Resonant kaon, photon, and eta production is also modeled using the Rein-Sehgal resonance production amplitudes, with modified branching ratios to account for the decay of the

resonances to kaons, photons, or eta, rather than to pions. External neutrino-nucleus and antineutrino-nucleus pion production data from MiniBooNE [51–53], MINERvA [54], SciBooNE [55], and K2K [56] were used as a cross-check to ensure that the broad features of all data sets were consistent with the uncertainties on the interaction level parameters (M_A^{RES}, C_5^A, and $I\frac{1}{2}$ component) or the uncertainties on final state interactions (FSI) (which will be described shortly). A full fit to the external data is difficult due to strong correlations between FSI parameters and the neutrino-nucleus interaction model parameters and a lack of information on the correlations between external data points.

The coherent pion production model used is the Rein-Sehgal model described in Refs. [57,58]. However, recent results from MINERvA [59] are better described by the Berger-Sehgal model [60], so a rough reweighting of the coherent events as a function of the outgoing pion energy, E_π, is applied to approximate the Berger-Sehgal model using the weights and binning given in Table II. Normalization uncertainties of 30% are introduced separately for charged current (CC)- and neutral current (NC)-coherent events, based on comparisons to the MINERvA data (after the weights in Table II are applied), which are fully correlated between ^{12}C and ^{16}O.

The DIS model is unchanged from previous analyses (described in Ref. [27]). The DIS cross section is calculated for $W \geq 1.3$ GeV, using GRV98 structure functions [61] with Bodek-Yang corrections [62]. Single pion production through DIS is suppressed for $W \leq 2$ GeV to avoid double-counting with the resonant pion production contributions and uses a custom hadronization model described in Ref. [28]. For $W > 2$ GeV, PYTHIA/JETSET [63] is used for hadronization. A CC-other shape parameter, $x^{\text{CC-Other}}$, was introduced to give flexibility to the CC-DIS contribution. This parameter applies to CC resonant kaon, photon, and eta production, as well as CC-DIS events, and it scales the cross section by $(1 + x^{\text{CC-Other}}/E_\nu)$. It was designed to give greater flexibility at low E_ν, and the initial uncertainty was set by NEUT comparisons with MINOS CC-inclusive data [64].

In addition to the previously described NC-coherent parameter, two other NC-specific parameters have been introduced in this analysis. A study in Ref. [65] showed that the NEUT neutral current single photon production (NC1γ) cross section prediction was approximately a factor of 2 smaller than a recent theoretical model [66]. Because of this, the NC1γ cross section has been set to be 200% of the NEUT nominal prediction, with an uncertainty of 100%. An NC-other normalization parameter is applied to neutral current elastic, NC resonant kaon and eta production, as well as NC-DIS events, with an initial uncertainty set at 30%.

TABLE II. Weights applied to coherent pion interactions as a function of the pion energy, E_π.

E_π (GeV)	Weight
0.00–0.25	0.135
0.25–0.50	0.400
0.50–0.75	0.294
0.75–1.00	1.206

Hadrons produced inside the nucleus may undergo FSI before leaving the nuclear environment, which changes the outgoing particle content and kinematics in the final state. NEUT models FSI for pions, kaons, etas, and nucleons using a cascade model described in Ref. [28]. Interactions are generated inside the nucleus according to a Woods-Saxon density distribution [67], and all outgoing hadrons are stepped through the nucleus with interaction probabilities calculated at each step until they leave the nucleus. Particles produced in DIS interactions are propagated some distance without interacting to allow for a formation zone, where the initial step size is based on results from the SKAT experiment [68]. The allowed pion interactions in the nucleus are charge exchange, where the charge of the pion changes; absorption, where the pion is absorbed through two- or three-body processes; elastic scattering, where the pion only exchanges momentum and energy; and inelastic scattering, where additional pions are produced. If an interaction occurs, new and modified particles are also added to the cascade. For pion momenta $p_\pi \geq 500$ MeV, nucleons are treated as free particles, and separate high ($p_\pi \geq 500$ MeV) and low ($p_\pi < 500$ MeV) energy scattering parameters are introduced for charge exchange and elastic scattering. Initial interaction uncertainties are obtained from fits to a large body of pion-nucleon and pion-nucleus scattering data for nuclei ranging from carbon to lead, as described in Ref. [27]. The variable parameters included to vary the pion FSI cross section are summarized in Table IX. Pion FSI parameters are assumed to be fully correlated between ^{12}C and ^{16}O. Uncertainties on nucleon, kaon, and eta FSI interaction probabilities are not considered in the current analysis.

To account for effects which may potentially affect $\overset{(-)}{\nu}_e$ but not $\overset{(-)}{\nu}_\mu$ cross sections, such as radiative corrections or second class currents (see, for example, Ref. [69]), which are not included in the NEUT cross section model, additional uncertainties which affect $\overset{(-)}{\nu}_e$ have been introduced. These include an uncorrelated 2% uncertainty on the ν_e/ν_μ and $\bar{\nu}_e/\bar{\nu}_\mu$ cross section ratios to account for radiative corrections and an additional 2% uncertainty which is fully anticorrelated between ν_e and $\bar{\nu}_e$ to allow for second class currents.

The full list of cross section uncertainties and their values before and after the ND280 data constraints is provided in Table. IX.

B. Alternative neutrino interaction models for studies of simulated data

Neutrino interactions with ^{12}C and ^{16}O nuclear targets at the near and far detectors may be affected by important nuclear effects which are not well understood. Various theoretical models are available to describe such effects, which are based on different approximations and with different ranges of validity. None of the available models is capable of describing all the available measurements of neutrino-nucleus cross sections from T2K and from other experiments. It is therefore crucial to test that the T2K oscillation analysis is insensitive to reasonable modifications of the neutrino interaction model described in Sec. III A, which will now be referred to as the "reference model." With this aim, various simulated data sets have been built based on alternative models. The following effects have been considered: variations of the distribution of the momentum of the initial nucleons in the nucleus and of the energy needed to extract the nucleons from the nucleus (the binding energy); uncertainties on the long-range nuclear correlations modifying the cross section as a function of Q^2; and modifications of the modeling of multinucleon interactions (2p2h), including short-range nuclear correlations and meson exchange currents.

To test the nuclear effects in the initial state, two alternative models have been considered beyond the RFG simulation used as reference: the SF developed in Ref. [39] and the local Fermi gas (LFG) model from Ref. [40]. The LFG model also differs from the reference model in the implementation of the binding energy. In the latter, an effective value is considered, based on the average momentum of nucleons within the nucleus, while the LFG model considers the different state of the initial and final nucleus after the nucleon ejection, naturally including a different binding energy for neutrino and antineutrino interactions. The simulated data sets built with this alternative model will be referred to as the "alternative 1p1h model".

The correction to the CCQE cross section due to long-range nuclear correlations, described by RPA in the reference model, has been parametrized as a function of Q^2 in terms of five free parameters. A joint fit to the MiniBooNE [42,43] and MINERvA [44,45] ν_μ and $\bar{\nu}_\mu$ data sets has been performed to extract an alternative, data-driven RPA correction, labeled "effective RPA" in the following. The effective-RPA correction deviates from the reference RPA at high Q^2, as can be seen in Fig. 3.

The model in Ref. [70] has been considered as an alternative 2p2h model, which differs from the reference model in many respects. The alternative 2p2h cross section is twice as large for neutrino interactions but has a similar strength for antineutrino interactions, except at high neutrino energies ($E_\nu \gtrsim 1$ GeV) where it is about 30% larger, as can be seen in Fig. 4. The difference between the 2p2h normalization for neutrino and antineutrino interactions is

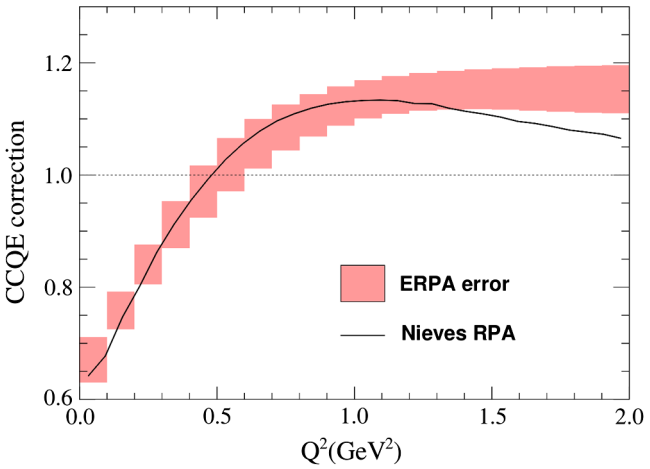

FIG. 3. Effective RPA with error band from the fit to external data compared with RPA corrections computed in Ref. [40].

constrained with the ND280 data in order to avoid biases in the *CP* asymmetry measurement in the oscillation analysis. The alternative model has also been used for one of the studies of simulated data. Another important difference between the two models consists in the relative proportion of nucleon-nucleon correlations, meson exchange currents, and their interference, the first being strongly enhanced in the alternative model. This difference affects the estimation of the neutrino energy from the outgoing lepton kinematics. This estimation assumes the CCQE hypothesis, and it is well known that the 2p2h contribution biases the neutrino energy reconstruction [30,31] if not properly taken into account in the simulation. The reference model includes 2p2h events, and so this effect is included in the T2K neutrino oscillation analysis. Nevertheless, the different 2p2h components produce different biases in the neutrino energy estimation, as shown in Fig. 5. Incorrectly estimating the relative proportion of nucleon-nucleon correlations

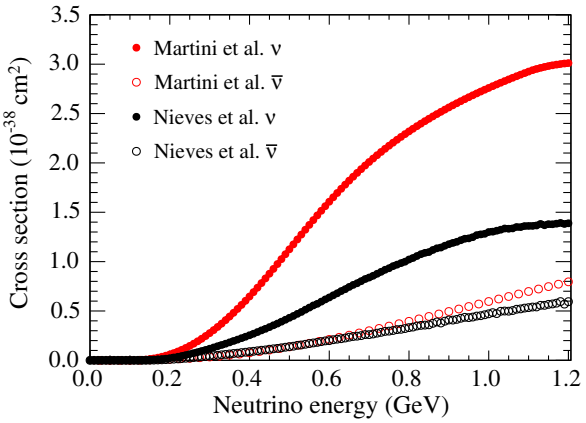

FIG. 4. Multinucleon interactions (2p2h) cross section on ^{12}C as a function of energy from the models of Nieves (reference model in the text) [40] and Martini (alternative model in the text) [70].

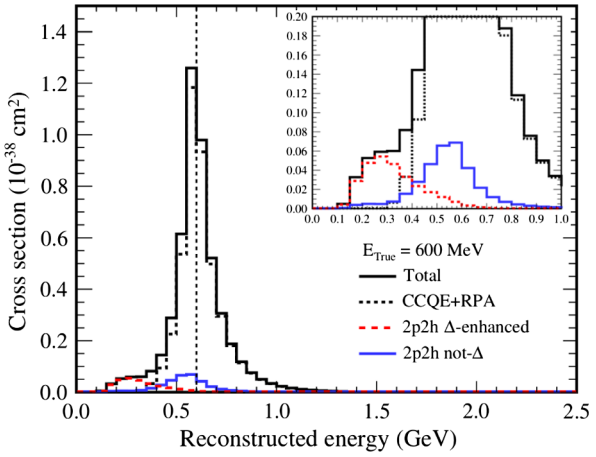

FIG. 5. Neutrino energy calculated with the CCQE two-body assumption for CCQE and 2p2h interactions of 600 MeV muon neutrinos on ^{12}C simulated with the reference model. The different components of 2p2h show differing amounts of bias.

and meson exchange current can cause a residual bias in the neutrino energy estimation. To address this, three simulated data sets have been built. In the first, the multinucleon interactions have been reweighted as a function of neutrino energy, separately for the neutrino and antineutrino, to reproduce the alternative model (referred to as the "alternative 2p2h model" in the following). In the other two simulated data sets, the full 2p2h cross section has been assigned either to meson exchange currents ("Delta-enhanced 2p2h") or nucleon-nucleon correlations only ("not-Delta 2p2h") by reweighting the muon kinematics as a function of the muon angle, muon momentum, and neutrino energy.

The results obtained by considering all the alternative models, SF, alternative 1p1h, effective RPA, alternative 2p2h, Delta-enhanced 2p2h, and not-Delta 2p2h, are shown in Sec. IX.

IV. ND280 COMPLEX

The precise measurement of neutrino oscillations in T2K requires a good understanding of the neutrino beam properties and of neutrino interactions. The two previous sections have described the neutrino flux model and neutrino-nucleus interaction model and constraints on those models based on external measurements. As we will show in Sec. VIII D, with only that information, the precision on the measurements of neutrino oscillations parameters would be limited. In order to reduce the model uncertainties, a near detector complex has been built 280 m downstream of the production target. The goal of the near detectors is to directly measure the neutrino beam properties and the neutrino interaction rate. The near detector complex comprises an on-axis detector (INGRID) and an off-axis detector (ND280). INGRID is composed of a set of modules with sufficient target mass and transverse extent to monitor the beam direction and profile on a day-to-day basis. The ND280 is composed of a set of subdetectors, installed inside a magnet, and is able to measure the products of neutrino interactions in detail.

In this section, the methods used to select high purity samples of neutrino and antineutrino interactions in INGRID and ND280 will be described, and the results are compared with the predictions obtained from the beam line simulation and the interaction models. The use of the ND280 data to reduce the systematic uncertainties in the T2K oscillation analysis will be described in Sec. V.

A. On-axis near detector

The INGRID detector is used to monitor the neutrino beam rate, profile, and center. Those parameters are used to determine the off-axis angle at SK. INGRID is centered on the neutrino beam axis and samples the neutrino beam with a transverse cross section of 10m × 10 m using 14 modules positioned in the shape of a cross. Each INGRID module holds 11 tracking segments built from pairs of orthogonally oriented scintillator planes interleaved with nine iron planes. There are also three veto planes, located on the top, bottom, and one side of each module. The most upstream tracking plane is used as a front veto plane. The scintillator planes are built from 24 plastic scintillator bars instrumented with fibers connected to multipixel photon counters (MPPCs) to detect scintillation light. More details can be found in Ref. [71].

1. Event selection and corrections

Neutrino and antineutrino interactions within INGRID modules are first reconstructed independently in the horizontal and vertical layers of scintillators. Pairs of tracks in the two different orientations are then matched by comparing the most upstream point to form three-dimensional (3D) tracks. The upstream edges of the different 3D tracks are then compared in the longitudinal and transverse direction with respect to the beam direction in order to construct a common vertex. The subsequent reconstructed event is rejected if the vertex is reconstructed out of the fiducial volume, if the external veto planes have hits within 8 cm from the upstream extrapolated position of a reconstructed track or if the event timing deviates from more than 100 ns to the expected event timing.

In order to reduce the systematic uncertainty on the track reconstruction in the $\bar{\nu}$ mode, the selection has been improved from the one used in Ref. [27]. To reduce the impact of MPPC dark noise, the reconstruction is only applied to events where two consecutive tracking planes have a hit coincidence on their horizontal and vertical planes. This condition was not used in Ref. [27] and has been applied only to the $\bar{\nu}$ mode in the analyses presented here. A total of 12.8×10^6 and 4.1×10^6 neutrino events are reconstructed respectively in the ν and $\bar{\nu}$ modes, with estimated purities of 99.6% and 98.0% respectively.

The selected number of events in each module is corrected to take into account the impact of the detector dead channels, the event loss due to nonreconstructed neutrino interactions caused by pileup, the variation of the iron mass between the modules, the time variation of the MPPC noise during the data taking, and the contamination from external background as the previous INGRID analysis [27,71].

2. Systematic uncertainties

The systematic uncertainties on the event selection are estimated using the simulation and control samples. The sources of error are the same as those identified in Ref. [27] and include the neutrino target mass, the accidental coincidence with MPPC dark noise, the hit efficiency, the event pileup, and the cosmic and beam-induced backgrounds along with errors associated to event selection cuts. The method for estimating the uncertainty has not been changed since Ref. [27] for the ν mode and is also applied here for $\bar{\nu}$-mode data. The uncertainties are evaluated to be 0.9% and 1.7% for neutrino and antineutrino data respectively. The larger uncertainty in the $\bar{\nu}$ mode mainly arises from a discrepancy between data and simulation for interactions producing a track that cross less than four tracking planes.

3. Results of neutrino beam measurement

The stability of the neutrino flux is monitored by measuring the event rate, that is the total number of selected events per protons on target. Figure 6 shows the intensity stability as a function of time for both the ν and $\bar{\nu}$ modes. Most of the data have been taken with the horn currents set to an absolute value of 250 kA, except for a small fraction of ν-mode data taken during T2K run 3 in which horns were operated at 205 kA. The average event rates are compared with the simulation, and the ratios are

$$\begin{aligned}
\frac{N^{\mathrm{data},\nu}_{250kA}}{N^{\mathrm{MC},\nu}_{250kA}} &= 1.010 \pm 0.001(\mathrm{stat.}) \pm 0.009(\mathrm{syst.}),\\
\frac{N^{\mathrm{data},\nu}_{205kA}}{N^{\mathrm{MC},\nu}_{205kA}} &= 1.026 \pm 0.002(\mathrm{stat.}) \pm 0.009(\mathrm{syst.}),\\
\frac{N^{\mathrm{data},\bar{\nu}}_{-250kA}}{N^{\mathrm{MC},\bar{\nu}}_{-250kA}} &= 0.984 \pm 0.001(\mathrm{stat.}) \pm 0.017(\mathrm{syst.}). \qquad (1)
\end{aligned}$$

The quoted systematic uncertainties do not include the uncertainties on the flux and cross section model, and they only include INGRID detector systematic uncertainties. The numbers of expected events in the Monte Carlo (MC) are obtained with the cross section models described in Sec. III A. The spatial spread of the neutrino beam is measured using the number of reconstructed events in each INGRID module. This produces a measurement of the number of events as a function of the distance from the center in both the vertical and horizontal directions. The two distributions are fit with a Gaussian, and the

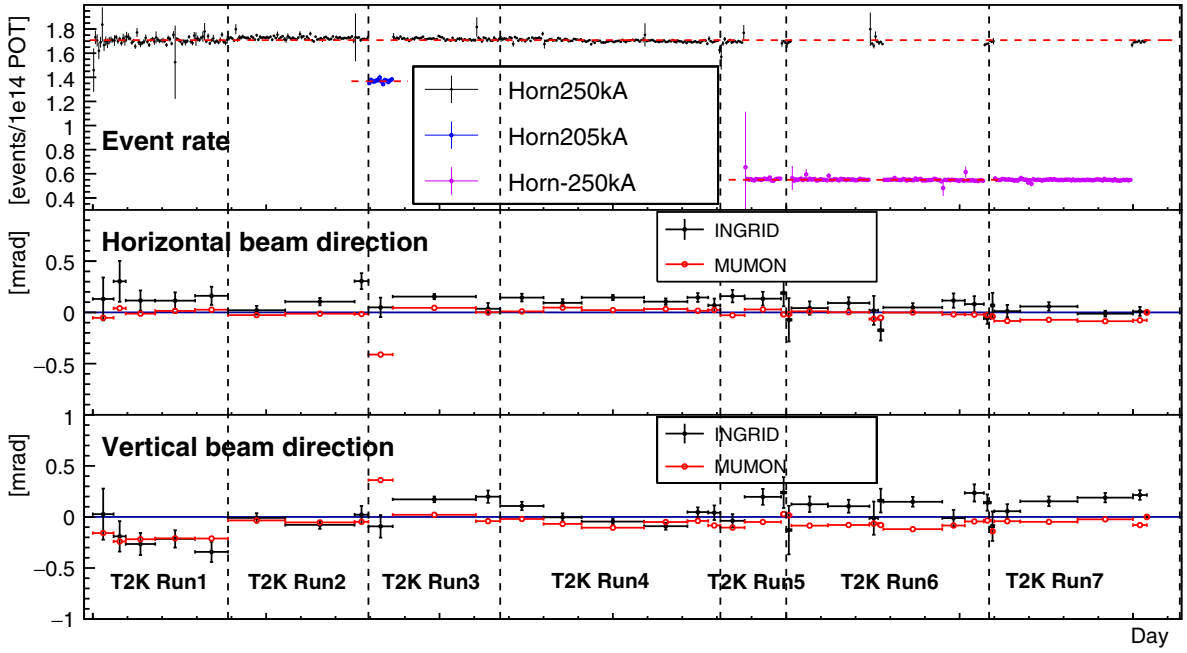

FIG. 6. The event rate at INGRID as a function of time is shown in the top panel. The horizontal dashed redline corresponds to the best fit for the different horn currents with a constant function. The central and bottom panels show the neutrino beam direction measured at INGRID and at MUMON along the horizontal and vertical transverse directions with respect to the beam as a function of time. The dashed vertical lines separate the seven T2K physics runs.

neutrino beam center and width are given by the mean and the sigma of the fit.

The measurement of the position of the beam center is crucial to determine the off-axis angle, and therefore the neutrino beam energy at SK. A deviation of 1 mrad of the beam direction would shift the peak neutrino energy by 2%. Figure 6 shows the beam direction stability for all data-taking periods. The variations are well within the design goal of 1 mrad. The average angles are

$$\bar{\theta}_X^{\text{beam},\nu} = 0.027 \pm 0.010(\text{stat.}) \pm 0.095(\text{syst.}) \text{ mrad}$$
$$\bar{\theta}_Y^{\text{beam},\nu} = 0.036 \pm 0.011(\text{stat.}) \pm 0.105(\text{syst.}) \text{ mrad} \quad (2)$$

for the ν mode and

$$\bar{\theta}_X^{\text{beam},\bar{\nu}} = -0.032 \pm 0.012(\text{stat.}) \pm 0.121(\text{syst.}) \text{ mrad}$$
$$\bar{\theta}_Y^{\text{beam},\bar{\nu}} = 0.137 \pm 0.020(\text{stat.}) \pm 0.140(\text{syst.}) \text{ mrad} \quad (3)$$

for the $\bar{\nu}$ mode. All values are compatible with the expected beam direction.

B. Off-axis ND280 detector

The off-axis near detector ND280 measures the neutrino energy spectrum, flavor content, and interaction rates of the unoscillated beam. These measurements are crucial to reduce the uncertainties on neutrino flux and interaction models which affect the prediction on the number of expected events at the far detector.

The ND280 detector consists of a set of subdetectors installed inside the refurbished UA1/NOMAD magnet, which provides a 0.2 T field, used to measure the charge and the momentum of particles passing through ND280. For the analyses described in this paper, ν_μ and $\bar{\nu}_\mu$ charged current interactions are selected in the tracker region of ND280, which consists of three time projection chambers (TPC1, 2, 3) [72], interleaved with two fine-grained detectors (FGD1, 2) [73].

The upstream FGD1 detector consists of 15 polystyrene scintillator modules, while the downstream FGD2 contains seven polystyrene scintillator modules interleaved with six water modules. The FGDs provide target mass for neutrino interactions and track the charged particles coming from the interaction vertex, while the TPCs provide 3D tracking and determine the momentum and energy loss of each charged particle traversing them. The observed energy loss in the TPCs, combined with the measurement of the momentum, is used for particle identification of the charged tracks produced in neutrino interactions in order to measure exclusive CC event rates. The major updates in the near detector analysis with respect to Ref. [27] are the use of interactions in FGD2 and the inclusion of data taken with the $\bar{\nu}$-mode beam.

The charge and particle identification ability of the tracker is important because it provides separation between μ^+ (produced by $\bar{\nu}_\mu$ CC interactions) and μ^- (produced by ν_μ CC interactions) when T2K runs in the $\bar{\nu}$ mode. Moreover, by including both FGD1 and FGD2 samples, the properties of neutrino interactions on water can be effectively isolated from those on carbon, reducing the uncertainties related to extrapolating across differing nuclear targets in the near and far detectors. The near detector analysis described here uses a reduced data set comprising 5.81×10^{20} POT in the ν mode and 2.84×10^{20} POT in the $\bar{\nu}$ mode, as shown in Table III.

TABLE III. Collected POT for each data set used in the ND280 analysis.

Run period	Dates	ν-mode POT ($\times 10^{20}$)	$\bar{\nu}$-mode POT ($\times 10^{20}$)
Run 2	Nov. 2010–Mar. 2011	0.78	···
Run 3	Mar. 2012–Jun. 2012	1.56	···
Run 4	Oct. 2012–May 2013	3.47	···
Run 5	Jun. 2014	–	0.43
Run 6	Nov. 2014–Apr. 2015	–	2.41
Total	Nov. 2010–Apr. 2015	5.81	2.84

1. ND280 ν_μ CC selection in ν mode

The event selection in the ν-mode beam is unchanged since the previous analysis described in Ref. [27]. Muon-neutrino-induced CC interactions are selected by identifying the μ^- produced in the final state as the highest-momentum, negative-curvature track in each event with a vertex in FGD1 (FGD2) fiducial volume (FV) and crossing the middle (last) TPC. The energy lost by the selected track in the TPC must be consistent with a muon.

All the events generated upstream of FGD1 are rejected by excluding events with a track in the first TPC. The selected ν_μ CC candidates are then divided into three subsamples, according to the number of identified pions in the event, CC-0π, CC-1π^+, and CC-other, which are dominated by charged current quasi elastic, CC resonant pion production, and DIS interactions, respectively. Pions are selected in different ways according to their charge. A π^+ can be identified in three ways: an FGD + TPC track with positive curvature and an energy loss in the TPC consistent with a pion, an FGD-contained track with a charge deposition consistent with a pion, or a delayed energy deposit in the FGD due to a decay electron from stopped $\pi^+ \to \mu^+$. In this analysis, π^-'s are only identified by selecting negative-curvature FGD + TPC tracks, while π^0's are identified by looking for tracks in the TPC with charge depositions consistent with an electron from a γ conversion. The output of the ν-mode tracker selection is six samples, three per FGD. The selected CC-0π and CC-1π^+ samples in both FGDs before the ND280 fit are shown in Fig. 7. For each of the selected samples, the numbers of observed and predicted events are shown in Table IV.

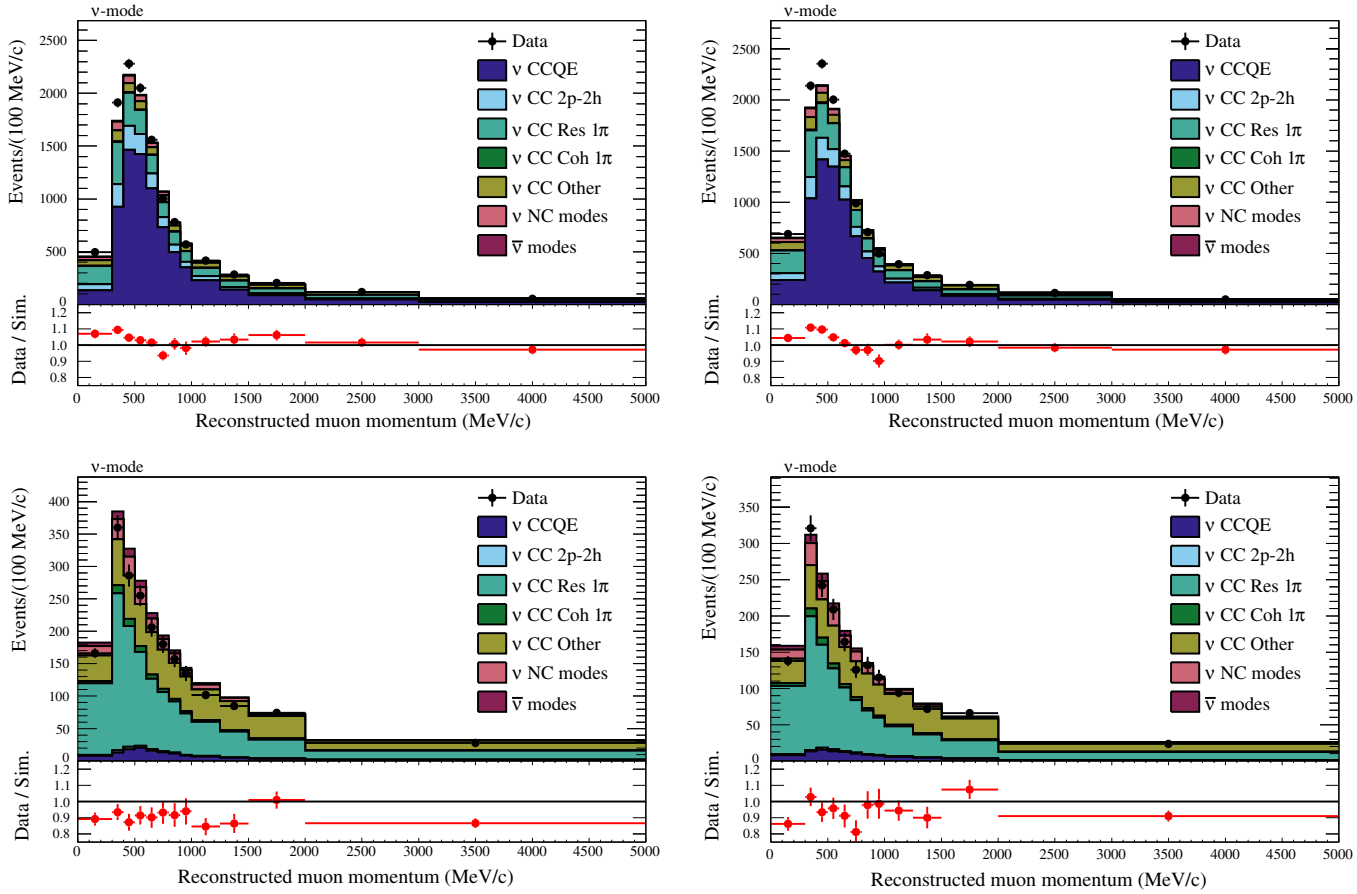

FIG. 7. Top: muon momentum distributions of the ν-mode ν_μ CC-0π samples in FGD1 (left) and FGD2 (right). Bottom: muon momentum distributions of the ν-mode ν_μ CC-1π^+ samples in FGD1 (left) and FGD2 (right). All distributions are shown prior to the ND280 fit.

2. ND280 $\bar{\nu}_\mu$ and ν_μ CC selections in $\bar{\nu}$ mode

The main difference between the ν and $\bar{\nu}$ modes is the increase in the number of interactions produced by wrong-sign neutrinos. Once differences in the flux and the cross section are taken into account, the wrong-sign contamination in the $\bar{\nu}$ mode is expected to be approximately 30%, while the wrong-sign contamination in the ν mode is approximately 4%.

TABLE IV. Observed and predicted event rates for different ND280 samples collected in ν-mode beam. Before the ND280 fit that will be described in Sec. V, uncertainties of ∼20% on the event rates are expected.

FGD1 sample	Data	Prediction
ν_μ CC-0π	17354	16951
ν_μ CC-1π^+	3984	4460
ν_μ CC-other	4220	4010
FGD2 sample	**Data**	**Prediction**
ν_μ CC-0π	17650	17212
ν_μ CC-1π^+	3383	3617
ν_μ CC-other	4118	3627

The lepton selection criteria of $\bar{\nu}_\mu$ (ν_μ) CC interactions is similar to the one used in the neutrino beam mode, except for the condition that the highest-momentum, positively (negatively) charged particles must also be the highest-momentum track in the event. This additional cut is essential to reduce the background due to π^+ (π^-) generated in neutrino (antineutrino) interactions that can be misidentified as the muon candidate. The selected $\bar{\nu}_\mu$ CC (ν_μ CC) candidate events are divided in two subsamples: CC-1-track, dominated by CCQE-like interactions, and CC-N-tracks (N > 1), a mixture of resonant production and DIS. These two subsamples are defined by the number of reconstructed tracks crossing the TPC. For these selections, the CC candidates are not divided into three subsamples as in Sec. IV B 1, according to the number of identified pions in the event in order to avoid samples with low statistics.

The output of the $\bar{\nu}$-mode tracker selection is eight samples, four per FGD. For each of the selected samples, the number of predicted events and the ones observed in

TABLE V. Observed and predicted event rates for different ND280 samples collected in the $\bar{\nu}$-mode beam. Before the ND280 fit that will be described in Sec. V, uncertainties of 20% on the event rates are expected.

FGD1 sample	Data	Prediction
$\bar{\nu}_\mu$ CC-1-track	2663	2709
$\bar{\nu}_\mu$ CC-N-tracks	775	798
ν_μ CC-1-track	989	938
ν_μ CC-N-tracks	1001	995
FGD2 sample	Data	Prediction
$\bar{\nu}_\mu$ CC-1-track	2762	2730
$\bar{\nu}_\mu$ CC-N-tracks	737	804
ν_μ CC-1-track	980	944
ν_μ CC-N-tracks	936	917

data are shown in Table V. The four selected samples in FGD1, before the ND280 fit, are shown in Fig. 8.

C. ND280 detector systematic uncertainties

In order to assess systematic uncertainties related to the ND280 detector modeling, various different control samples are used, as described in Ref. [27]. The control samples include muons produced in neutrino interactions outside ND280, cosmic muons, interactions upstream of TPC1, and stopping muons. All control samples are independent of the samples used for the ND280 analyses described earlier. The method to propagate the systematic uncertainties in the near detector analysis is also unchanged with respect to Ref. [27]; a vector of systematic parameters $\vec{d}$ scales the expected number of events in bins of p_μ and $\cos\theta_\mu$. The covariance of $\vec{d}$, V_d, is evaluated by varying each systematic parameter.

The difference with respect to the previous analysis is the inclusion of a time of flight (ToF) systematic and new methods used to evaluate charge misidentification and FGD tracking efficiency uncertainties and uncertainties due to interactions outside the fiducial volume. The ToF between FGD1 and FGD2 is used to select events with a backward muon candidate in the FGD2 samples. The ToF systematic uncertainty is ~0.1% for the ν-mode FGD2 samples and ~0.01% for the $\bar{\nu}$-mode FGD2 samples. The ToF uncertainty is smaller in the $\bar{\nu}$ mode because fewer backward-going μ^+ are produced in $\bar{\nu}_\mu$ interactions than backward-going μ^- in ν_μ interactions.

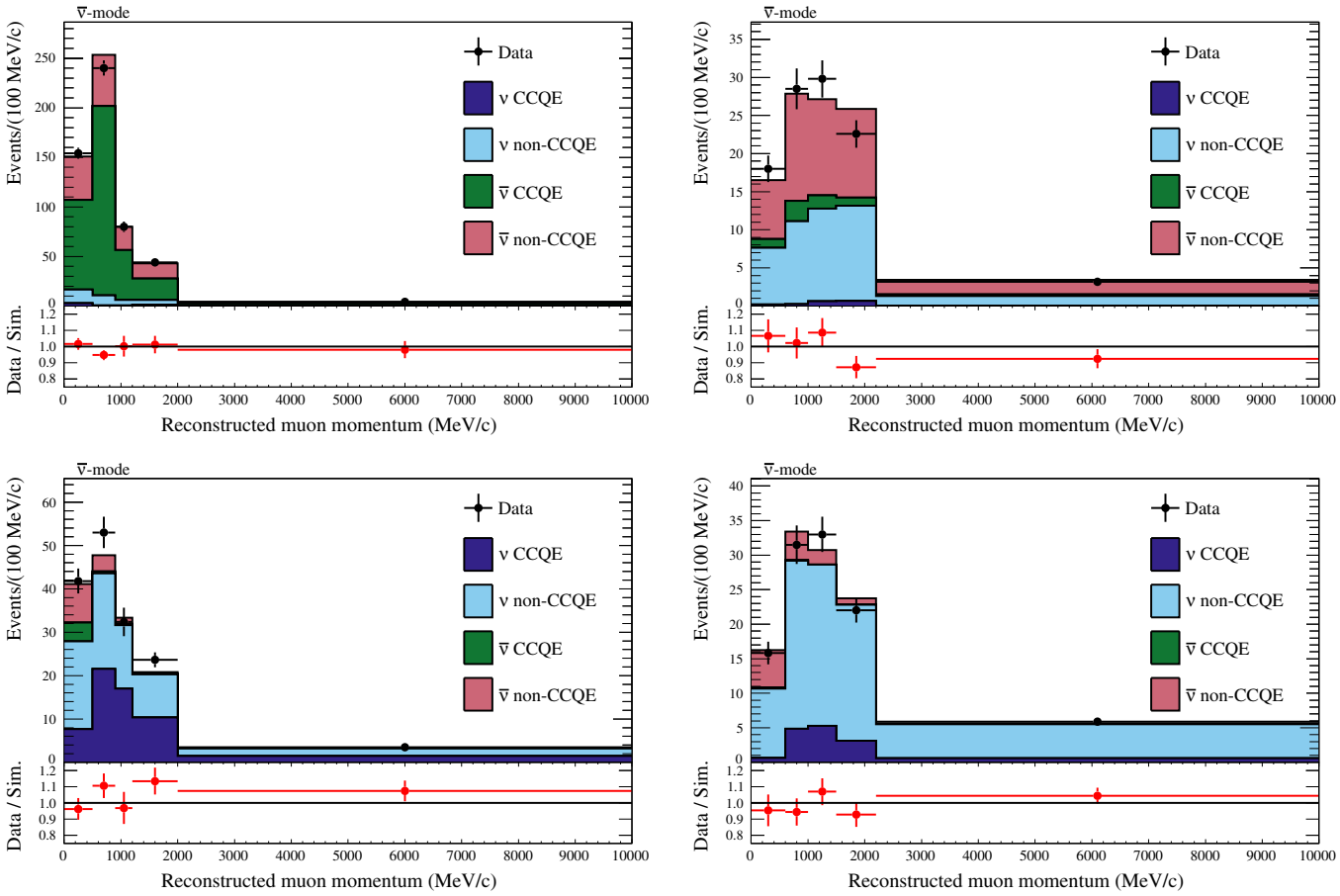

FIG. 8. Top: muon momentum distributions for the $\bar{\nu}$-mode $\bar{\nu}_\mu$ CC-1-track (left) and CC-N-tracks (right) samples. Bottom: muon momentum distributions for the $\bar{\nu}$-mode ν_μ CC-1-track (left) and CC-N-tracks (right) samples. All distributions are shown prior to the ND280 fit.

The charge misidentification uncertainty is parametrized as a function of the momentum resolution in the TPCs.

The FGD tracking efficiency for CC events, where either a short pion or proton track is also produced, is estimated using a hybrid data-MC sample. This sample uses events with a long FGD-TPC matched muon candidate track with the addition of an FGD-isolated track generated via a particle gun with a common vertex.

The method used to estimate the number of out-of-fiducial volume (OOFV) events has been refined by estimating the number of events, and the error, separately for each detector in which the OOFV events occur, rather than averaging over the number of OOFV events produced in all of the detectors outside the tracker as previously done.

Most sources of systematic error are common between the ν and $\bar{\nu}$ modes because the selection criteria are similar, as described in Sec. IV B 2. However, as $\bar{\nu}$-mode data are divided into CC 1-track and CC N-track samples, only based on the number of reconstructed FGD-TPC matched tracks, most uncertainties relating to the FGD reconstruction are not relevant. The exceptions are the FGD-TPC matching and ToF uncertainties, which apply to both modes. Other differences between modes arise because some errors change with the beam conditions (sand muons, pileup, and OOFV) and are evaluated independently for each run period.

The total systematic uncertainties are shown in Table VI.

The dominant source of uncertainty for all ND280 samples comes from the pion reinteraction model, used to estimate the rate of pion interactions in the FGDs. This is due to differences between the GEANT4 model, used to simulate pion reinteractions outside the nucleus, and the available experimental data. For example, the systematic uncertainty related to pion interactions affecting the FGD1 ν_μ CC-0π ($\bar{\nu}_\mu$ CC-1-track) sample is 1.4% (4.9%), with a total error of 1.7% (5.4%). The pion reinteraction uncertainty is larger for $\bar{\nu}$-mode samples than for ν-mode samples because π^- interactions on carbon and water are less well understood than π^+ interactions at the relevant energies and because the fraction of π^+ from wrong-sign contamination in the $\bar{\nu}$ mode misidentified as a μ^+ candidate is larger than the fraction of π^- misidentified as μ^- in the ν mode.

TABLE VI. Systematic uncertainty on the total event rate affecting the near detector samples.

ND280 sample	Total systematic uncertainty (%)
ν mode	
FGD1 ν_μ CC-0π	1.7
FGD1 ν_μ CC-1π^+	3.3
FGD1 ν_μ CC-other	6.5
FGD2 ν_μ CC-0π	1.7
FGD2 ν_μ CC-1π^+	3.9
FGD2 ν_μ CC-other	5.9
$\bar{\nu}$ mode	
FGD1 $\bar{\nu}_\mu$ CC-1-track	5.4
FGD1 $\bar{\nu}_\mu$ CC-N-tracks	10.4
FGD1 ν_μ CC-1-track	2.5
FGD1 ν_μ CC-N-tracks	4.8
FGD2 $\bar{\nu}_\mu$ CC-1-track	3.5
FGD2 $\bar{\nu}_\mu$ CC-N-tracks	7.3
FGD2 ν_μ CC-1-track	2.0
FGD2 ν_μ CC-N-tracks	4.0

V. NEAR DETECTOR DATA ANALYSIS

The predicted event rates at both the ND280 and SK are based on parametrized neutrino flux and interaction models, described in Secs. II and III A. These models are fit to the precisely measured, high statistics data at the ND280, producing both a better central prediction of the SK event rate and reducing the systematic uncertainties associated with the flux and interaction models. The near detector analysis uses event samples from both FGD1 and FGD2 and from the ν-mode and $\bar{\nu}$-mode data, giving 14 samples in total. These, along with their associated systematic uncertainty, were described in Sec. IV B.

A. Near detector likelihood and fitting methods

The forms of the ND280 likelihood and the fitting method are the same as described in Ref. [27]. The 14 event samples are binned in p_μ and $\cos\theta_\mu$, giving 1062 fit bins in total, though only the p_μ projection is shown for clarity. The likelihood assumes that the observed number of events in each bin follows a Poisson distribution, with an expectation calculated according to the flux, cross section, and detector systematic parameters discussed above. A multivariate Gaussian likelihood function is used to constrain these parameters in the fit, with the initial constraints that are described in Secs. II, III A, and IV B. The near detector systematic and near detector flux parameters are treated as nuisance parameters, as are the cross section systematic parameters governing neutral current and electron neutrino interactions. The fitted neutrino cross section and unoscillated SK flux parameters are passed to the oscillation analysis, using a covariance matrix to describe their uncertainties.

One significant difference with respect to Ref. [27] is that, as discussed in Sec. III A, the CCQE cross section parameters (except the nucleon binding energy, E_b) have no external constraint. These parameters are constrained solely by the ND280 data. In addition, in order to alleviate possible biases on the estimation of the oscillation parameters (see Sec. IX for more details), the differences between the reference model and the alternative model for the 1p1h component of the neutrino-nucleus interaction cross section described in Sec. III are taken into account in the

likelihood. This is done by adding the difference in the expected number of events between the two models in each p_μ and $\cos\theta_\mu$ bin to the diagonal of the ND280 detector covariance matrix V_d. Finally, another significant difference is the inclusion of event samples from FGD2, which contains a water target, and $\bar{\nu}$-mode data samples.

B. Fit results

The fit produces central values for the flux, cross section, and detector systematic parameters along with a covariance. Figure 9 shows the values of the unoscillated SK flux parameters, and Fig. 10 shows the cross section parameters before and after the fit as a fraction of the nominal value, along with their prior constraints. These parameter values are listed in Tables VII, VIII, and IX, showing the best-fit point for each along with its uncertainty, calculated as the square root of the diagonal of the covariance.

Most noticeable in these results is the 10%–15% increase in the neutrino flux, seen across all species and energies in both the ν and $\bar{\nu}$ modes.

Small changes are seen in the central values of the CCQE cross section parameters, with the fit increasing the Fermi momentum parameter while reducing the nucleon binding energy and axial mass parameters. More interestingly, the 2p2h normalization is increased to approximately 1.5 times its nominal value, indicating that the fit is sensitive to differences in lepton kinematics between CCQE and 2p2h interactions. The antineutrino 2p2h normalization is reduced compared to the neutrino parameter, highlighting a difference in the neutrino and antineutrino CC-0π event rates that cannot be explained by flux or detector systematics. The fit also reduces the value of the charged current single pion parameters, as seen in the previous analysis [27]. This accounts for the relative deficit observed in the CC-1π sample compared to the CC-0π sample.

1. Goodness of fit and fit validation

The goodness of fit for the near detector analysis was estimated using mock data sets including statistical uncertainties. Mock data sets are generated by simultaneously

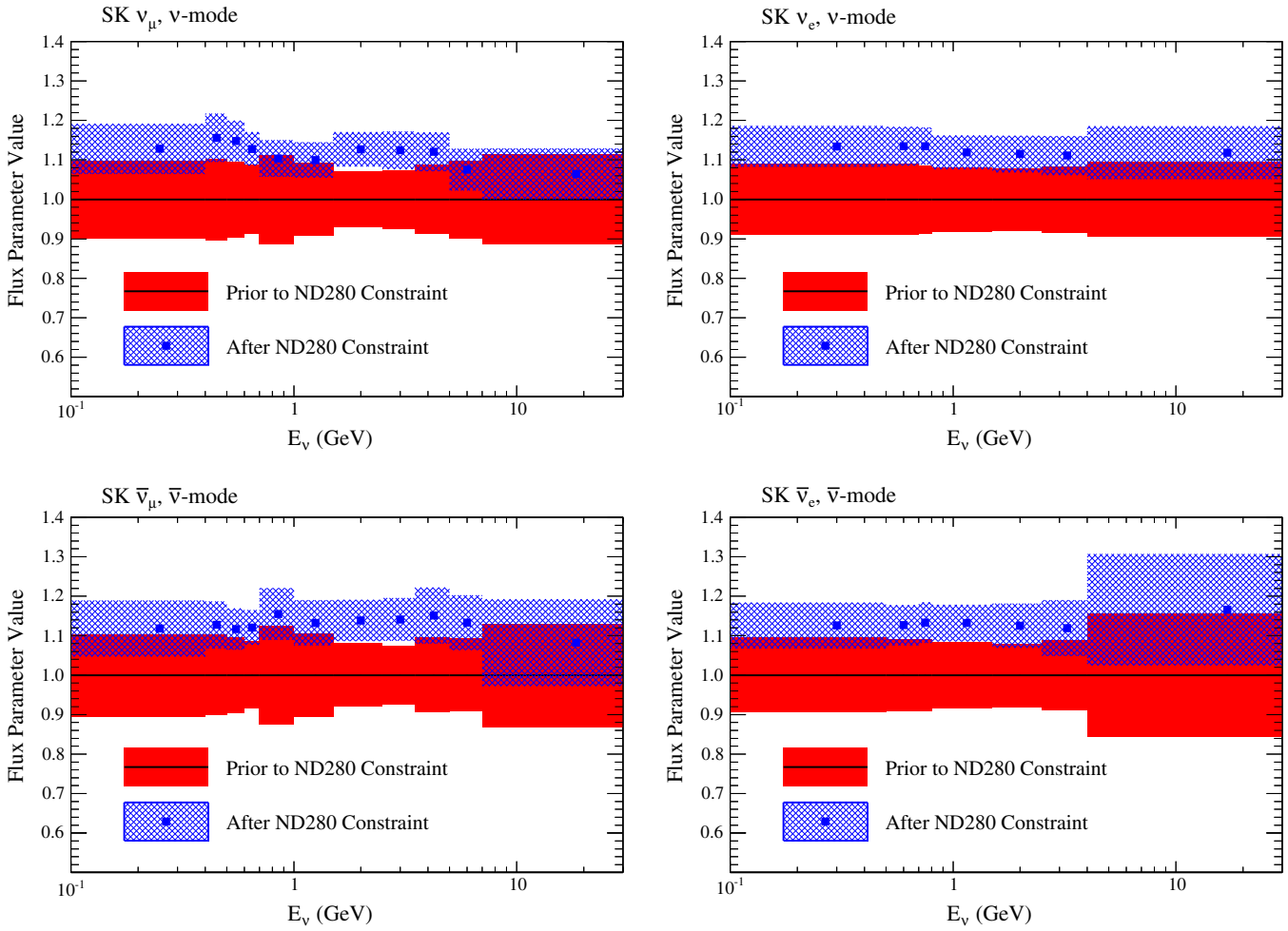

FIG. 9. The SK flux parameters for the $\overset{(-)}{\nu}_\mu$ (left) and $\overset{(-)}{\nu}_e$ (right) neutrino species in the ν (top) and $\bar{\nu}$ modes (bottom), shown as a fraction of the nominal value. The bands indicate the 1σ uncertainty on the parameters before (solid, red) and after (hatched, blue) the near detector fit.

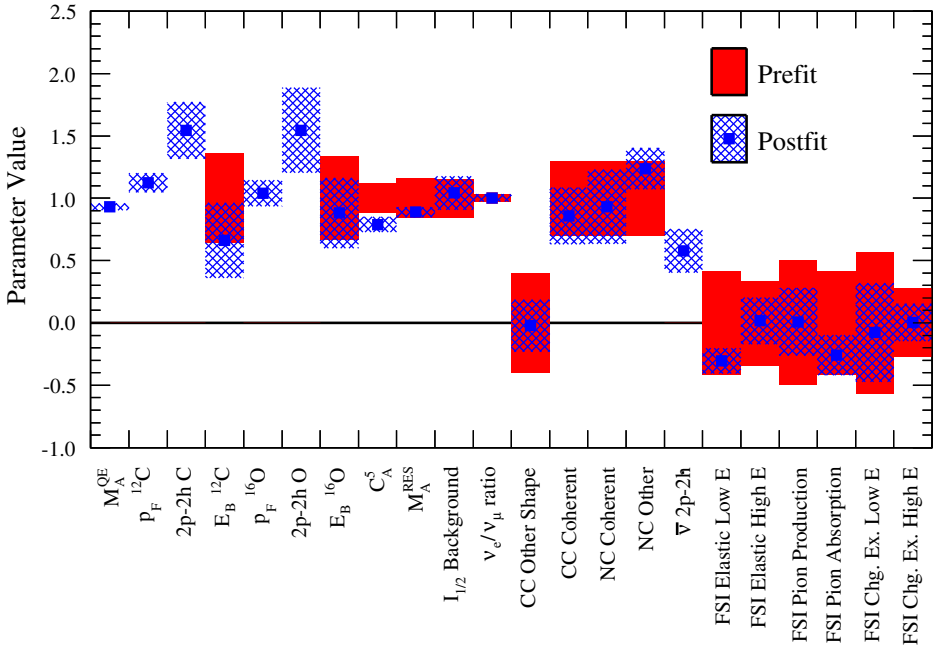

FIG. 10. Cross section parameters before (solid, red) and after (hatched, blue) the near detector fit, shown as a fraction of the nominal value (given in Table IX). The extent of the colored band shows the 1σ uncertainty.

TABLE VII. Prefit and postfit values for the SK ν-mode flux parameters.

ν-mode flux parameter (GeV)	Prefit	ND280 postfit
SK ν_μ [0.0–0.4]	1.000 ± 0.099	1.128 ± 0.064
SK ν_μ [0.4–0.5]	1.000 ± 0.103	1.156 ± 0.061
SK ν_μ [0.5–0.6]	1.000 ± 0.096	1.148 ± 0.051
SK ν_μ [0.6–0.7]	1.000 ± 0.087	1.128 ± 0.043
SK ν_μ [0.7–1.0]	1.000 ± 0.113	1.104 ± 0.047
SK ν_μ [1.0–1.5]	1.000 ± 0.092	1.100 ± 0.045
SK ν_μ [1.5–2.5]	1.000 ± 0.070	1.127 ± 0.044
SK ν_μ [2.5–3.5]	1.000 ± 0.074	1.124 ± 0.048
SK ν_μ [3.5–5.0]	1.000 ± 0.087	1.121 ± 0.049
SK ν_μ [5.0–7.0]	1.000 ± 0.098	1.075 ± 0.053
SK $\nu_\mu > 7.0$	1.000 ± 0.114	1.064 ± 0.065
SK $\bar{\nu}_\mu$ [0.0–0.7]	1.000 ± 0.103	1.100 ± 0.081
SK $\bar{\nu}_\mu$ [0.7–1.0]	1.000 ± 0.079	1.112 ± 0.048
SK $\bar{\nu}_\mu$ [1.0–1.5]	1.000 ± 0.084	1.111 ± 0.060
SK $\bar{\nu}_\mu$ [1.5–2.5]	1.000 ± 0.086	1.116 ± 0.070
SK $\bar{\nu}_\mu > 2.5$	1.000 ± 0.086	1.162 ± 0.069
SK ν_e [0.0–0.5]	1.000 ± 0.090	1.134 ± 0.052
SK ν_e [0.5–0.7]	1.000 ± 0.090	1.135 ± 0.049
SK ν_e [0.7–0.8]	1.000 ± 0.086	1.135 ± 0.047
SK ν_e [0.8–1.5]	1.000 ± 0.081	1.119 ± 0.043
SK ν_e [1.5–2.5]	1.000 ± 0.079	1.115 ± 0.046
SK ν_e [2.5–4.0]	1.000 ± 0.084	1.111 ± 0.050
SK $\nu_e > 4.0$	1.000 ± 0.094	1.118 ± 0.067
SK $\bar{\nu}_e$ [0.0–2.5]	1.000 ± 0.074	1.121 ± 0.057
SK $\bar{\nu}_e > 2.5$	1.000 ± 0.128	1.153 ± 0.117

TABLE VIII. Prefit and postfit values for the SK $\bar{\nu}$-mode flux parameters.

$\bar{\nu}$-mode flux parameter (GeV)	Prefit	ND280 postfit
SK ν_μ [0.0–0.7]	1.000 ± 0.094	1.098 ± 0.072
SK ν_μ [0.7–1.0]	1.000 ± 0.079	1.121 ± 0.052
SK ν_μ [1.0–1.5]	1.000 ± 0.077	1.130 ± 0.048
SK ν_μ [1.5–2.5]	1.000 ± 0.081	1.155 ± 0.054
SK $\nu_\mu > 2.5$	1.000 ± 0.080	1.111 ± 0.055
SK $\bar{\nu}_\mu$ [0.0–0.4]	1.000 ± 0.104	1.118 ± 0.071
SK $\bar{\nu}_\mu$ [0.4–0.5]	1.000 ± 0.102	1.127 ± 0.060
SK $\bar{\nu}_\mu$ [0.5–0.6]	1.000 ± 0.096	1.117 ± 0.052
SK $\bar{\nu}_\mu$ [0.6–0.7]	1.000 ± 0.085	1.121 ± 0.044
SK $\bar{\nu}_\mu$ [0.7–1.0]	1.000 ± 0.125	1.155 ± 0.066
SK $\bar{\nu}_\mu$ [1.0–1.5]	1.000 ± 0.105	1.132 ± 0.057
SK $\bar{\nu}_\mu$ [1.5–2.5]	1.000 ± 0.078	1.139 ± 0.053
SK $\bar{\nu}_\mu$ [2.5–3.5]	1.000 ± 0.074	1.141 ± 0.054
SK $\bar{\nu}_\mu$ [3.5–5.0]	1.000 ± 0.094	1.151 ± 0.071
SK $\bar{\nu}_\mu$ [5.0–7.0]	1.000 ± 0.093	1.133 ± 0.070
SK $\bar{\nu}_\mu > 7.0$	1.000 ± 0.130	1.082 ± 0.110
SK ν_e [0.0–2.5]	1.000 ± 0.069	1.118 ± 0.051
SK $\nu_e > 2.5$	1.000 ± 0.085	1.112 ± 0.071
SK $\bar{\nu}_e$ [0.0–0.5]	1.000 ± 0.095	1.126 ± 0.058
SK $\bar{\nu}_e$ [0.5–0.7]	1.000 ± 0.091	1.127 ± 0.051
SK $\bar{\nu}_e$ [0.7–0.8]	1.000 ± 0.091	1.133 ± 0.052
SK $\bar{\nu}_e$ [0.8–1.5]	1.000 ± 0.084	1.132 ± 0.046
SK $\bar{\nu}_e$ [1.5–2.5]	1.000 ± 0.080	1.125 ± 0.056
SK $\bar{\nu}_e$ [2.5–4.0]	1.000 ± 0.089	1.119 ± 0.071
SK $\bar{\nu}_e > 4.0$	1.000 ± 0.156	1.166 ± 0.141

TABLE IX. Prefit and postfit values for the cross section parameters used in the oscillation fits. If no prefit uncertainty is shown, then the parameter had a flat prior assigned. If a parameter was not constrained by the ND280 fit, this is noted in the postfit column.

Cross section parameter	Prefit	ND280 postfit
M_A^{QE} (GeV/c^2)	1.20	1.12 ± 0.03
p_F ^{12}C (MeV/c)	217.0	243.9 ± 16.6
2p2h ^{12}C	100.0	154.5 ± 22.7
E_b ^{12}C (MeV)	25.0 ± 9.00	16.5 ± 7.53
p_F ^{16}O (MeV/c)	225.0	234.2 ± 23.7
2p2h ^{16}O	100.0	154.6 ± 34.3
E_b ^{16}O (MeV)	27.0 ± 9.00	23.8 ± 7.61
C_A^5	1.01 ± 0.12	0.80 ± 0.06
M_A^{RES} (GeV/c^2)	0.95 ± 0.15	0.84 ± 0.04
$I_{\frac{1}{2}}$ background	1.30 ± 0.20	1.36 ± 0.17
CC other shape	0.00 ± 0.40	-0.02 ± 0.21
CC coherent	1.00 ± 0.30	0.86 ± 0.23
NC coherent	1.00 ± 0.30	0.93 ± 0.30
2p2h $\bar{\nu}$	1.00	0.58 ± 0.18
NC other	1.00 ± 0.30	Not constrained
NC 1-γ	1.00 ± 1.00	Not constrained
ν_e/ν_μ ratio	1.00 ± 0.02	Not constrained
$\bar{\nu}_e/\bar{\nu}_\mu$ ratio	1.00 ± 0.02	Not constrained
FSI elastic low-E	1.00 ± 0.41	Not constrained
FSI elastic high-E	1.00 ± 0.34	Not constrained
FSI pion production	1.00 ± 0.50	Not constrained
FSI pion absorption	1.00 ± 0.41	Not constrained
FSI charge exchange low-E	1.00 ± 0.57	Not constrained
FSI charge exchange high-E	1.00 ± 0.28	Not constrained

varying the systematic parameters in the fit according to their prior covariance then applying these to the nominal MC. These were then fit, and the minimum negative log-likelihood value was found. The distribution of the minimum negative log-likelihood values is shown by the histogram in Fig. 11, with the value from the data fit indicated with a red line. The overall p-value for the fit is 8.6%. Figure 12 shows the same distribution for the flux and cross section parameter priors, demonstrating that the fitted parameter values propagated to the oscillation analysis are reasonable.

In addition, the Bayesian analysis which simultaneously fits both near and far detector samples, that will be described in Sec. VIII B, was used to cross-check the primary result by only fitting near detector data. The results of this fit are compared to the best-fit parameters from the near detector analysis in Fig. 13, showing excellent agreement between the two.

C. ND280 postfit distributions

The expected muon momentum spectrum after the ND280 fit for the CC-0π and CC-1π^+ samples in the ν mode and the FGD1 samples in the $\bar{\nu}$ mode are shown in

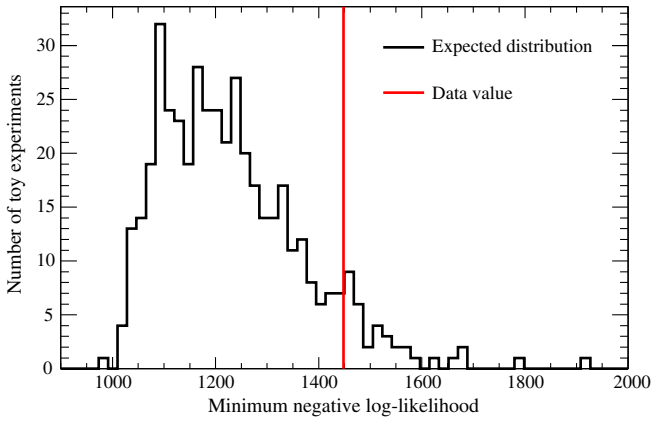

FIG. 11. Distribution of the minimum negative log-likelihood values from fits to the mock data sets (black), with the value from the fit to the data superimposed in red.

Figs. 14 and 15 respectively. After the ND280 fit, the expected distributions show in general a better agreement with the data. The numbers of postfit predicted events for all the 14 samples are shown in Table X. The effects

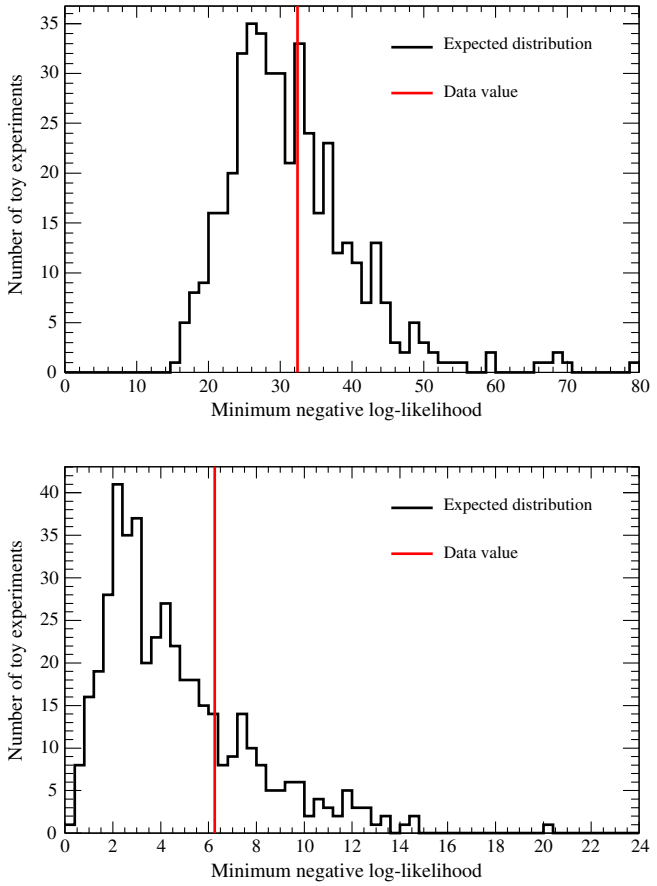

FIG. 12. Distribution of the minimum negative log-likelihood values from fits to the mock data sets (black), with the value from the fit to the data superimposed in red. The distributions shown make up the contribution from the flux (top) and cross section (bottom) prior terms.

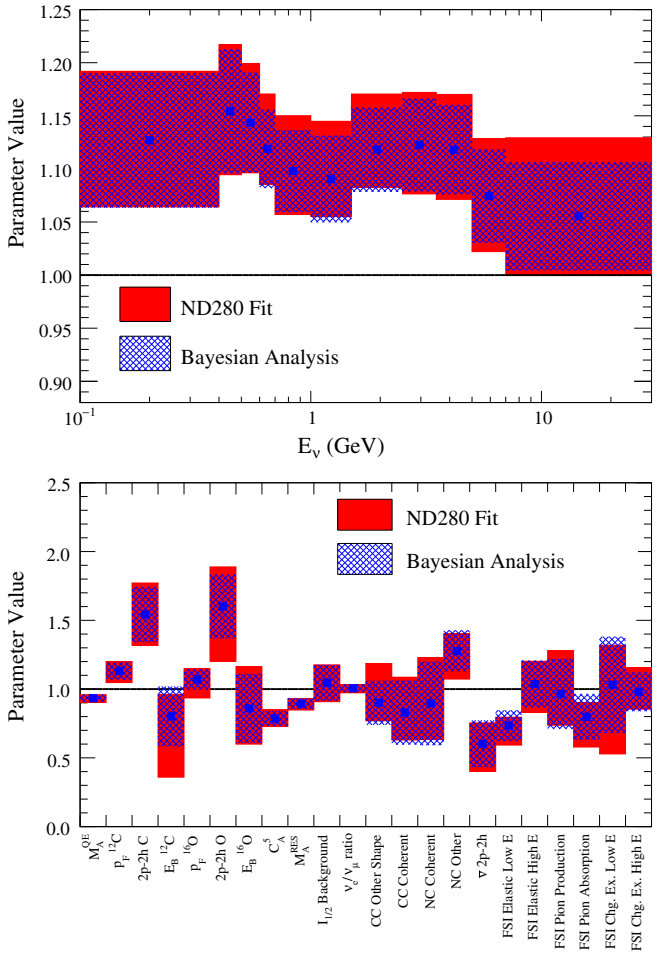

FIG. 13. Comparison of the fitted SK ν-mode flux parameters (top) and cross section parameters (bottom) between the ND280 fit (red, solid) and the Bayesian analysis (blue, hashed).

of the ND280 fit on the different neutrino interactions contributing to each ND280 sample are detailed in Tables XI and XII.

VI. FAR DETECTOR EVENT SELECTION AND SYSTEMATICS

The T2K far detector is Super-Kamiokande [74], a 50 kt water Cherenkov detector located in the Kamioka Observatory, Gifu, Japan. SK is divided into two concentric cylinders, defining an inner detector (ID) instrumented with 11,129 20 in. photomultiplier tubes (PMT) and an outer detector (OD) instrumented with 1885 PMTs. The outer detector is mainly used as a veto for entering backgrounds while neutrino interactions are selected in a fiducial volume inside the ID.

In order to precisely measure neutrino oscillations parameters, together with the large target volume, high acceptance and efficient discrimination is necessary to distinguish the leptons produced in ν_μ and ν_e interactions. Vertex, momentum reconstruction, and particle identification (PID) in SK are done by observing the Cherenkov radiation produced by charged particles traversing the detector. These particles produce ring patterns that are recorded by the PMTs and are the primary tool used for the PID. Muons produced by $\overset{(-)}{\nu}_\mu$ CC interactions are usually unscattered thanks to their large mass and produce a clear ring pattern. In contrast, electrons from $\overset{(-)}{\nu}_e$ CC interactions produce electromagnetic showers resulting in diffuse ring edges. In addition to the shape of the Cherenkov ring, the opening angle also helps to distinguish between electrons and muons. At the typical energies of leptons produced by neutrinos from the T2K beam, the probability to misidentify a single electron (muon) as a muon (electron) is 0.7% (0.8%). In SK, it is not possible to distinguish neutrinos from antineutrinos event by event since the charge of the outgoing leptons cannot be reconstructed. For this reason, the selection that will be described in this section is identical for data taken in the ν mode and in $\bar{\nu}$ mode.

T2K data are extracted from the incoming stream in ± 500 μs windows centered on the beam trigger. A scan of each window recovers individual events which are then classified.

Events in which Cherenkov light is deposited exclusively in the ID comprise the fully contained (FC) sample. PMTs in the OD that register light are grouped into clusters. If the largest such cluster contains more than 15 PMTs, the event is moved to an OD sample. Low energy (LE) events are separated into a dedicated sample by requiring that the total charge from the ID PMT hits in a 300 ns window be greater than 200 photoelectrons (p.e.), which corresponds to the charge observed from a 20 MeV electromagnetic shower. Events are also designated as LE if a single ID PMT hit constitutes more than half of the total p.e. observed to reject events due to noise. LE events are not included in the analysis presented here.

Events at the far detector are timed with respect to the leading edge of the beam spill, taking into account the neutrino time of flight, the Cherenkov photon propagation time, and delays in the electronics. Figure 16 shows the event timing (ΔT_0) distribution for all OD, LE, and FC events within ± 500 μs of the beam arrival time. For FC events, a visible energy ($E_{\rm vis}$) greater than 30 MeV is also requested. A clear peak is observed around $\Delta T_0 = 0$ in the FC sample. For an event to be incorporated into the analysis, ΔT_0 must lie in the interval $[-2, 10]$ μs. A total of four events have been observed outside this range. The expected number of such events is 4.17, estimated by using data taken with no beam. FC events within the spill window can be seen in Fig. 17 where the beam structure with eight bunches is clearly visible. The dotted lines represent the fitted bunch center times with a fixed bunch interval of 581 ns.

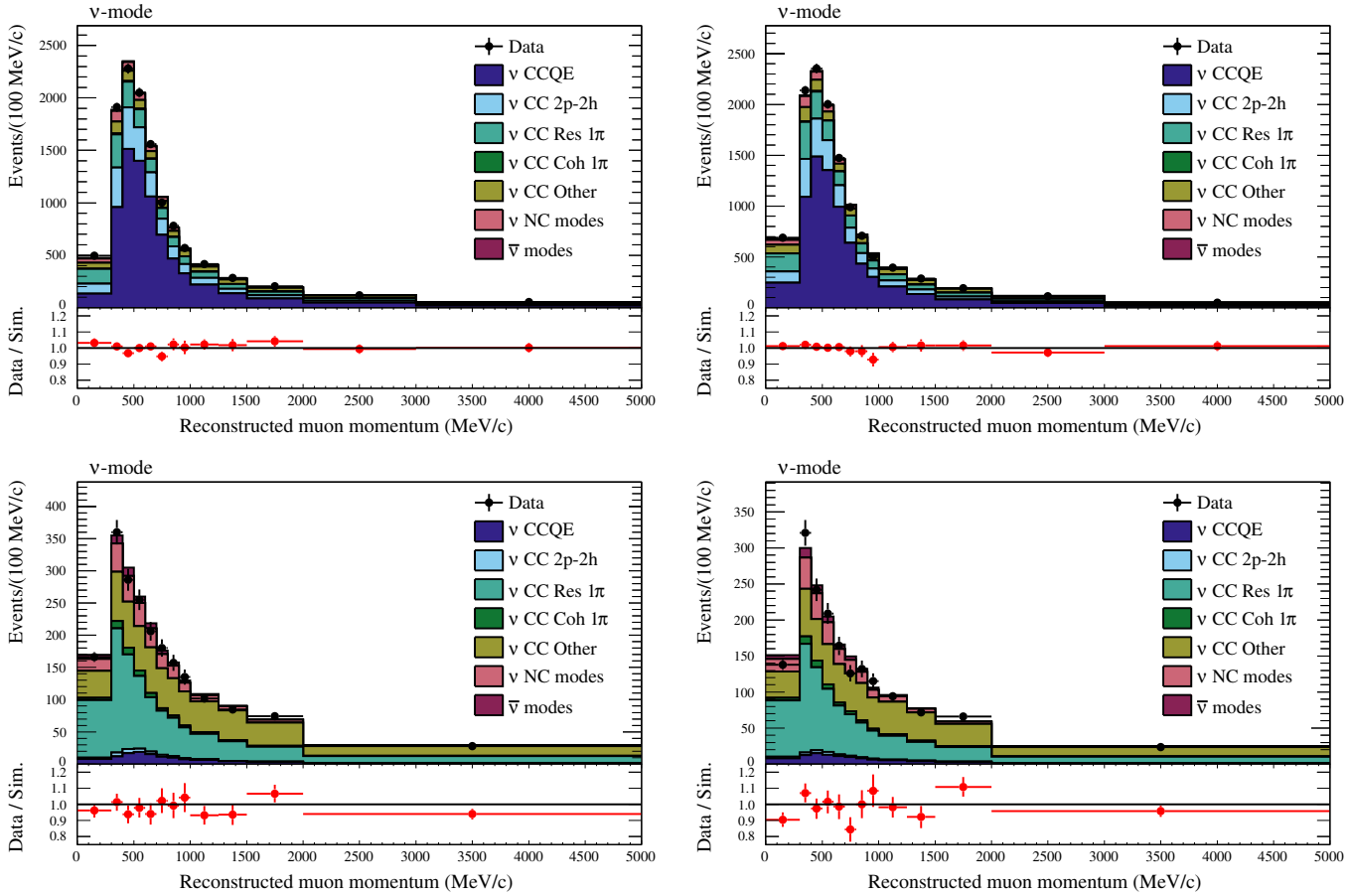

FIG. 14. Data MC comparison of ν-mode ν_μ CC-0π (top) and CC-1π^+ (bottom) samples in FGD1 (left) and FGD2 (right) after the ND280 fit. The simulation is broken down by neutrino reaction type.

A fiducial volume is defined within the ID, 2 m away from the detector wall, with a fiducial mass of 22.5 kt. Events of which the vertex is reconstructed within this volume are selected into the fully contained fiducial volume sample (FCFV). Visible energy is defined as the energy of an electromagnetic shower that produces the observed amount of Cherenkov light. In total, 608 events are classified as FCFV. The expected number of background events from nonbeam related sources in accidental coincidence is estimated to be 0.0145.

A. SK charged-current quasi-elastic selection

Charged-current interactions $(\overset{(-)}{\nu} + N \to l^{\pm} + X)$ in the narrow energy range of the T2K beam most commonly produce single-ring events at SK because most of the resulting particles, except for the primary lepton, do not escape the nucleus, or are below detection threshold. The energy of the incoming neutrino can be calculated assuming the kinematics of a CCQE interaction and neglecting Fermi motion,

$$E_\nu^{\mathrm{rec}} = \frac{m_f^2 - (m_i')^2 - m_l^2 + 2m_i' E_l}{2(m_i' - E_l + p_l \cos\theta_l)}, \tag{4}$$

where E_ν^{rec} is the reconstructed neutrino energy; m_i and m_f are the initial and final nucleon masses, respectively; and $m_i' = m_i - E_{\mathrm{b}}$, where $E_{\mathrm{b}} = 27$ MeV is the binding energy of a nucleon inside ^{16}O nuclei. E_l, p_l, and θ_l are the reconstructed lepton energy, momentum, and angle with respect to the beam, respectively. The selection criteria for both $\overset{(-)}{\nu}_e$ CC and $\overset{(-)}{\nu}_\mu$ CC events were fixed using MC studies before being applied to data. Events are determined to be e-like or μ-like based on the PID of the brightest Cherenkov ring. The PID of each ring is determined by a likelihood incorporating information on the charge distribution and the opening angle of the Cherenkov cone. The PID likelihood distribution for ν-mode FCFV single-ring events is shown in Fig. 18. The same criteria are applied to events observed for both ν- and $\bar{\nu}$-mode data taking.

$\overset{(-)}{\nu}_e$ CC candidate events are selected using the criteria listed in Table XIV. The E_{vis} requirement removes low energy NC interactions and electrons from the decay of unseen parents that are below the Cherenkov threshold or fall outside the beam time window. The π^0-like event rejection uses an independent reconstruction algorithm which was introduced in previous analyses [27]. The cut

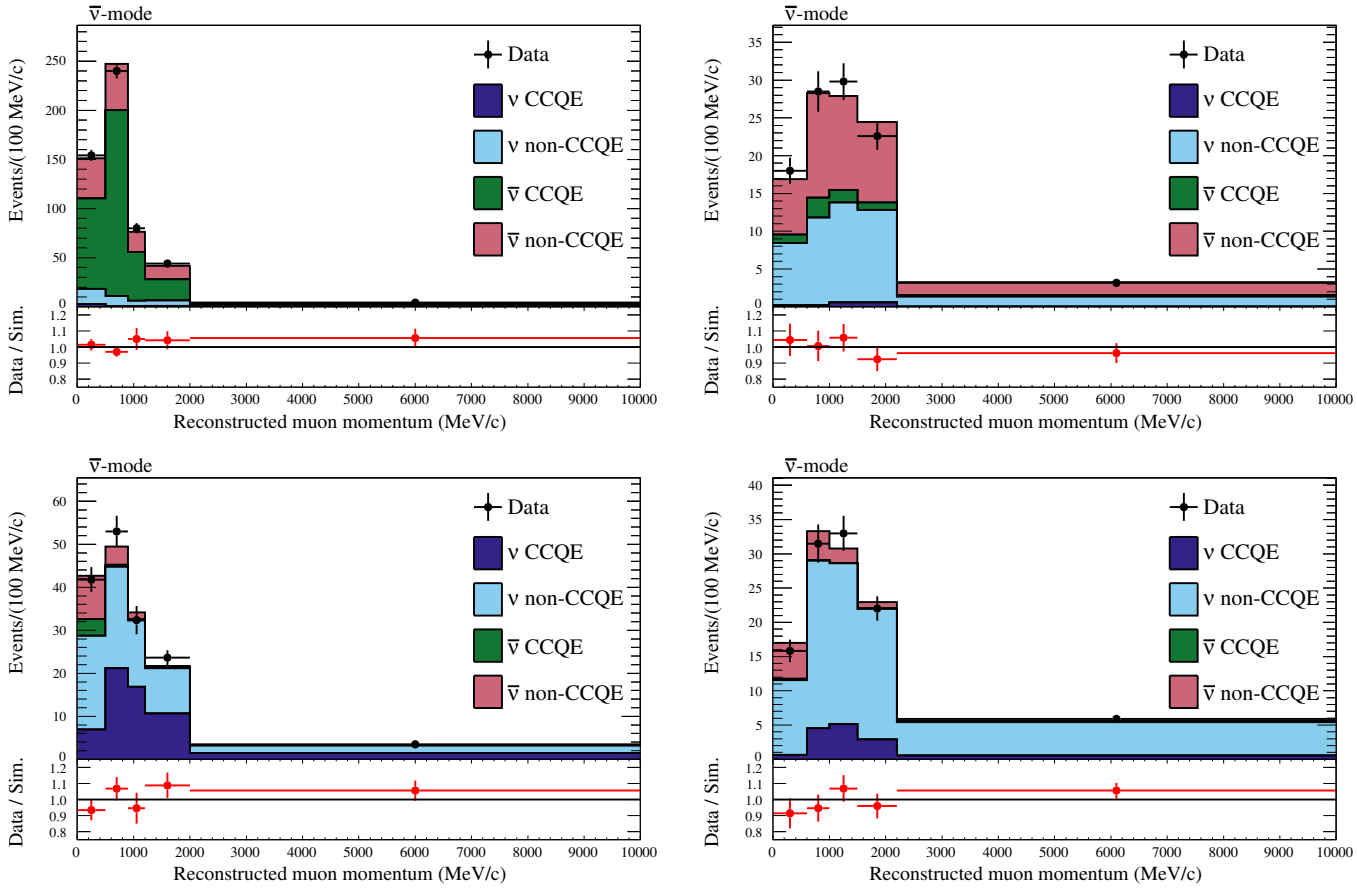

FIG. 15. Top: data MC comparison of $\bar{\nu}_\mu$ (right-sign) CC-1-track (left) and CC-N-tracks (right) samples after the ND280 fit. The simulation is broken down by neutrino reaction type. Bottom: same muon momentum distributions for ν_μ background samples.

$E_\nu^{\mathrm{rec}} < 1.25$ GeV is required, as above this energy the intrinsic beam $\overset{(-)}{\nu}_e$ background is dominant. The numbers of events remaining in the neutrino and antineutrino beam data after successive selection criteria for a simulation sample produced with the oscillation parameters of Table XIII are shown in Table XIV.

After all cuts, 32 events remain in the ν_e CC candidate sample, and 4 remain in the $\bar{\nu}_e$ CC candidate sample, as shown in Fig. 19. Kolmogorov-Smirnov (KS) tests of the accumulated events as a function of POT are compatible with a constant rate, with p-values of 0.99 and 0.25, respectively.

TABLE X. Observed and predicted events rates for different ND280 samples after the ND280 fit.

ND280 sample	FGD1 data	FGD1 postfit	FGD2 data	FGD2 postfit
ν_μ CC-0π	17354	17345	17650	17638
ν_μ CC-1π^+	3984	4113	3383	3449
ν_μ CC-other	4220	4150	4118	3965
$\bar{\nu}_\mu$ CC-1-track	2663	2639	2762	2728
$\bar{\nu}_\mu$ CC-N-tracks	775	785	737	814
ν_μ CC-1-track	989	966	980	987
ν_μ CC-N-tracks	1001	989	936	937

The vertex distributions of the candidate event samples are checked for signs of bias that might suggest background contamination. Figure 20 shows the vertex distribution of the ν_e CC candidate events in the SK tank coordinate system. Combined KS tests for uniformity in r^2 and z yield p-values of 0.1 and 0.6 for the ν_e and $\bar{\nu}_e$ samples, respectively.

$\overset{(-)}{\nu}_\mu$ CC candidate events are selected using the criteria shown in Table XV. The momentum cut rejects charged pions and misidentified electrons from the decay of unobserved muons and pions. Fewer than two Michel electrons are required to reject events with additional unseen muons or pions. After all cuts are applied, 135 events remain in the ν_μ CC candidate sample, and 66 remain in the $\bar{\nu}_\mu$ CC candidate sample as shown in Fig. 21.

B. SK charged-current single pion selection

A new far detector event sample has been included in the oscillation analysis described here. As mentioned

TABLE XI. Prefit and postfit expected fraction of events for each neutrino interactions for samples taken in the ν mode.

	FGD1 ν_μ CC-0π		FGD2 ν_μ CC-0π	
Reaction	Prefit	Postfit	Prefit	Postfit
ν CCQE	0.562	0.540	0.547	0.533
ν CC 2p2h	0.100	0.165	0.094	0.155
ν CC Resonant 1π	0.202	0.152	0.219	0.164
ν CC Coherent 1π	0.003	0.003	0.003	0.003
ν CC other	0.096	0.098	0.101	0.103
ν NC modes	0.032	0.037	0.032	0.037
$\bar{\nu}$ modes	0.003	0.003	0.004	0.004

	FGD1 ν_μ CC-1π^+		FGD2 ν_μ CC-1π^+	
Reaction	Prefit	Postfit	Prefit	Postfit
ν CCQE	0.054	0.053	0.055	0.054
ν CC 2p2h	0.008	0.014	0.007	0.013
ν CC Resonant 1π	0.485	0.409	0.476	0.401
ν CC Coherent 1π	0.025	0.025	0.026	0.025
ν CC other	0.348	0.389	0.353	0.395
ν NC modes	0.059	0.087	0.60	0.089
$\bar{\nu}$ modes	0.022	0.024	0.022	0.024

	FGD1 ν_μ CC-Other		FGD2 ν_μ CC-Other	
Reaction	Prefit	Postfit	Prefit	Postfit
ν CCQE	0.047	0.043	0.049	0.045
ν CC 2p2h	0.010	0.015	0.010	0.016
ν CC Resonant 1π	0.148	0.112	0.154	0.117
ν CC Coherent 1π	0.004	0.003	0.003	0.003
ν CC other	0.701	0.712	0.696	0.707
ν NC modes	0.078	0.102	0.075	0.099
$\bar{\nu}$ modes	0.013	0.014	0.11	0.013

TABLE XII. Prefit and postfit expected fraction of events for each neutrino interaction for samples taken in the $\bar{\nu}$ mode.

	FGD1 $\bar{\nu}_\mu$ CC-1-track		FGD2 $\bar{\nu}_\mu$ CC-1-track	
Reaction	Prefit	Postfit	Prefit	Postfit
ν CCQE	0.011	0.012	0.015	0.014
ν non-CCQE	0.069	0.077	0.074	0.080
$\bar{\nu}$ CCQE	0.733	0.751	0.731	0.751
$\bar{\nu}$ non-CCQE	0.186	0.161	0.181	0.156

	FGD1 $\bar{\nu}_\mu$ CC-N-tracks		FGD2 $\bar{\nu}_\mu$ CC-N-tracks	
Reaction	Prefit	Postfit	Prefit	Postfit
ν CCQE	0.017	0.017	0.021	0.021
ν non-CCQE	0.422	0.447	0.412	0.437
$\bar{\nu}$ CCQE	0.085	0.083	0.088	0.087
$\bar{\nu}$ non-CCQE	0.474	0.452	0.478	0.453

	FGD1 ν_μ CC-1-track		FGD2 ν_μ CC-1-track	
Reaction	Prefit	Postfit	Prefit	Postfit
ν CCQE	0.480	0.516	0.466	0.499
ν non-CCQE	0.412	0.372	0.411	0.363
$\bar{\nu}$ CCQE	0.037	0.033	0.042	0.038
$\bar{\nu}$ non-CCQE	0.071	0.079	0.081	0.100

	FGD1 ν_μ CC-N-tracks		FGD2 ν_μ CC-N-tracks	
Reaction	Prefit	Postfit	Prefit	Postfit
ν CCQE	0.150	0.163	0.143	0.154
ν non-CCQE	0.771	0.756	0.777	0.764
$\bar{\nu}$ CCQE	0.003	0.003	0.004	0.003
$\bar{\nu}$ non-CCQE	0.076	0.078	0.077	0.078

previously, single-ring events produced by quasielastic interactions are the most common at T2K neutrino energies. By modifying the event selection criteria to include an additional Michel electron candidate, it is possible to select events with a pion produced below the Cherenkov threshold. Michel electrons are tagged at SK by searching for secondary hit clusters within the same trigger window and in subsequent trigger windows that pass time, charge, and vertex goodness criteria. Note that this selection tags only positive π^+'s as π^-'s are absorbed by nuclei before they decay when stopped in water. Figure 22 shows the true Michel electron momentum distribution for true CC1π^+ simulated events reconstructed inside the fiducial volume. Figure 23 shows the true pion momentum distribution for selected signal events and the selection efficiency. The Cherenkov threshold for charged pions is also shown. The efficiency falls above this threshold as the pion produces more light and the event-fitting algorithm is increasingly likely to find a second ring, thus disqualifying events from the sample. The event reduction for the full selection is shown in Table. XVI. There is a larger background from misidentified muons in this sample compared with the single-ring selection as such events are more likely to contain a Michel electron candidate. It can be seen in Table XVI that there is an apparent difference between the data and the MC expectation after cut number 5. Applying an equivalent cut sequence to atmospheric neutrino data and MC (in this case, the neutrino direction is not known, so a cut on $E_{\rm vis}$ is used instead of $E_\nu^{\rm rec}$) yielded no such discrepancy. This single-ring CC1π^+ selection has been implemented as a new sample for ν_e appearance with neutrino beam data. The reconstructed energy equation is modified from the CCQE case by recognizing that the outgoing baryon is a Δ^{++} instead of a proton and neglecting nuclear effects,

$$E_\nu^{\rm rec} = \frac{m_{\Delta^{++}}^2 - m_p^2 - m_l^2 + 2m_p E_l}{2(m_p - E_l + p_l \cos\theta_l)}, \tag{5}$$

where $m_{\Delta^{++}}$ is the mass of the Δ^{++} (1232.0 MeV/c^2). Figure 24 shows the difference in the true and reconstructed neutrino energy for the final CC1π^+ candidate selection

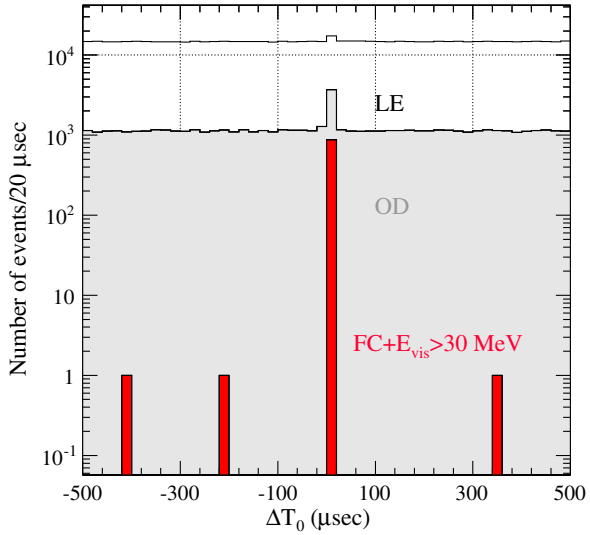

FIG. 16. ΔT_0 distribution of all FC, OD, and LE events within ± 500 μs of the expected beam arrival time observed during T2K Run 1-7. The histograms are stacked in that order.

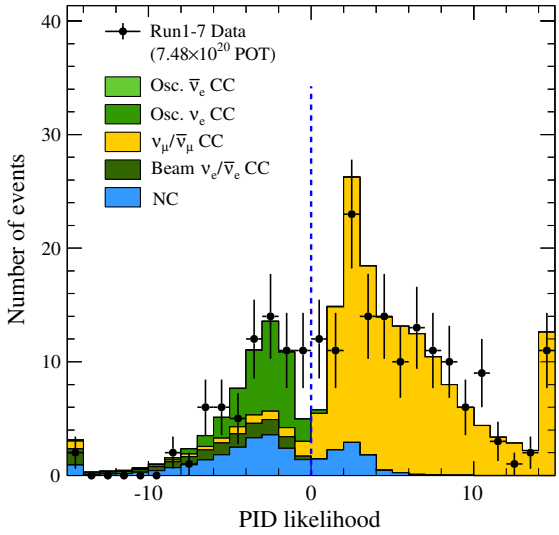

FIG. 18. The PID likelihood distribution of the observed ν-mode CC event samples after FCFV and single-ring cuts have been applied. The data are shown as points with statistical error bars and the shaded, stacked histograms are the MC predictions. The expectation is based on the parameters of Table XIII.

along with that for the single-ring selection for comparison. Figure 25 shows the reconstructed energy distribution for the final sample. Five ν_e CC1π^+ candidates are reconstructed in the data, while 3.1 events are expected for the oscillation parameters of Table XIII.

Figure 26 shows the vertex distribution of the ν_e CC1π^+ candidate events in the SK tank coordinate system.

C. SK detector systematic uncertainties

This section discusses the estimation of the uncertainty in the selection efficiency and background for the oscillation samples that result from the modeling of the SK detector. This topic has been covered in detail in previous publications [27], but there have been a number of updates, particularly related to the addition of the ν_e CC1π^+ sample.

Control samples unrelated to the T2K beam are used to assess the uncertainties. Cosmic-ray muon samples are used to estimate uncertainties related to the FC, fiducial-volume and decay-electron requirements, for the selections of both $\overset{(-)}{\nu}_e$ and $\overset{(-)}{\nu}_\mu$ CC candidates. The error from the initial FC event selection is negligible. The uncertainty in the fiducial volume is estimated to be 1% using the vertex distribution of cosmic-ray muons which have been independently determined to have stopped inside the ID. The uncertainty due to the Michel electron tagging efficiency is estimated by comparing cosmic-ray stopped muon data with MC. The rate of falsely identified

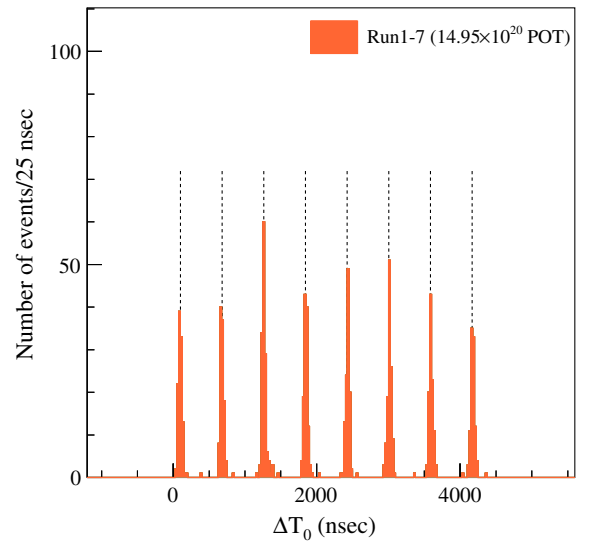

FIG. 17. ΔT_0 distribution of all FC events observed during T2K Run 1-7 zoomed in on the expected beam arrival time.

TABLE XIII. Values of the oscillation parameters used for the Monte Carlo simulation at SK. The values of $\sin^2\theta_{12}$, Δm^2_{21}, and $\sin^2\theta_{13}$ are taken from Ref. [75], while all the other oscillation parameters correspond to the most probable values obtained by the Bayesian analysis in Ref. [27].

Parameter	Value
$\sin^2 2\theta_{12}$	0.846
Δm^2_{21}	7.53×10^{-5} eV^2/c^4
$\sin^2\theta_{23}$	0.528
Δm^2_{32}	2.509×10^{-3} eV^2/c^4
$\sin^2 2\theta_{13}$	0.085
δ_{CP}	-1.601
Mass ordering	Normal

TABLE XIV. Event reduction for the ν_e CC selection at the far detector. The numbers of expected MC events divided into five categories are shown after each selection criterion is applied. The MC expectation is based upon three-neutrino oscillations with the parameters as shown in Table XIII.

		$\nu_\mu + \bar{\nu}_\mu$	$\nu_e + \bar{\nu}_e$	$\nu + \bar{\nu}$	$\bar{\nu}_\mu \to \bar{\nu}_e$	$\nu_\mu \to \nu_e$	
ν-beam mode	MC total	CC	CC	NC	CC	CC	Data
Interactions in FV	744.89	364.32	18.55	326.16	0.39	35.47	···
FCFV	431.85	279.88	18.09	98.72	0.38	34.78	438
Single ring[a]	223.49	153.40	11.15	28.68	0.32	29.95	220
Electronlike[b]	66.94	6.46	11.06	19.53	0.31	29.57	70
$E_{\rm vis} > 100$ MeV[c]	61.78	4.59	11.01	16.81	0.31	29.06	66
$N_{\text{Michel-e}} = 0$[d]	50.60	0.97	8.97	14.24	0.31	26.11	51
$E_\nu^{\rm rec} < 1250$ MeV[e]	40.71	0.25	4.26	10.85	0.22	25.14	46
Not π^0-like[f]	28.55	0.09	3.68	1.35	0.18	23.25	32
$\bar{\nu}$-beam mode							
Interactions in FV	312.38	164.04	9.00	132.75	4.30	2.29	···
FCFV	180.48	123.24	8.75	42.05	4.20	2.24	170
Single ring	96.06	73.21	5.51	11.87	3.74	1.73	94
Electronlike	21.55	2.31	5.48	8.36	3.70	1.71	16
$E_{\rm vis} > 100$ MeV	20.05	1.83	5.46	7.39	3.68	1.69	14
$N_{\text{Michel-e}} = 0$	16.40	0.33	4.71	6.24	3.66	1.46	12
$E_\nu^{\rm rec} < 1250$ MeV	11.40	0.08	1.89	4.83	3.42	1.19	9
Not π^0-like	6.28	0.02	1.58	0.60	3.04	1.05	4

[a]There is only one reconstructed Cherenkov ring.
[b]The ring is e-like.
[c]The visible energy, $E_{\rm vis}$, is greater than 100 MeV.
[d]There is no reconstructed Michel electron.
[e]The reconstructed energy, $E_\nu^{\rm rec}$, is less than 1.25 GeV.
[f]The event is not consistent with a π^0 hypothesis.

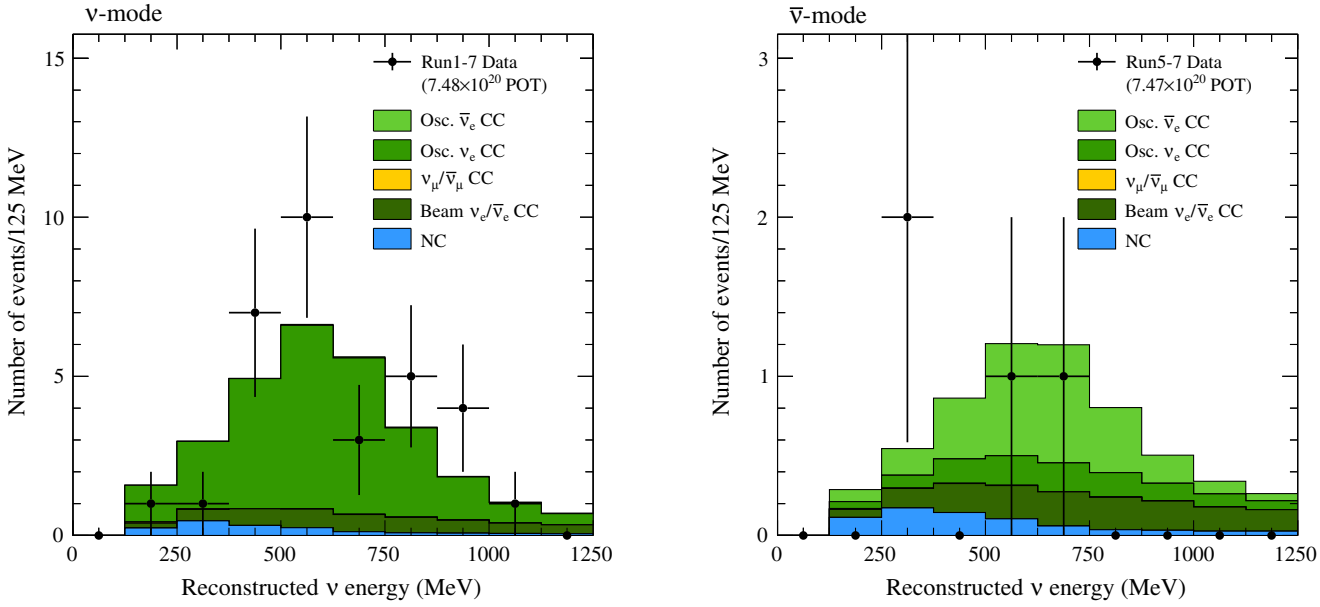

FIG. 19. The reconstructed energy spectra of the observed ν_e in ν-mode (left) and $\bar{\nu}_e$ in $\bar{\nu}$-mode (right) CC candidate event samples assuming CCQE interaction kinematics. The data are shown as points with statistical error bars, and the shaded, stacked histograms are the MC predictions. The expectation is based on the parameters of Table XIII.

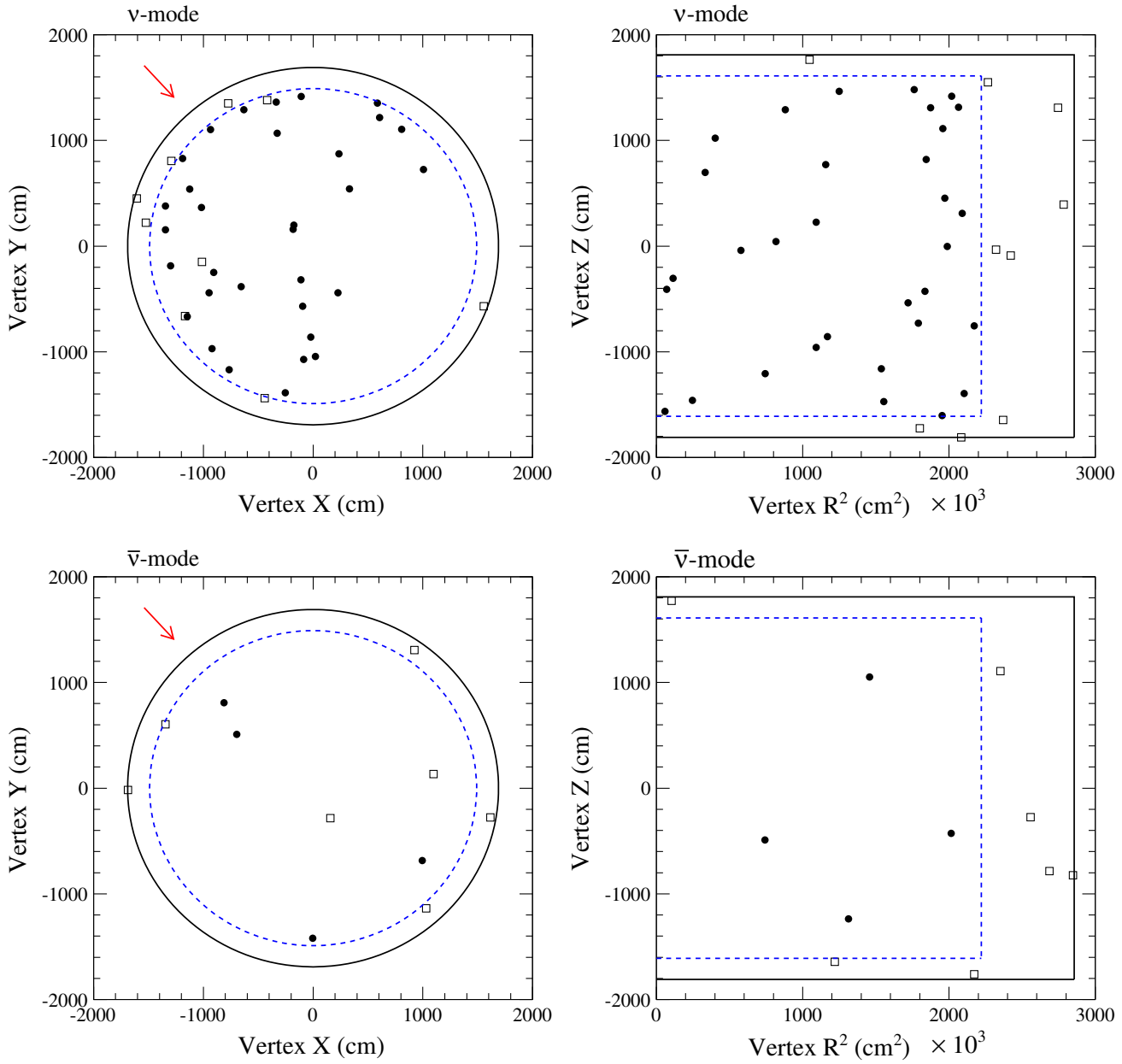

FIG. 20. Two-dimensional vertex distributions of the observed ν_e CC candidate events in (X, Y) and (R^2, Z) for the ν mode (top) and $\bar{\nu}$ mode (bottom). The arrow indicates the neutrino beam direction, and the dashed line indicates the fiducial volume boundary. Events indicated by open square markers passed all of the ν_e selection cuts except for the fiducial volume cut.

Michel electrons is estimated from MC, and a 100% uncertainty on that rate is assumed.

Other studies of systematic uncertainty in SK modeling divide simulated events into categories according to their final state topologies, with the criteria shown in Table XVII. These topologies do not correspond exactly with true interaction modes due to subsequent interactions within the nucleus or with neighboring nuclei or because one or more particles are produced below Cherenkov threshold. The dominant uncertainties are described in the following paragraphs. Atmospheric neutrino data are used to assess possible mismodeling of the ring counting (RC), PID, and π^0 rejection for the first four topologies shown in Table XVII. In addition to flux and cross section uncertainties from the atmospheric neutrino analysis, additional parameters are included in the fit to alter the cut values applied to the MC for the three classifiers above, thereby allowing for possible mismodeling of the events. Separate parameters are used for each of the four final state topologies and for different ranges of visible energy. A likelihood is defined comparing the data and MC which is then marginalized over flux and cross section parameters

TABLE XV. Event reduction for the ν_μ CC selection at the far detector. The numbers of expected MC events divided into four categories are shown after each selection criterion is applied. The MC expectation is based upon three-neutrino oscillations with the parameters as shown in Table XIII.

		ν_μ	$\bar{\nu}_\mu$	$\nu_\mu + \bar{\nu}_\mu$	$\nu_e + \bar{\nu}_e$	$\nu + \bar{\nu}$	
ν-beam mode	MC total	CCQE	CCQE	CC nonQE	CC	NC	Data
Interactions in FV	744.89	100.17	6.45	257.70	54.41	326.16	···
FCFV	431.85	78.75	4.85	196.28	53.25	98.72	438
Single ring[a]	223.49	73.49	4.70	75.21	41.41	28.68	220
Muonlike[b]	156.56	72.22	4.65	70.06	0.47	9.16	150
$p_\mu > 200$ MeV$/c$[c]	156.24	72.03	4.65	70.00	0.47	9.08	150
$N_{\text{Michel-e}} \leq 1$[d]	137.76	71.28	4.63	52.61	0.46	8.78	135
$\bar{\nu}$-beam mode							
Interactions in FV	312.38	20.04	30.77	113.23	15.59	132.75	···
FCFV	180.48	15.04	24.95	83.26	15.19	42.05	170
Single ring	96.06	13.52	24.28	35.41	10.98	11.87	94
Muonlike	74.52	13.40	23.96	33.56	0.09	3.52	78
$p_\mu > 200$ MeV$/c$	74.42	13.39	23.92	33.54	0.09	3.48	78
$N_{\text{Michel-e}} \leq 1$	68.26	13.18	23.85	27.79	0.09	3.35	66

[a]There is only one reconstructed Cherenkov ring.
[b]The ring is μ-like.
[c]The reconstructed momentum, p_μ, is greater than 200 MeV$/c$.
[d]There are less than two reconstructed Michel electrons.

using a Markov chain Monte Carlo to estimate corrected efficiencies for the four final state topologies in bins of E_{vis} and their covariance. The measured shifts between the nominal and fitted efficiencies are included in the final uncertainty assuming full correlation between samples.

To estimate the uncertainty in modeling π^0's, we construct a set of hybrid data MC control samples. Events in these samples are created by overlaying a single electronlike ring from the SK data with a simulated photon ring. The kinematics of the photon ring are chosen such that, when combined, the two rings follow the decay kinematics of π^0 events from the T2K MC. Hybrid samples with both rings from the SK MC are also produced for comparison with the hybrid data. The difference in the selection efficiency when using the oscillation analysis sample candidate criteria is used to determine the

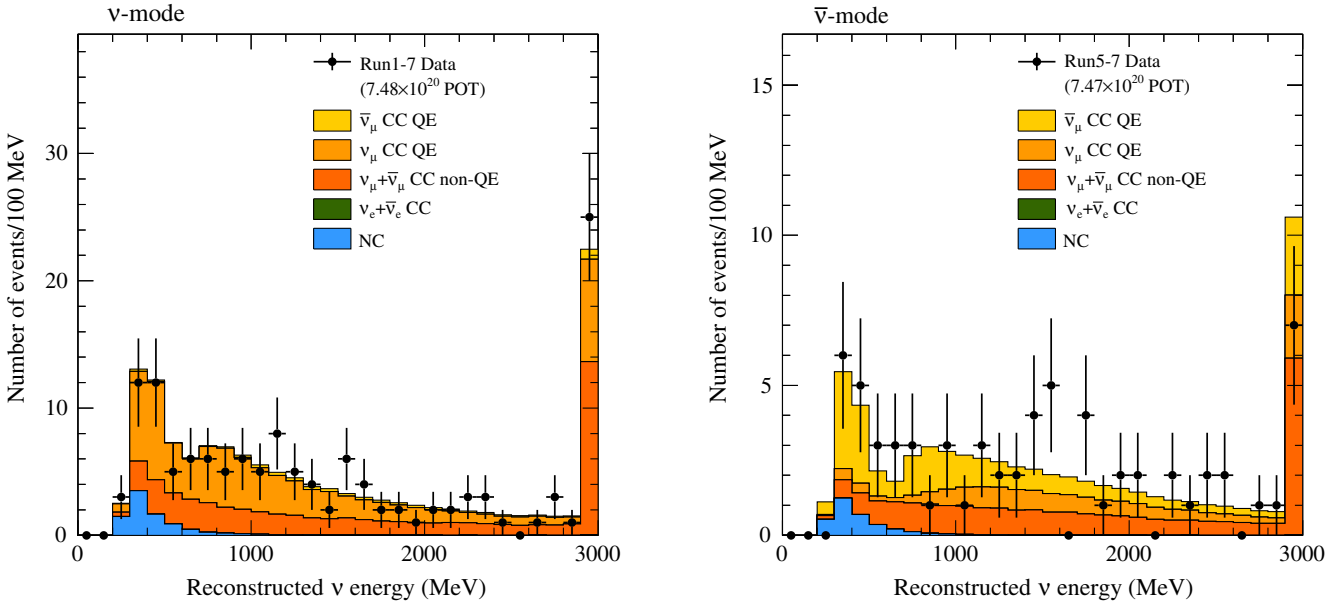

FIG. 21. The reconstructed energy spectra of the observed ν_μ in ν-mode (left) and $\bar{\nu}_\mu$ in $\bar{\nu}$-mode (right) CC candidate event samples assuming CCQE interaction kinematics. The data are shown as points with statistical error bars, and the shaded, stacked histograms are the MC predictions, and the rightmost bin includes overflow. The expectation is based on the parameters of Table XIII.

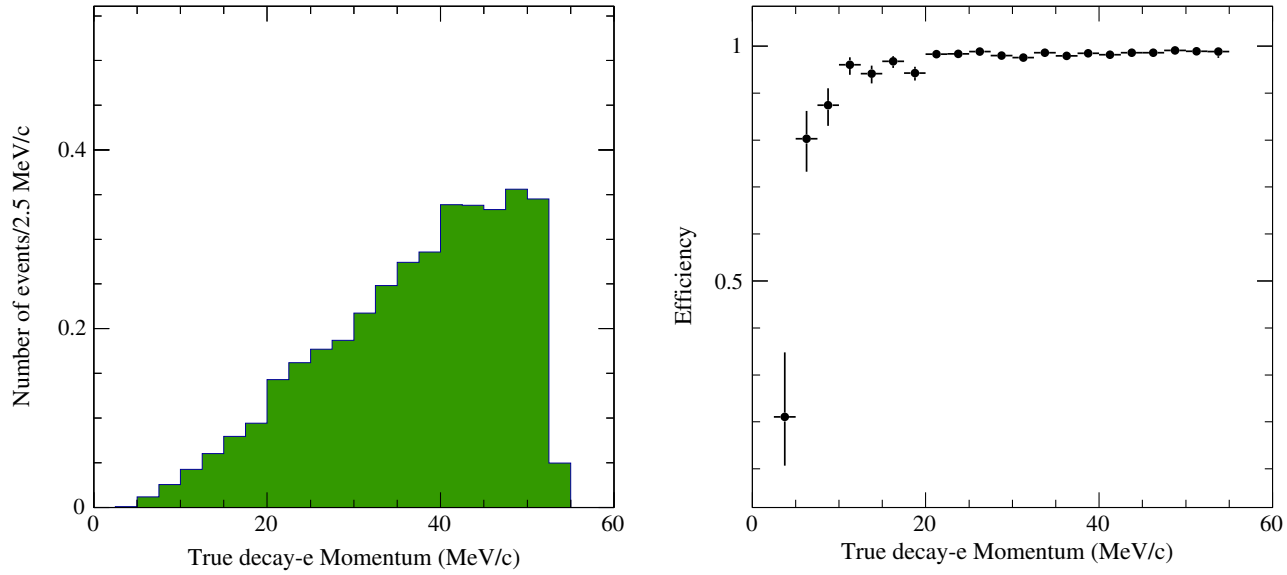

FIG. 22. The true momentum distribution for tagged Michel electrons from true CC1π^+ simulated events reconstructed in the fiducial volume (left) and the tagging efficiency for these events (right). The expectation is based on the parameters of Table XIII.

systematic error. This procedure is performed twice, with the data electron as the higher energy and lower energy ring, and the uncertainties are combined.

In previous analyses, the CC1μ events in the ν_e appearance sample that did not involve muon decay in flight (81% of CC1μ) were assigned a conservative 150% error due to the ring counting, PID, and π^0 rejection cuts. However, while these events form only ~1% of the ν_e CCQE-like candidate sample, they are ~10% of the ν_e CC1π^+ candidate sample, and thus the uncertainty was reevaluated with a dedicated analysis using stopped cosmic-ray muons and atmospheric neutrinos. Based upon this work, this uncertainty has been reduced to 63.2%, where the error on the particle identification is the dominant source of uncertainty. For CC1μ events involving a muon decay in flight, a 16% uncertainty is assigned, unchanged with respect to the previous analysis.

All aspects of the SK detector simulation that can affect the modeling of the candidate event selection described above are propagated using a vector of systematic uncertainty parameters, $\vec{s}$, which scale the nominal expected number of events in bins of the observable kinematic

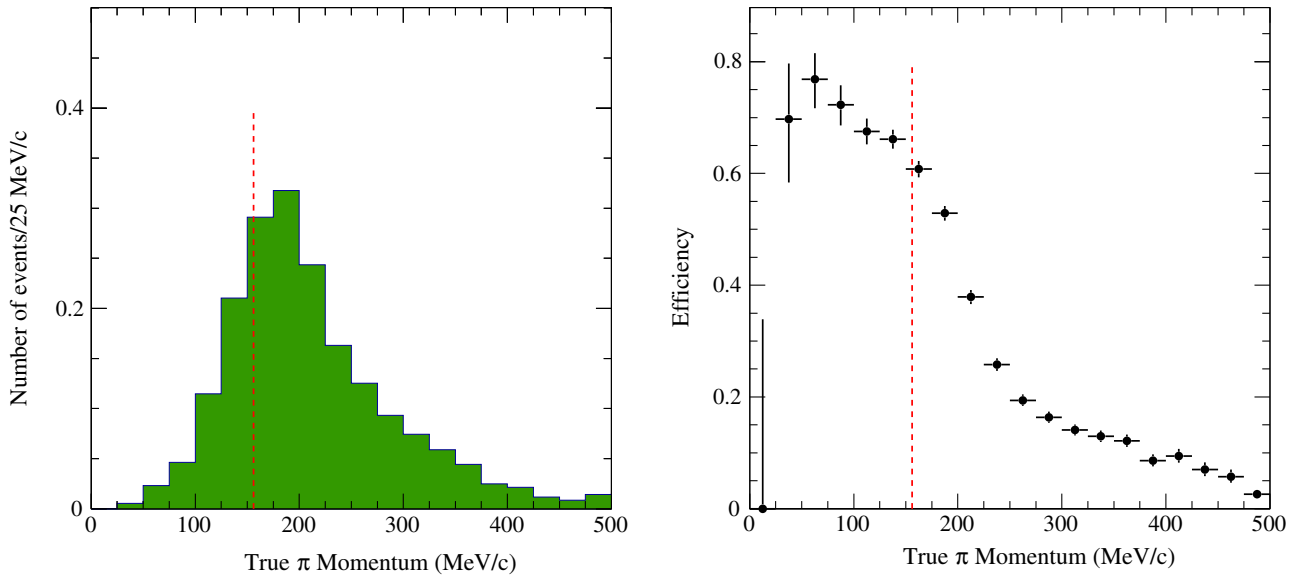

FIG. 23. The true momentum distribution for selected simulated signal events in the CC1π^+ candidate sample (left) and the selection efficiency for these events (right). The expectation is based on the parameters of Table XIII. The red dashed line indicates the Cherenkov threshold for charged pions.

TABLE XVI. Event reduction for the ν_e CC1π^+ selection at the far detector. The numbers of expected MC events divided into five categories are shown after each selection criterion is applied. The MC expectation is based on the parameters of Table XIII.

		$\nu_\mu + \bar{\nu}_\mu$	$\nu_e + \bar{\nu}_e$	$\nu + \bar{\nu}$	$\bar{\nu}_\mu \to \bar{\nu}_e$	$\nu_\mu \to \nu_e$	
ν-beam mode	MC total	CC	CC	NC	CC	CC	Data
Interactions in FV	744.89	364.32	18.55	326.16	0.39	35.47	···
FCFV	431.85	279.88	18.09	98.72	0.38	34.78	438
(1) Single ring[a]	223.49	153.40	11.15	28.68	0.32	29.95	220
(2) Electronlike[b]	66.94	6.46	11.06	19.53	0.31	29.57	70
(3) $E_{\text{vis}} > 100$ MeV[c]	61.78	4.59	11.01	16.81	0.31	29.06	66
(4) $N_{\text{Michel-e}} = 1$[d]	9.36	2.42	1.87	2.14	0.01	2.92	14
(5) $E_\nu^{\text{rec}} < 1250$ MeV[e]	4.66	0.70	0.50	0.78	<0.01	2.66	11
(6) Not π^0-like[f]	3.14	0.29	0.39	0.15	<0.01	2.31	5

[a]There is only one reconstructed Cherenkov ring.
[b]The ring is e-like.
[c]The visible energy, E_{vis}, is greater than 100 MeV.
[d]There is one reconstructed Michel electron.
[e]The reconstructed energy, E_ν^{rec}, is less than 1.25 GeV.
[f]The event is not consistent with a π^0 hypothesis.

variables E_ν^{rec} or p_l for the true neutrino interaction mode categories.

VII. NEUTRINO OSCILLATION FRAMEWORK

The previous sections have described how the near detector samples are used to reduce the uncertainties on the neutrino fluxes before oscillation and on the neutrino interaction model parameters. The best-fit values of the neutrino and antineutrino flux and cross section parameters together with their correlations are extrapolated to SK, where the oscillation probabilities are measured. In this section, the general model that describes the oscillations between the three standard neutrino flavors, ν_e, ν_μ, and ν_τ, are described, with a focus on the relevant oscillation channels for the T2K experiment. Finally, external measurements of neutrino oscillation parameters, which are used as prior constraints in some fits, are summarized.

A. Oscillation probabilities in the PMNS framework

As anticipated by Pontecorvo, the neutrino flavor eigenstates do not correspond to mass eigenstates but are linear superpositions of them,

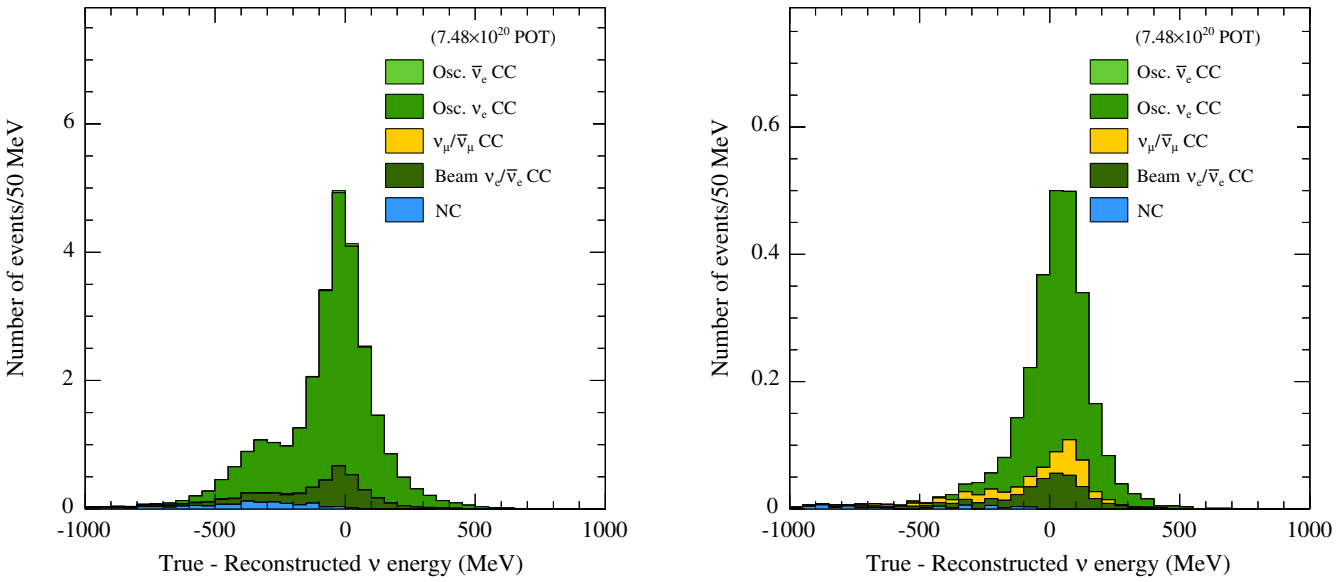

FIG. 24. Difference between true and reconstructed energy of the ν_e CCQE-like (left) and CC1π^+ (right) simulated samples. The energy for the CCQE-like sample is reconstructed using Eq. (4). For the CC1π^+ sample, the modified interaction kinematics in Eq. (5) are used. The expectation is based on the parameters of Table XIII.

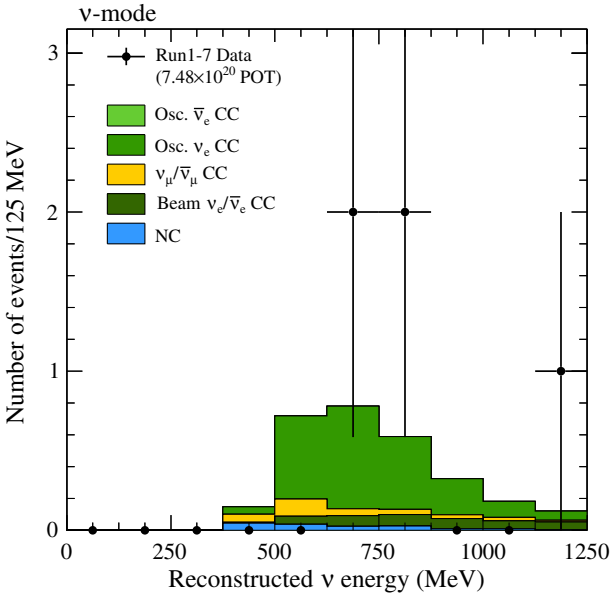

FIG. 25. The reconstructed energy spectrum of the observed ν_e CC1π^+ candidate events assuming the modified interaction kinematics in Eq. (5). The data are shown as points with statistical error bars, and the shaded, stacked histograms are the MC predictions. The expectation is based on the parameters of Table XIII.

$$|\nu_\alpha\rangle = \sum_k U_{\alpha k}|\nu_k\rangle \qquad (\alpha = e, \mu, \tau), \tag{6}$$

where only the three active neutrinos, $k = 1, 2, 3$ are considered. $U_{\alpha k}$ is an element of the 3×3 unitary matrix, called the PMNS matrix [76,77], which can be parametrized as

$$U = \begin{pmatrix} 1 & 0 & 0 \\ 0 & c_{23} & s_{23} \\ 0 & -s_{23} & c_{23} \end{pmatrix} \begin{pmatrix} c_{13} & 0 & s_{13}e^{-i\delta_{CP}} \\ 0 & 1 & 0 \\ -s_{13}e^{i\delta_{CP}} & 0 & c_{13} \end{pmatrix} \times \begin{pmatrix} c_{12} & s_{12} & 0 \\ -s_{12} & c_{12} & 0 \\ 0 & 0 & 1 \end{pmatrix}, \tag{7}$$

where $s_{ij} \equiv \sin\theta_{ij}$ and $c_{ij} \equiv \cos\theta_{ij}$, θ_{ij} are the three mixing angles and δ_{CP} is the CP-violating phase. The Majorana phases are neglected here as the three-flavor oscillation probability is invariant under their rotation.

The neutrino oscillation probability is determined by six parameters: the mixing angles θ_{12}, θ_{13}, θ_{23}, which define the amplitude of the oscillation probability; the differences in the squared masses of the eigenstates, $\Delta m^2_{21} = m^2_2 - m^2_1$ and $\Delta m^2_{32} = m^2_3 - m^2_2$, that define the oscillation frequency and the position of the oscillation maxima as a function of L/E; and the CP-violating phase, δ_{CP}. While it is known that $\Delta m^2_{21} > 0$, the neutrino mass ordering (MO) and hence the sign of Δm^2_{32} have not yet been determined.

Effects due to charged-current coherent scattering of ν_e with the electrons in the Earth matter can affect the neutrino event rate. The matter effect potential is proportional to $+N_e$ for ν_e and $-N_e$ for $\bar{\nu}_e$, where N_e is the matter electron density.

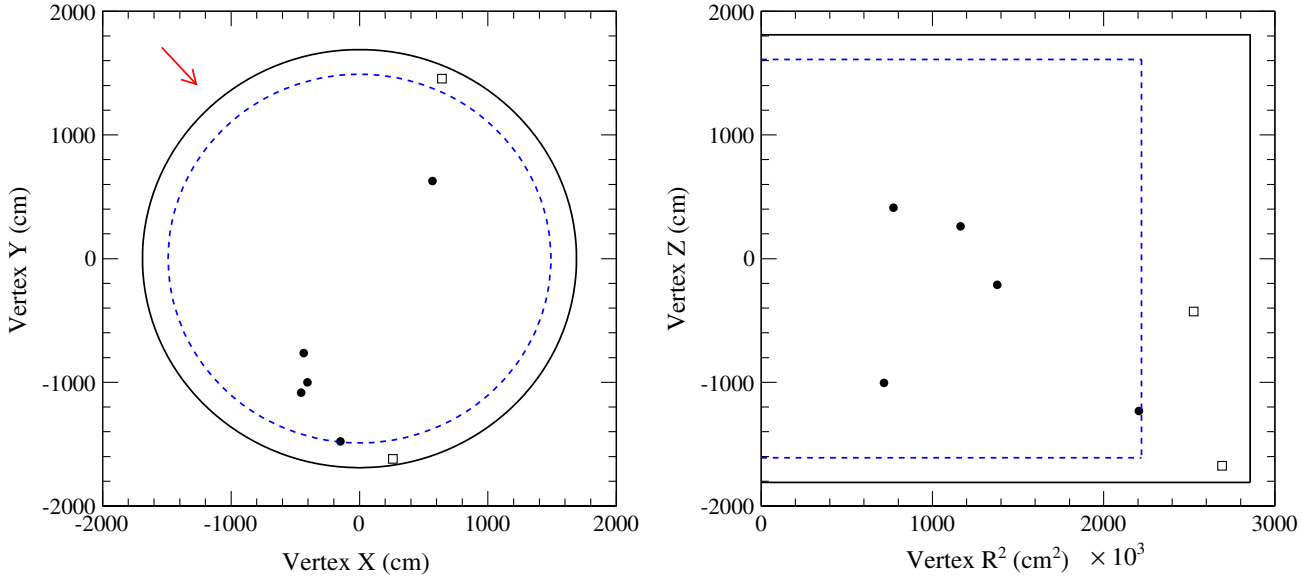

FIG. 26. Two-dimensional vertex distributions of the observed ν_e CC1π^+ candidate events in (X, Y) and (R^2, Z). The arrow indicates the neutrino beam direction, and the dashed line indicates the fiducial volume boundary. Events indicated by open square markers passed all of the ν_e CC1π^+ selection cuts except for the fiducial volume cut.

Neglecting matter effects, the $\overset{(-)}{\nu}_\mu$ survival probability can be written as

$$\begin{aligned}P(\overset{(-)}{\nu}_\mu \to \overset{(-)}{\nu}_\mu) = 1 &- 4(s_{12}^2 c_{23}^2 + s_{13}^2 s_{23}^2 c_{12}^2 + 2 s_{12} s_{13} s_{23} c_{12} c_{23} \cos\delta_{CP}) s_{23}^2 c_{13}^2 \sin^2\phi_{31} \\ &- 4(c_{12}^2 c_{23}^2 + s_{13}^2 s_{23}^2 s_{12}^2 - 2 s_{12} s_{13} s_{23} c_{12} c_{23} \cos\delta_{CP}) s_{23}^2 c_{13}^2 \sin^2\phi_{32} \\ &- 4(s_{12}^2 c_{23}^2 + s_{13}^2 s_{23}^2 c_{12}^2 + 2 s_{12} s_{13} s_{23} c_{12} c_{23} \cos\delta_{CP})(c_{12}^2 c_{23}^2 + s_{13}^2 s_{23}^2 s_{12}^2 - 2 s_{12} s_{13} s_{23} c_{12} c_{23} \cos\delta_{CP}) \sin^2\phi_{21},\end{aligned} \tag{8}$$

where

$$\phi_{kj} = \frac{\Delta m_{kj}^2 L}{4E}. \tag{9}$$

$|\Delta m_{32}^2|$ and $\sin^2 2\theta_{23}$ can be determined from Eq. (8), but the θ_{23} octant, i.e. whether $\theta_{23} > \pi/4$ or $\theta_{23} < \pi/4$, cannot be distinguished. At the T2K baseline and peak neutrino energy, the impact of the matter effect is small, and a full calculation including them would only modify the $P(\nu_\mu \to \nu_\mu)$ and $P(\bar{\nu}_\mu \to \bar{\nu}_\mu)$ probabilities by ~0.1%.

The $\overset{(-)}{\nu}_e$ appearance probability, approximated to first order in the matter effect (see Ref. [78]), is

$$\begin{aligned}P(\overset{(-)}{\nu}_\mu \to \overset{(-)}{\nu}_e) = &\, 4 c_{13}^2 s_{13}^2 s_{23}^2 \sin^2\phi_{31} \left(1 + \frac{2\alpha}{\Delta m_{31}^2}(1 - 2 s_{13}^2)\right) + 8 c_{13}^2 s_{12} s_{13} s_{23} (c_{12} c_{23} \cos\delta_{CP} - s_{12} s_{13} s_{23}) \cos\phi_{23} \sin\phi_{31} \sin\phi_{21} \\ &\overset{(+)}{-} 8 c_{13}^2 c_{12} c_{23} s_{12} s_{13} s_{23} \sin\delta_{CP} \sin\phi_{32} \sin\phi_{31} \sin\phi_{21} + 4 s_{12}^2 c_{13}^2 (c_{12}^2 c_{23}^2 + s_{12}^2 s_{23}^2 s_{13}^2 - 2 c_{12} c_{23} s_{12} s_{23} s_{13} \cos\delta_{CP}) \sin^2\phi_{21} \\ &- 8 c_{13}^2 s_{13}^2 s_{23}^2 (1 - 2 s_{13}^2) \frac{\overset{(-)}{+} \alpha L}{4E} \cos\phi_{32} \sin\phi_{31},\end{aligned} \tag{10}$$

where "(−)" corresponds to the change of sign required for antineutrino oscillations. ρ is the average density of the Earth matter through which the neutrinos travel, and $\alpha(\mathrm{eV}^2/\mathrm{c}^4) = 7.56 \times 10^{-5} \rho(\mathrm{g/cm}^3) E_\nu(\mathrm{GeV})$. In all oscillation analyses described here, the exact three-flavor oscillation probabilities are used, rather than the approximations shown in this section.

TABLE XVII. Criteria for categorization of simulated events by final state topology for systematic studies. N_x is the number of particles of type x, and the number of charged pions ($N_{\pi^\pm}$) and protons (N_p) only includes those particles produced with momentum above the Cherenkov threshold set at 156.0 and 1051.0 MeV/c, respectively.

Event type	MC truth selection criteria
CC $1e$	ν_e CC and $N_{\pi^0} = 0$ and $N_{\pi^\pm} = 0$ and $N_P = 0$
CC e other	ν_e CC and not ν_e CC$1e$
CC 1μ	ν_μ CC and $N_{\pi^0} = 0$ and $N_{\pi^\pm} = 0$ and $N_P = 0$
CC μ other	ν_μ CC and $N_{\pi^0} = 0$
CC $\mu\pi^0$ other	ν_μ CC and $N_{\pi^0} > 0$
NC $1\pi^0$	NC and not NC 1γ and $N_{\pi^0} = 1$ and $N_{\pi^\pm} = 0$ and $N_P = 0$
NC π^0 other	NC and not NC 1γ and $N_{\pi^0} \geq 1$ and not NC $1\pi^0$
NC 1γ	NC 1γ in the MC generator
NC $1\pi^\pm$	NC and not NC 1γ and $N_{\pi^0} = 0$ and $N_{\pi^\pm} = 1$ and $N_P = 0$
NC other	NC and not NC 1γ and not NC $1\pi^0$ and not NC $1\pi^\pm$ and not NC π^0 other

As well as being proportional to $\sin^2\theta_{13}$, the first, leading, term of Eq. (10) is proportional to $\sin^2\theta_{23}$, which makes the appearance probability (in contrast to the disappearance probability) sensitive to the octant of θ_{23}. The precise determination of θ_{23} and the solution of the octant degeneracy are important for the determination of δ_{CP}. Because of the precise measurement of θ_{13} from reactor experiments (see Table XVIII), the largest uncertainty in the oscillation model which affects the determination of δ_{CP} is due to the uncertainties on the value of θ_{23}.

By looking at the other terms in Eq. (10), it is easy to understand why the $\overset{(-)}{\nu}_e$ appearance transition is the golden channel in the search for CP violation. The term containing $\sin\delta_{CP}$ in Eq. (10) has an opposite sign for neutrinos and antineutrinos and is the only term that can violate CP symmetry. Since all the mixing angles have been measured as nonzero, the requirement for violating CP symmetry in neutrino oscillations is $\sin\delta_{CP} \neq 0$, i.e. $\delta_{CP} \neq 0, \pi$.

In T2K, the term proportional to $\sin\delta_{CP}$ can change the appearance probability by as much as ±30%. This means that an extreme value of δ_{CP} such as $\delta_{\mathrm{CP}} = -\pi/2$ would increase (decrease) the ν_e ($\bar{\nu}_e$) by 30% with respect to

$\delta_{\mathrm{CP}} = 0$. In Eq. (10), there are also other terms containing $\cos\delta_{CP}$. While these terms do not violate CP symmetry, they change the shape of the appearance spectrum and are important for a precise determination of the value of δ_{CP}.

In summary, at first order, the term in $\sin\delta_{CP}$ defines the normalization of the $\overset{(-)}{\nu}_{\mu} \to \overset{(-)}{\nu}_{e}$ spectrum, while the term in $\cos\delta_{CP}$ provides information on the shape and allows the discrimination of the CP-conserving phases $\delta_{CP} = 0$ and π.

As mentioned above, the appearance probability is also affected by the matter effects. Matter effects can enhance either $\nu_\mu \to \nu_e$, or $\bar{\nu}_\mu \to \bar{\nu}_e$ depending on the sign of Δm^2_{32}. For instance, if the mass ordering is normal (inverted), $\nu_\mu \to \nu_e$ oscillations are enhanced (suppressed), while $\bar{\nu}_\mu \to \bar{\nu}_e$ oscillations are suppressed (enhanced).

With its low neutrino energy and baseline of 295 km, the T2K experiment is not sensitive to the matter effect. The two possible solutions for the MO change the appearance probability by approximately $\pm 10\%$, and a definitive measurement of the MO cannot be made by exploiting the matter effects in T2K beam. The interplay between effects due to δ_{CP} and effects due to the MO on the $\overset{(-)}{\nu}_{e}$-appearance probabilities are shown in Fig. 27. Each ellipse shows the effect due to δ_{CP} on the two appearance probabilities, and the two ellipses represent the two possible solutions for the mass ordering. The two regions overlap for more than half of the δ_{CP} range, indicating the large degeneracy among the MO and δ_{CP} at the T2K baseline.

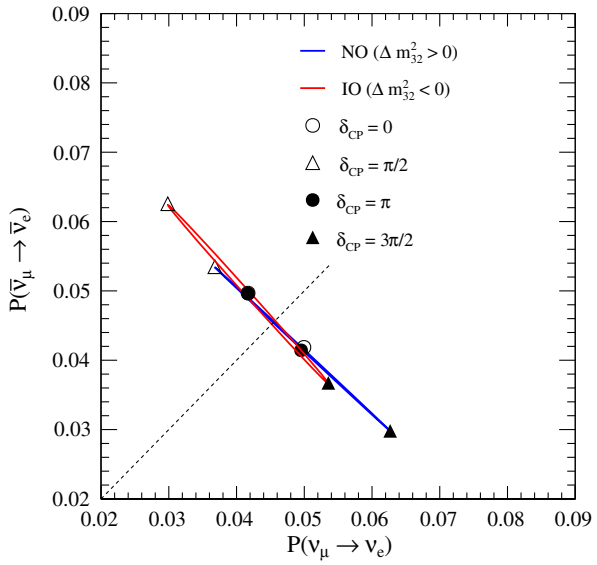

FIG. 27. The oscillation probability for $\nu_\mu \to \nu_e$ and $\bar{\nu}_\mu \to \bar{\nu}_e$ transitions as a function of δ_{CP} and MO for $E_\nu = 0.6$ GeV and a baseline of 295 km. The other oscillation parameters are fixed to the values shown in Table XIII. The dashed line indicates $P(\nu_\mu \to \nu_e) = P(\bar{\nu}_\mu \to \bar{\nu}_e)$.

The goal of T2K is the precise measurement of θ_{13}, θ_{23}, $|\Delta m^2_{32}|$ and to search for evidence of CP violation. Since T2K has excellent sensitivity to the absolute value of Δm^2_{32} but not to its sign, the absolute value of Δm^2_{32} and the MO are considered as two separate parameters. As mentioned above, the violation of CP symmetry would manifest itself as a difference between neutrino and antineutrino oscillation probabilities. In order to find a hint of this violation, it is necessary to directly compare $\nu_\mu \to \nu_e$ and $\bar{\nu}_\mu \to \bar{\nu}_e$ oscillation probabilities, as also shown in Fig. 27, where the anticorrelation as a function of both δ_{CP} and MO is visible. The measurement of the $\overset{(-)}{\nu}_{\mu}$ survival probabilities is important for determining $|\Delta m^2_{32}|$, i.e. the position of the first oscillation maximum, and $\sin^2 2\theta_{23}$, drastically reducing the uncertainty on δ_{CP}. The degeneracy between δ_{CP} and the θ_{23} octant can be solved by comparing ν_e and $\bar{\nu}_e$ appearance probabilities. Indeed, in contrast to δ_{CP}, $\sin^2\theta_{23}$ has the same effect on both the $\nu_\mu \to \nu_e$ and the $\bar{\nu}_\mu \to \bar{\nu}_e$ oscillation probabilities. For this reason, T2K measures the $\nu_\mu \to \nu_\mu$ $(\bar{\nu}_\mu \to \bar{\nu}_\mu)$ disappearance and the $\nu_\mu \to \nu_e$ $(\bar{\nu}_\mu \to \bar{\nu}_e)$ appearance probabilities in the ν and $\bar{\nu}$ modes simultaneously in the analyses described in this paper. The joint analysis also allows all of the correlations between the oscillation parameters to be properly taken into account.

B. External constraints on the oscillation parameters

For some of the oscillation parameters, Gaussian priors, based on external experiments, are used in the oscillation analyses. These parameters are the solar oscillation parameters, to which T2K is insensitive, and, in some cases, the value of $\sin^2\theta_{13}$ as measured by reactor experiments. In the latter case, the weighted average of Daya Bay, RENO, and Double Chooz as reported in Ref. [75] is used. The Gaussian priors used in the analysis are shown in Table XVIII. For all the results shown in this paper, it will be specified whether reactor constraints on $\sin^2\theta_{13}$ are used.

All the parameters that are measured by T2K are included in the oscillation analyses with flat priors which extend beyond the allowed regions for those parameters. The boundaries on the flat priors used in the analysis are $0.3 < \sin^2\theta_{23} < 0.7$, $2 < \Delta m^2_{32}$ $(\times 10^{-3} eV^2/c^4) < 3$, $-\pi < \delta_{\mathrm{CP}} < \pi$, and $0 < \sin^2(2\theta_{13}) < 0.4$ (when no reactor measurements are used).

TABLE XVIII. Gaussian priors used for the neutrino oscillation parameters, taken from Ref. [75].

Oscillation parameter	Mean and standard deviation
$\sin^2 2\theta_{12}$	0.846 ± 0.021
Δm^2_{21}	$(7.53 \pm 0.18) \times 10^{-5}$ eV^2/c^4
$\sin^2 2\theta_{13}$	0.085 ± 0.005

VIII. OSCILLATION ANALYSIS METHOD

In this section, the oscillation analyses which have been developed to provide oscillation parameter estimations are described; three different analyses have been developed within frequentist and Bayesian frameworks.

For all analyses, the appearance and disappearance channels in both the ν and $\bar{\nu}$ modes are analysed simultaneously, incorporating constraints from several T2K samples and external experiments. The oscillation analyses compare the rate and distribution of events in analysis bins defined by combinations of the reconstructed neutrino energy, $E_\nu^{\rm rec}$ [see Eq. (4)]; the reconstructed lepton momentum; and the reconstructed angle of the outgoing lepton with model predictions. Systematic uncertainties are characterized by systematic model parameters, which tune the model prediction, and by a covariance matrix, which determines the sizes and correlations of their uncertainties. The fit to the near detector data is applied as a multivariate Gaussian penalty term to constrain flux and cross section uncertainties common to the near and far detectors.

For a given set of systematic and oscillation parameters, the expected distribution is computed in the following way. The expected SK MC samples are produced assuming nominal systematic parameters without oscillation. The effects of oscillations are then included by applying the neutrino oscillation probability to events defined by neutrino energy and interacting flavor. In order to do this, all the analyses use the full three-flavor oscillation probabilities. The number of events is weighted by the oscillation probability and for the systematic parameters, as will be described in Sec. VIII D. Then, the expected number of events in each bin of the far detector samples is extracted from a Poisson distribution, leading to a likelihood of the form

$$-2\ln\mathcal{L}(\vec{o},\vec{f}) = 2\sum_{i=0}^{N-1}[n_i^{\rm obs}\cdot\ln(n_i^{\rm obs}/n_i^{\rm exp}) + (n_i^{\rm exp} - n_i^{\rm obs})], \tag{11}$$

where $\vec{o}$ and $\vec{f}$ are particular choices of the vector of the neutrino oscillation parameters (free in the fit) and of the nuisance parameters. $n_i^{\rm obs}$ is the observed number of events in the ith analysis template bin, and $n_i^{\rm exp} = n_i^{\rm exp}(\vec{o},\vec{f})$ is the expected number of events in the ith bin.

The method described in Ref. [79] is used to project out the nuisance parameters. The high dimensionality of the likelihood function is solved by computing the marginal likelihood. This marginal likelihood for the parameters of interest is found by integrating the product of the likelihood function and the priors over all the parameters that are not of interest and is defined as

$$\mathcal{L}_{\rm marg}(\vec{o};x) = \int_F \mathcal{L}(\vec{o},\vec{f};x)\pi(\vec{f})d\vec{f} = \frac{1}{n}\sum_{i=1}^{n}\mathcal{L}(\vec{o},\vec{f}_i;x). \tag{12}$$

This defines the likelihood which is a function only of the parameters of interest $\vec{o}$, given a data set, x, and a model prediction defined by a set of systematic and oscillation parameters. The marginal likelihood of Eq. (12) can be used to perform both a hybrid frequentist-Bayesian analysis as well as a full Bayesian analysis. In both cases, the prior p.d.f. for flux, cross section, and SK detector parameters is a multivariate Gaussian, with mean μ and covariance V. All the analyses have been validated with simulated data sets using different neutrino interaction models and different sets of oscillation parameters for the generation of the simulated samples. Examples of the validations will be shown in Sec. IX.

A. Frequentist analyses

Two analyses have been developed in the frequentist framework. The main difference between the two analyses is that one uses two-dimensional (2D) templates in $\{E_\nu^{\rm rec},\theta_{\rm lep}\}$ for the e-like samples and the other uses $\{p_{\rm lep},\theta_{\rm lep}\}$ templates. The reasons for these choices will be described in Sec. VIII C. Both analyses construct confidence intervals or regions by fitting the SK data set, using the likelihood ratio $-2\Delta\ln\mathcal{L}(\vec{o}) = -2\ln[\mathcal{L}(\vec{o};x)/\mathcal{L}_{\rm max}(x)]$ as the test statistic, where $\mathcal{L}(\vec{o};x)$ is as defined in Eq. (12). If the Gaussian approximation holds, Eq. (12) converges to a χ^2 distribution, and the negative log-likelihood ratio is sometimes denoted as $\Delta\chi^2(\vec{o})$.

Due to the difficulties in providing confidence intervals with high dimensionality, a subset of the oscillation parameters is projected out by using the marginalization method described above, with the priors shown in Table XVIII.

Two approaches can be used in order to calculate the confidence intervals. In the Gaussian approximation, where the parameter dependence is linear, the so-called "constant $\Delta\chi^2$ method" provides the correct coverage: the confidence region consists of the set of oscillation parameter values that satisfies the condition $-2\Delta\ln\mathcal{L}(\vec{o}) \le X_{\rm crit}(\vec{o})$. The precomputed values of $X_{\rm crit}(\vec{o})$ [75], that define the $\alpha\%$ confidence level for different dimensionalities, do not depend on the value of $\vec{o}$.

Since in the neutrino oscillation analysis the Gaussian approximation condition does not always hold, a toy MC method, recommended by Feldman and Cousins [80], should be used to define the values of $X_{\rm crit}(\vec{o})$ as a function of $\vec{o}$, in order to provide the correct coverage. An ensemble of 10,000 toy data sets was produced for each point of the oscillation parameter grid, fine enough to describe the variation of $X_{\rm crit}(\vec{o})$ as a function of the free parameters.

The flux, cross section, and detector systematic parameters were sampled from the same multivariate Gaussian with mean μ and covariance V used as prior p.d.f. in the marginalization method, as described above. The oscillation parameters constrained by external measurements, such as $\sin^2\theta_{12}$, Δm^2_{21} and $\sin^2\theta_{13}$, were sampled by using the p.d.f.s with parameters given in Table XVIII. The remaining oscillation parameters were sampled using the distribution of $-2\Delta\ln\mathcal{L}(\vec{\sigma})$ obtained from the fit of the T2K data. This method will be referred as "posterior predictive".

Since the Feldman-Cousins method is computationally intensive, it is used only for the most important result of the oscillation analysis, i.e. the confidence intervals as a function of δ_{CP} and MO. For all the other results, the constant $\Delta\chi^2$ method, which is more practical and provides good coverage to a first order approximation, is used.

B. Bayesian analysis

The Bayesian analysis performs the integration of Eq. (12) using a Markov chain Monte Carlo (MCMC) method. The Metropolis-Hastings algorithm [81] is used to populate the space of the oscillation and nuisance parameters, distributed according to the posterior probability density function.

This algorithm uses a weighted random walk to explore the parameter space with a chain of many points, X_i. A new proposed step to X_{i+1} is accepted with a probability equal to the minimum between 1 and $P(X_{i+1})/P(X_i)$; i.e. it is accepted with 100% probability when $P(X_{i+1}) > P(X_i)$ and with a probability equal to $P(X_{i+1})/P(X_i)$ when $P(X_{i+1}) < P(X_i)$. When a step to X_{i+1} is rejected, the point X_i is repeated in the chain, and a new step is proposed again from the previous step X_i. Typically, a chain consists of 10^6–10^7 steps. The population of accepted points in parameter space thus constructed is distributed according to the posterior probability density.

Credible intervals are built by selecting the highest density region in the space of the parameters of interest, typically one or two, that contains $\alpha\%$ of the points. A kernel density estimator (KDE) [82,83] is used to extract the most probable values of the oscillation parameters of interest. A KDE p.d.f. is built by smearing the step points with a Gaussian function which has a width inversely proportional to the number of points. The most probable values of the parameters of interest were found by maximizing the KDE p.d.f. using MINUIT [84].

C. Analysis templates

The three analyses use different far detector templates. All of them use the reconstructed neutrino energy, $E^{\rm rec}_\nu$, for the ν_μ and $\bar{\nu}_\mu$ candidate samples, while different templates are used for the ν_e and $\bar{\nu}_e$ candidate samples. One of the two frequentist analyses and the MCMC Bayesian analysis use $E^{\rm rec}_\nu$ and the angle between the lepton and the neutrino beam direction, $\theta_{\rm lep}$. The choice of these two parameters is due to the fact that $E^{\rm rec}_\nu$ is important to infer the oscillation probability function, which depends on the true neutrino energy. $\theta_{\rm lep}$ is used because it provides additional separation between ν and $\bar{\nu}$ candidate events. The ν and $\bar{\nu}$ cross sections differ as a function of Q^2, and leptons produced in ν interactions tend to be emitted at larger angles than those produced in $\bar{\nu}$ interactions.

As was shown in Table XIV, while the number of $\bar{\nu}_\mu \to \bar{\nu}_e$ in the ν mode is negligible, in the $\bar{\nu}$ mode, the number of oscillated ν_e is roughly 30% of the number of oscillated $\bar{\nu}_e$, and thus it is crucial to use templates which are able to distinguish between the two cases. In Fig. 28, the expected $\{E^{\rm rec}_\nu, \theta_{\rm lep}\}$ distribution in the single-ring e-like sample in the $\bar{\nu}$ mode for the signal ($\bar{\nu}_\mu \to \bar{\nu}_e$) and for the oscillated ν_e background is shown.

In Fig. 29, the 2D templates for the three ν_e candidate samples are shown. The ν_e CC1π^+ sample has no events with reconstructed energy below 400 MeV due to the Δ^{++} production requirement in Eq. (5) used to reconstruct the neutrino energy.

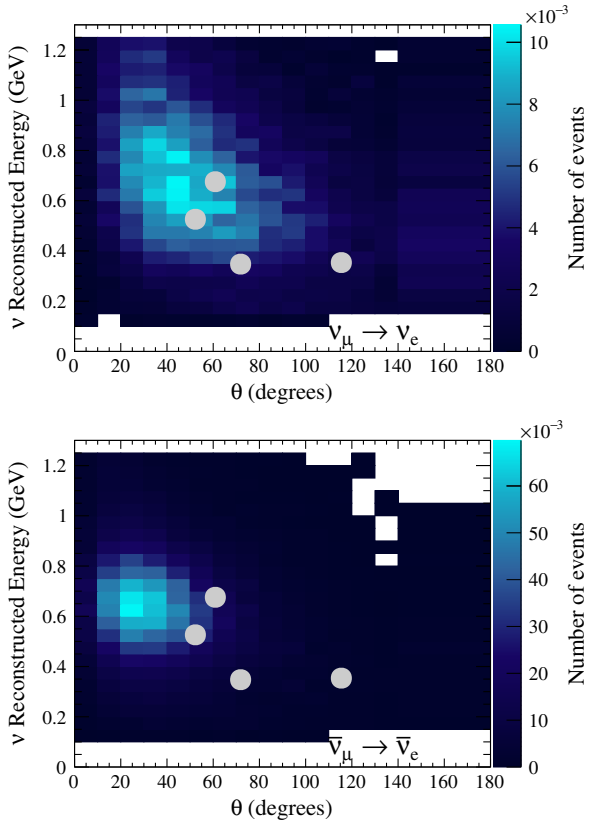

FIG. 28. Expected $\{E^{\rm rec}_\nu, \theta_{\rm lep}\}$ distributions for the signal $\bar{\nu}_\mu \to \bar{\nu}_e$ (top) and wrong-sign background $\nu_\mu \to \nu_e$ (bottom) in the e-like CCQE-like selection in the $\bar{\nu}$ mode. The superimposed gray dots correspond to the data. The expectation is based on the parameters of Table XIII.

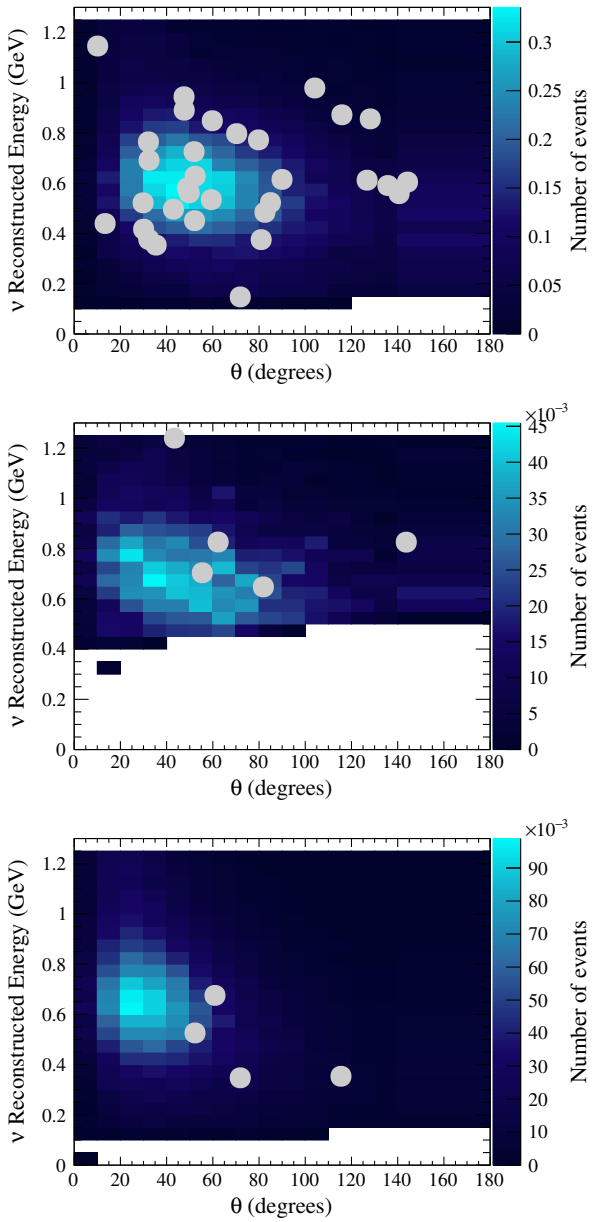

FIG. 29. $\{E_\nu^{\rm rec}, \theta_{\rm lep}\}$ templates for the ν_e CCQE-like (top), ν_e CC1π^+ (middle) in the ν-mode, and $\bar{\nu}_e$ CCQE-like (bottom) in $\bar{\nu}$-mode candidate samples. Both signal and background events are included in the expected distributions based on the oscillation parameters of Table XIII. The superimposed gray dots correspond to the data.

The second frequentist analysis also uses 2D templates, but instead of using $E_\nu^{\rm rec}$, it uses lepton momentum, $p_{\rm lep}$, and $\theta_{\rm lep}$. This choice provides similar ν–$\bar{\nu}$ separation as $\{p_{\rm lep}, \theta_{\rm lep}\}$ templates are directly related to $E_\nu^{\rm rec}$. Indeed, a particular value of $E_\nu^{\rm rec}$ corresponds to a slice in the $\{p_{\rm lep}, \theta_{\rm lep}\}$ phase space. For this reason, $\{E_\nu^{\rm rec}, \theta_{\rm lep}\}$ and $\{p_{\rm lep}, \theta_{\rm lep}\}$ analysis templates provide very similar sensitivities to the oscillation parameters.

Finally, another difference among the three analyses is that the Bayesian analysis performs a simultaneous fit of the ND280 and SK data sets in order to validate the extrapolation of the flux, cross section, and detector systematic parameters from the near to far detector. The other two analyses perform a fit of the far detector data using the priors obtained by the near detector data fit for the flux and cross section systematic parameters. The two methods show very good agreement in the estimation of flux and cross section parameters as was shown in Sec. V.

D. Systematic uncertainties on the oscillation analyses

The systematic uncertainties of the oscillation analysis are separated into four different categories: flux, cross section, and SK detector and momentum scale parameters. The flux and many of the cross section parameters (mentioned in Table IX) are correlated by the ND280 measurements as shown in Sec. V, effectively reducing the systematic uncertainties of the measurements at SK.

The flux parameters assign the systematic uncertainties on the neutrino and antineutrino flux. These parameters are applied as normalization factors for different neutrino flavor subcategories and true energy bins. The flux uncertainties at SK are constrained by the ND280 measurements.

The cross section parameters are applied based on the true neutrino interaction category of each event. Most of these parameters are normalization factors, but some also contain shape information, modifying the kinematic distributions in $p_{\rm lep} - \theta_{\rm lep}$ and $E_\nu^{\rm rec}$ probability density functions for corresponding oscillation analysis samples.

There are several categories of SK uncertainty: detector efficiency, FSI, secondary interaction (SI), and photonuclear (PN) effect uncertainties. The update on the SK detector efficiency uncertainty related to the addition of the CC1π e-like sample is described in Sec. VI C. In addition, the FSI, SI, and PN effect uncertainties on the CC1π^+ e-like sample are evaluated using the same method introduced in Ref. [27]. The increased uncertainties for this sample are mainly due to the larger backgrounds affecting it and to larger uncertainties on the pion FSI and SI as shown in Table XIX, where the SK systematic uncertainties are separated into the SK detector and the FSI + SI + PN contributions.

The SK energy scale uncertainty is applied independently from other parameters. The energy scale uncertainty is applied as a normalization of $E_\nu^{\rm rec}$ for each event, which may vary the total event rate by shifting the events into the cut regions of the visible energy and reconstructed neutrino energy selection criteria. The SK energy scale uncertainty is estimated to be 2.4%.

The effects of the systematic uncertainties on the predicted event rates of the ν- and $\bar{\nu}$-mode samples are summarized in Tables XIX and XX, respectively. The 1σ uncertainties are obtained by throwing large sets of toy experiments, varying only the selected systematic parameters for each experiment, and calculating the relative uncertainties from the distributions of the event rates.

TABLE XIX. Effect of 1σ variation of the systematic uncertainties on the predicted event rates of the ν-mode samples.

	ν_e CCQE-like	ν_μ	ν_e CC1π^+
Source of uncertainty	$\delta N/N$	$\delta N/N$	$\delta N/N$
Flux (w/ ND280 constraint)	3.7%	3.6%	3.6%
Cross section (w/ ND280 constraint)	5.1%	4.0%	4.9%
Flux+cross section			
(w/o ND280 constraint)	11.3%	10.8%	16.4%
(w/ ND280 constraint)	4.2%	2.9%	5.0%
FSI + SI + PN at SK	2.5%	1.5%	10.5%
SK detector	2.4%	3.9%	9.3%
All			
(w/o ND280 constraint)	12.7%	12.0%	21.9%
(w/ ND280 constraint)	5.5%	5.1%	14.8%

The anticorrelations between flux and cross section parameters reduce the systematic uncertainties when both these sources are taken into account.

IX. SENSITIVITY OF OSCILLATION PARAMETERS TO NEUTRINO INTERACTION MODELING

The neutrino interaction uncertainties are one of the main contributors to the systematic uncertainty on all oscillation measurements, and there is a global effort underway to improve the understanding of neutrino cross sections. This has led to the creation of a number of interaction models which can, at least partially, describe existing cross section data but which also produce different predictions for the oscillated event rates and spectra at SK. This analysis uses the high statistics near detector data to constrain both the flux and cross section model uncertainties, improving the prediction of the far detector event rate and reducing the uncertainty on that prediction. However, the near and far detectors observe different neutrino energy spectra (mainly due to oscillations), so the underlying neutrino interactions they sample will be different. The different design of the two detectors also means that they are sensitive to different regions of the lepton kinematic phase space. The near detector fit therefore tunes the flux and cross section models to a set of neutrino interactions and a lepton kinematic phase space that is not the same as that observed at the far detector. These differences could then be incorrectly attributed to neutrino oscillation effects in the oscillation analysis, which would result in biased oscillation measurements.

TABLE XX. Effect of 1σ variation of the systematic uncertainties on the predicted event rates of the $\bar{\nu}$-mode samples.

	$\bar{\nu}_e$ CCQE-like	$\bar{\nu}_\mu$
Source of uncertainty	$\delta N/N$	$\delta N/N$
Flux (w/ ND280 constraint)	3.8%	3.8%
Cross section (w/ ND280 constraint)	5.5%	4.2%
Flux+cross section		
(w/o ND280 constraint)	12.9%	11.3%
(w/ ND280 constraint)	4.7%	3.5%
FSI + SI + PN at SK	3.0%	2.1%
SK detector	2.5%	3.4%
All		
(w/o ND280 constraint)	14.5%	12.5%
(w/ ND280 constraint)	6.5%	5.3%

This has been studied in a phenomenological context using a simplified oscillation analysis, summarized in Ref. [29]. The results of the studies show that long-baseline experiments may be biased by cross section model choices, as might be expected from the qualitative arguments above. Given the potential impact of these model choices, it is important to investigate these issues using the full T2K oscillation analysis framework. This has been performed for a range of neutrino interaction model variations, which were discussed in Sec. III B.

A. Production and analysis of simulated data sets

The analysis is performed using replica data sets created by changing one part of the nominal MC. Simulated data are created by applying the event selection described in Secs. IV B and VI to the nominal T2K MC. A weight is then applied to each selected event, calculated as the ratio of the altered interaction model to the nominal cross section model. For the SK simulated data, the relevant oscillation probability is also applied. This produces event samples corresponding to the alternative interaction model. An example of this is shown in Fig. 30 for the ND280 samples, where the left plot shows the ratio of the alternative 2p2h simulated data to the nominal MC for the FGD1 CC-0π sample, while the right shows the ratio for the alternative 1p1h model.

For each interaction model variation, simulated data are generated at both the ND280 and SK. The nominal flux and interaction models are then fit to the ND280 simulated data using the procedure described in Sec. V. The result is then used as the ND280 input to the oscillation analysis, described in Sec. VIII A. The SK simulated data are fit to produce a set of likelihood contours for the oscillation parameters. These likelihood contours are then compared to the expected likelihood contour for fits where the nominal MC is used as data. For each oscillation parameter, a bias is calculated, defined as the difference in the parameter best-fit point between the simulated data fit and the nominal data fit, divided by the 1σ uncertainty on that parameter from the nominal fit.

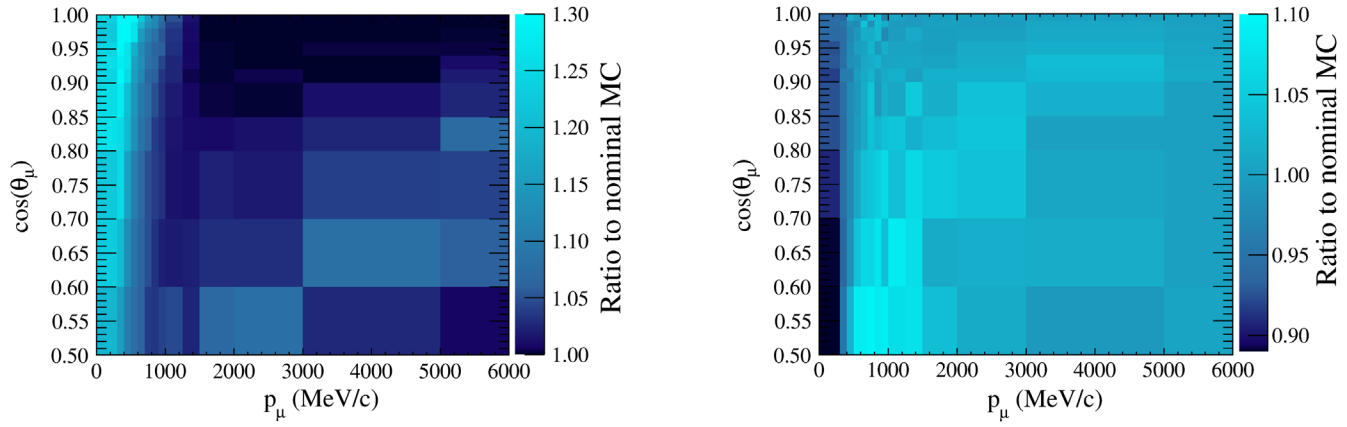

FIG. 30. Ratio of the alternative 2p2h simulated data (left) and alternative 1p1h simulated data (right) to the nominal MC, shown as a function of reconstructed lepton kinematics for the FGD1 CC-0π sample.

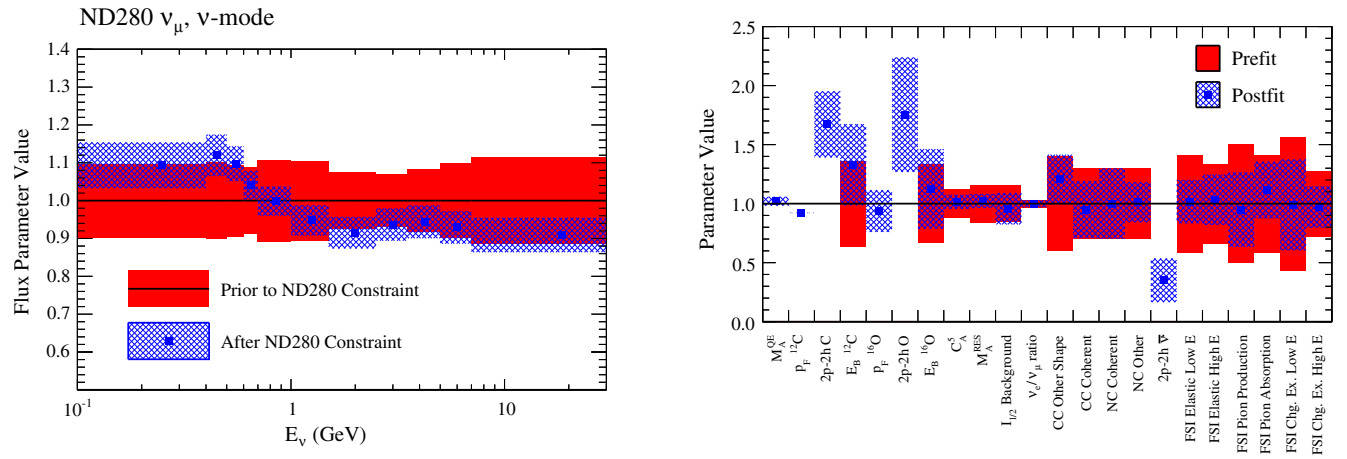

FIG. 31. The nominal values (red) and postfit values (blue) of the ND 280ν-mode ν_μ flux (left) and the cross section (right) parameters, shown as a fraction of their nominal value, following the near detector fit to the alternative 2p2h ND280 simulated data.

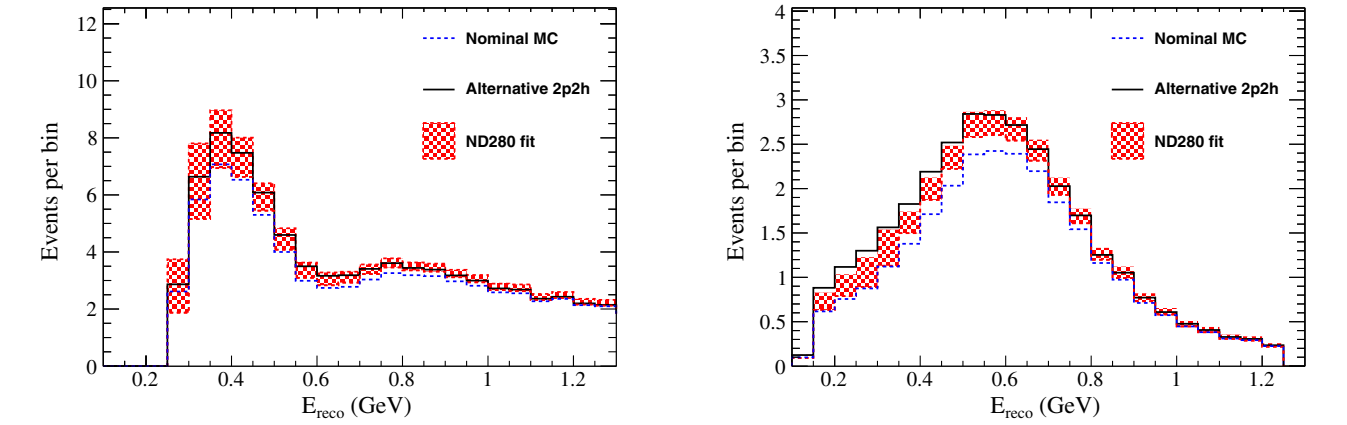

FIG. 32. Single-ring expected event spectrum at SK as a function of E_ν^{rec}, assuming CCQE kinematics, for the selected μ-like (left) and e-like (right) events in the ν mode. The nominal SK prediction is shown by the dashed blue line, the SK simulated data are shown by the solid black line, and the prediction from the ND280 simulated data fit is shown by the hashed red region.

TABLE XXI. Oscillation parameter values used as inputs for the studies of simulated data.

Parameter	Maximal oscillation	Nonmaximal oscillation
$\sin^2(\theta_{23})$	0.523	0.6
δ_{CP} (rad)	−1.601	−1.601
$\sin^2(\theta_{13})$	0.0217	
$\sin^2(\theta_{12})$	0.304	
Δm^2_{21} (10^{-5} eV^2)	7.53	
Δm^2_{32} (10^{-3} eV^2)	2.51	

B. Results

Results from the ND280 fit are used for central values and uncertainties for the neutrino flux and cross section model parameters. When fitting the nominal MC, the parameter estimators are found to be unbiased, while their uncertainties are reduced. For the fits to simulated data generated from alternative models, the values of both the flux and cross section parameters change, as shown in Fig. 31. These show the results obtained by fitting the data generated using the alternative 2p2h model, rather than the nominal model. Figure 31 demonstrates how differences between the true and model interaction cross sections can be absorbed by both the flux and cross section parameters.The ND280 fit result is used to predict the unoscillated event spectra at SK, producing the ν-mode ν_μ and ν_e event spectra shown in Fig. 32. The predicted spectra fall between the nominal and 2p2h models, and the uncertainty typically covers much of the difference between the models.

To evaluate possible bias in the oscillation parameter estimators, a fit is performed with SK simulated data. The likelihood surfaces for the oscillation parameters of interest obtained by this fit are shown in Fig. 33. These results use the true parameter values listed in the "maximal oscillation" column of Table XXI. Figure 33 shows that if the alternative 2p2h model is correct, using the Nieves model in the nominal MC produces small (∼2%) biases in the measured values of $\sin^2\theta_{23}$ and Δm^2_{32} (<1%). The study also shows a change in the δ_{CP} likelihood contour, increasing the exclusion around $\delta_{CP} = \pi/2$ by 1.2 units of $\Delta\chi^2$. Overall, as seen in the bottom right of Fig. 33, the effect on the appearance analysis is small, compared to the statistical uncertainty.

Figure 34 shows fits to the same alternative 2p2h simulated data as in Fig. 33, but using the nonmaximal oscillation parameters from Table XXI. For nonmaximal disappearance, a larger change is observed in the $\sin^2\theta_{23}$

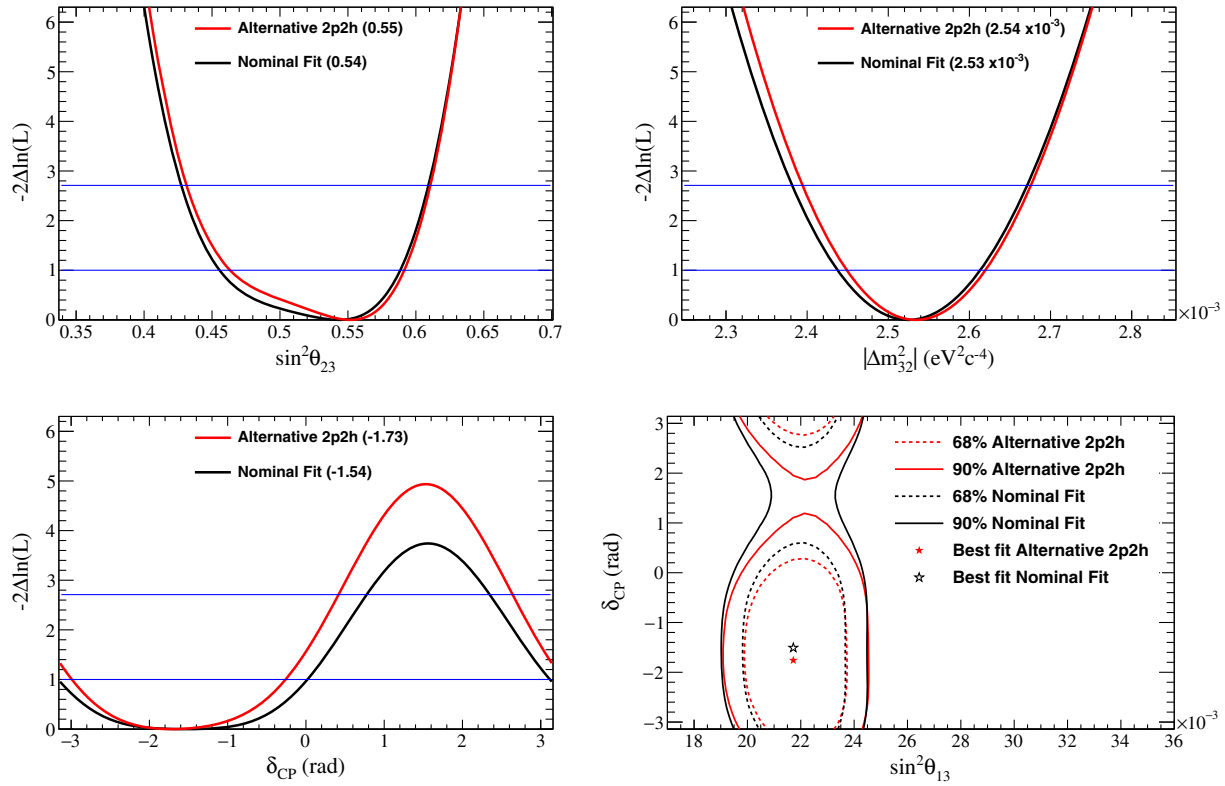

FIG. 33. The likelihood surfaces (red) from the oscillation fit of the alternative 2p2h simulated data at SK, using the result of the fit to the ND280 simulated data as an input. The oscillation parameters of Table XXI (maximal mixing) were used. The likelihood surfaces from the nominal fit are shown by the black line. The contours for $\sin^2\theta_{23}$ (top left), Δm^2_{32} (top right), δ_{CP} (bottom left), and δ_{CP} vs $\sin^2\theta_{13}$ (bottom right) are shown. For the one-dimensional likelihoods, the point of minimum $\Delta\chi^2$ is given in each legend.

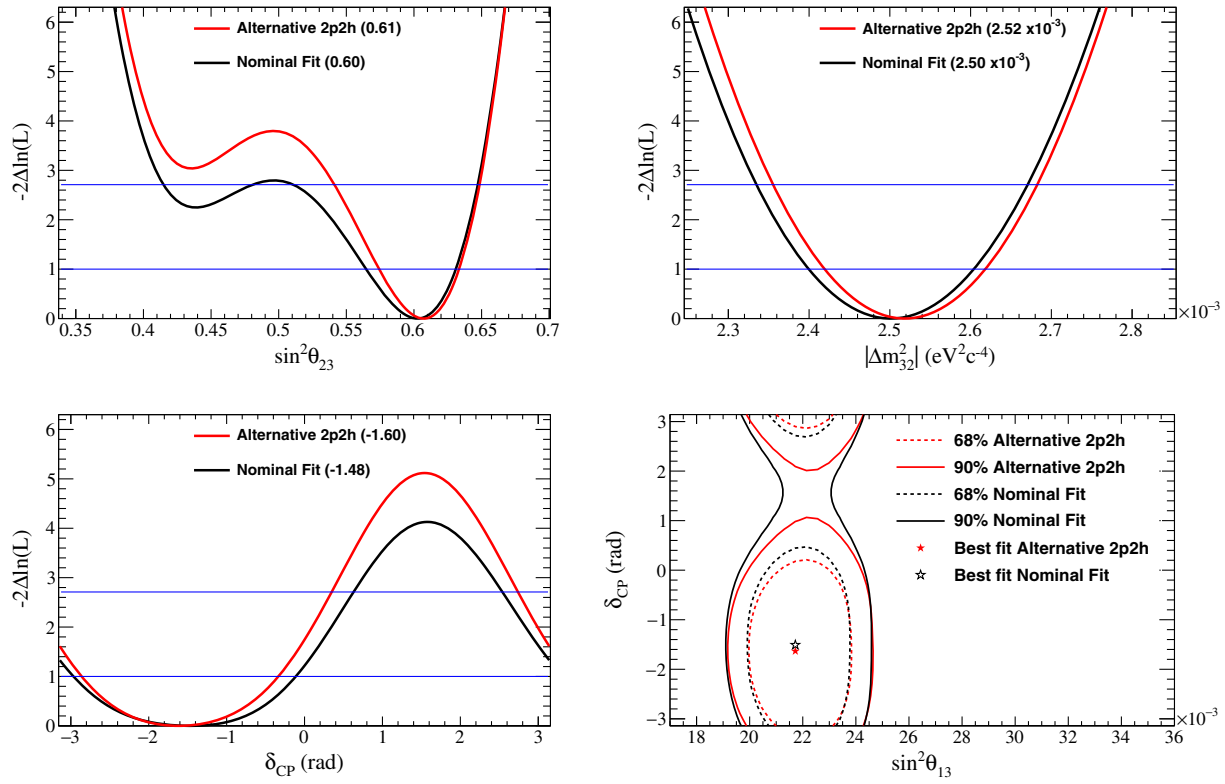

FIG. 34. The likelihood surfaces (red) from the oscillation fit of the alternative 2p2h simulated data at SK, using the result of the fit to the ND280 simulated data as an input. The oscillation parameters of Table XXI (nonmaximal mixing) were used. The likelihood surfaces from the nominal fit are shown by the black line. The contours for $\sin^2\theta_{23}$ (top left), Δm^2_{32} (top right), δ_{CP} (bottom left), and δ_{CP} vs $\sin^2\theta_{13}$ (bottom right) are shown. For the one-dimensional likelihoods, the point of minimum $\Delta\chi^2$ is given in each legend.

likelihood contour. The effect on the point estimate and 68% C.L. interval is relatively small.

Figure 35 shows the results of the fits to the alternative 1p1h simulated data set described in Sec. III B. The alternative 1p1h model changes the T2K MC as a function of both the neutrino energy and the angle at which the lepton is produced relative to the neutrino direction. Similarly to the alternative 2p2h case, this model variation introduces a small bias in the measurement of Δm^2_{32} and has a small effect on the δ_{CP} likelihood contour.

C. Summary

Detailed studies have been performed to evaluate the sensitivity of the T2K oscillation analysis to neutrino interaction modeling. By using the near detector data to estimate flux and interaction model parameters, the oscillation parameter estimates are found to be essentially unaffected by changes to the interaction model. The largest observed effect on the oscillation parameter likelihood contours is shown in Fig. 34, while Fig. 35 is more representative of the majority of the model variations discussed in Sec. III B.

A summary of the maximum bias observed for all of the alternative models studied is shown in Table XXII. The bias is presented as a fraction of the expected 1σ uncertainty on each oscillation parameter and is the maximum bias seen from all true oscillation parameter values tested. T2K does not expect a significant constraint on δ_{CP} given the integrated POT available for this analysis. As a result, it is difficult to quantify the effect on δ_{CP} in a single number, and so this parameter is not included in the summary table. For reference, the largest effect observed for δ_{CP} is shown in Fig. 34.

X. $\bar{\nu}_e$ APPEARANCE ANALYSIS

T2K has already observed the ν_e appearance in a ν_μ beam [7], but no direct evidence of the $\bar{\nu}_e$ appearance has been reported so far. A search for this process, with the data collected by T2K in the $\bar{\nu}$ mode, has been performed using the analysis tools described in Sec. VIII.

In order to look for the $\bar{\nu}_e$ appearance independently from the ν_e appearance, a parameter β is introduced which multiplies the $\bar{\nu}_e$-appearance probability

$$P(\bar{\nu}_\mu \to \bar{\nu}_e) \to \beta \times P(\bar{\nu}_\mu \to \bar{\nu}_e). \tag{13}$$

In this analysis, β can have two values: $\beta = 0$, which corresponds to no $\bar{\nu}_\mu \to \bar{\nu}_e$ oscillations, and $\beta = 1$, which

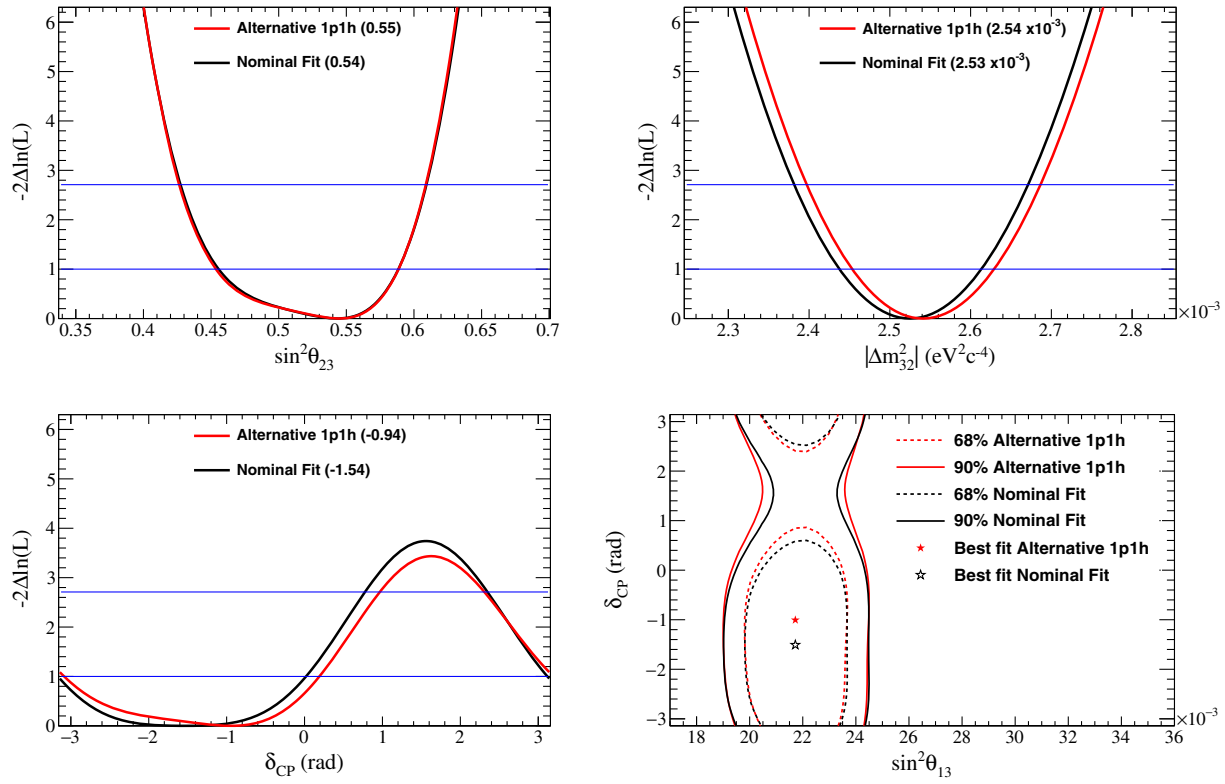

FIG. 35. The likelihood surfaces (red) from the oscillation fit of the alternative 1p1h simulated data at SK, using the result of the fit to the ND280 simulated data as an input. The oscillation parameters of Table XXI (maximal mixing) were used. The likelihood surfaces from the nominal fit are shown by the black line. The contours for $\sin^2\theta_{23}$ (top left), Δm^2_{32} (top right), δ_{CP} (bottom left), and δ_{CP} vs $\sin^2\theta_{13}$ (bottom right) are shown. For the one-dimensional likelihoods, the point of minimum $\Delta\chi^2$ is given in each legend.

corresponds to the appearance probability as predicted by the PMNS framework.

The two hypotheses are tested using rate-only and rate-plus-shape analyses. The test statistic is different in the two cases. The test statistic used in the rate-only analysis is the number of e-like candidates observed at SK in the $\bar{\nu}$ mode, while for the rate-plus-shape analysis, the likelihood ratio for the two hypotheses, assuming PMNS oscillations and no $\bar{\nu}_\mu \to \bar{\nu}_e$, is used:

$$\begin{aligned}\Delta\chi^2 &= \chi^2(\beta=0) - \chi^2(\beta=1) \\ &= 2[-\ln\mathcal{L}(\beta=0;x) + \ln\mathcal{L}(\beta=1;x)], \quad (14)\end{aligned}$$

A toy ensemble is generated according to the prior knowledge on the oscillation parameters defined in Sec. VII B for both values of β. The T2K information from the ν_μ-disappearance, $\bar{\nu}_\mu$-disappearance and ν_e-appearance[1] channels are taken into account by using a posterior predictive method [85]. In this method, the data from these channels are used to constrain the prior parameter space in generating the toy ensemble for the $\bar{\nu}_e$ sample while preserving their correlations.

The sensitivity of the analysis is computed by producing a simulated sample without statistical fluctuations using the values of the oscillation parameters defined in Table XIII. The test statistics for this particular data set are 6.28 expected $\bar{\nu}_e$ candidates for the rate-only analysis, corresponding to the total number of expected events in the $\bar{\nu}$

TABLE XXII. Summary of the maximum bias seen in oscillation parameters when fitting simulated data sets (defined in Sec. III B), presented as a fraction of the expected 1σ uncertainty on each parameter. Fits were performed for a number of true oscillation parameter assumptions. The numbers shown here are the maximum bias found for a given parameter and alternative model across all true oscillation parameter values tested.

	Maximum bias on parameter (σ)		
Alternative model	Δm^2_{32}	$\sin^2\theta_{23}$	$\sin^2\theta_{13}$
SF	0.09	0.17	0.17
Effective RPA	0.00	0.06	0.00
Alternative 1p1h	0.20	0.09	0.07
Alternative 2p2h	0.20	0.21	0.18
Delta-enhanced 2p2h	0.10	0.10	0.00
Not-Delta 2p2h	0.11	0.07	0.05

[1]Note that the e-like CC1π^+ sample was not included in this analysis; only CCQE-like samples were used.

TABLE XXIII. Expected and observed (data) p-values for the $\beta = 0$ and $\beta = 1$ hypotheses, for both rate-only and rate-plus-shape analyses. The expected p-values are estimated for the simulated data set defined in Table XIII.

	Rate only	Rate plus shape
Simulated sample		
$\beta = 0$	0.047	0.047
$\beta = 1$	0.52	0.41
Data		
$\beta = 0$	0.41	0.46
$\beta = 1$	0.21	0.07

TABLE XXIV. Point estimates and 1σ confidence intervals under the constant $\Delta\chi^2$ approximation from an analysis considering T2K oscillation data only.

	Normal ordering		Inverted ordering	
Parameter	Best fit	$\pm 1\sigma$	Best-fit	$\pm 1\sigma$
δ_{CP}	−1.791	[−2.789; −0.764]	−1.382	[−2.296; −0.524]
$\sin^2\theta_{13}$	0.0271	[0.0209; 0.0342]	0.0299	[0.0232; 0.0380]

mode in Table XIV, and $\Delta\chi^2 = 2.54$ for the rate-plus-shape analysis. When compared to the generated toy ensembles for the no-$\bar{\nu}_e$ appearance hypothesis, the p-values are 0.047 for both the rate-only and rate-plus-shape analyses. When compared with the toy ensemble generated with $\beta = 1$, p-values of 0.52 and 0.41 are found for the rate-only and rate-plus-shape analyses, respectively.

The same analysis is then applied to the e-like data selected in the $\bar{\nu}$ mode. The test statistics in data for the rate-only and rate-plus-shape analyses are $N^{\text{obs}} = 4$ $\bar{\nu}_e$ candidates and $\Delta\chi^2 = -2.51$, obtained from the $\{E_\nu^{\text{rec}}, \theta_{\text{lep}}\}$ distribution of the e-like candidates in the $\bar{\nu}$ mode shown in Fig. 28. As shown in Table XXIII, these test statistics return a p-value of 0.41 (0.46) for the $\beta = 0$ hypothesis for the rate-only (rate-plus-shape) analysis, while the p-value for $\beta = 1$ is 0.21 (0.07). This analysis shows that, with the available data, the rate-plus-shape analysis excludes $\beta = 1$ at 90% C.L.

The observed p-values for the $\beta = 0$ hypothesis are larger than expectation due to the lower than expected number of observed events in the e-like $\bar{\nu}$-mode sample. The lower p-value for the rate $\beta = 1$ hypothesis is driven by the larger discrepancy between the selected ν_e and $\bar{\nu}_e$ rate (32 and 4 events, respectively) than predicted by the simulated data set generated, even under the assumption of a maximal CP violation $\delta = -\pi/2$ (28.55 and 6.28 events, respectively). The p-value in the rate-plus-shape analysis for the $\beta = 1$ hypothesis is reduced further, due to the distribution of the $\bar{\nu}_e$-appearance candidates in the electron momentum and angle. Their distribution is more compatible with the background expected distribution, as shown in Fig. 19.

XI. JOINT NEUTRINO AND ANTINEUTRINO OSCILLATION ANALYSIS RESULTS

In this section, joint three-flavor oscillation analyses performed with both the frequentist and the Bayesian approaches are presented. The five SK samples introduced in Sec. VI are used, which allows the simultaneous study of the ν_e and $\bar{\nu}_e$ appearance channels and the ν_μ and $\bar{\nu}_\mu$ disappearance channels. The oscillation parameters $|\Delta m^2_{32}|$, $\sin^2\theta_{23}$, $\sin^2\theta_{13}$, δ_{CP}, and the mass ordering are determined with and without using the measurement of $\sin^2\theta_{13}$ from reactor experiments as a constraint.

A. Frequentist analysis

Although two frequentist analyses were introduced in Sec. VIII A, the results are similar, so detailed results are only presented for the analysis which uses $\{E_\nu^{\text{rec}}, \theta_{\text{lep}}\}$ templates in this section. Comparisons between both

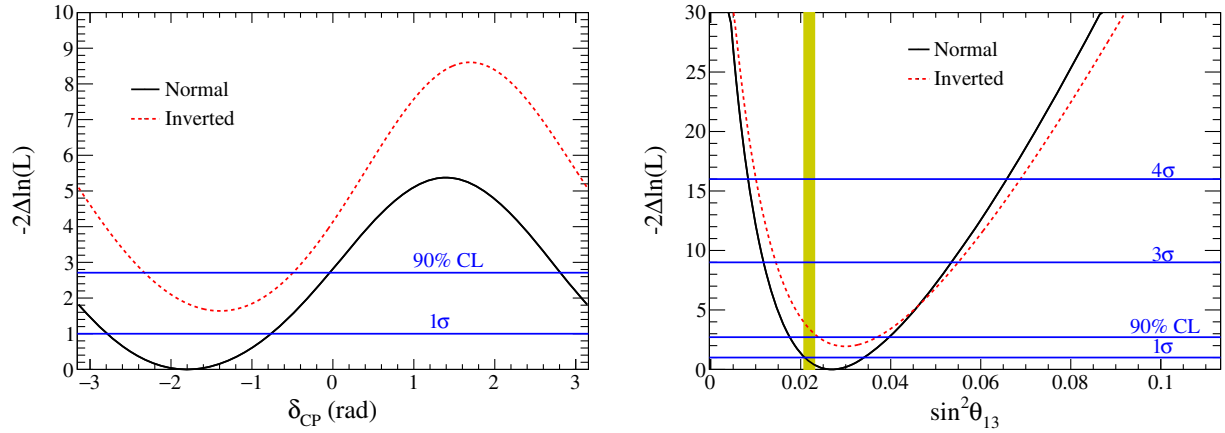

FIG. 36. One-dimensional $\Delta\chi^2$ surfaces for oscillation parameters δ_{CP} and $\sin^2\theta_{13}$ using T2K-only data. The yellow band on the right plot corresponds to the reactor value on $\sin^2\theta_{13}$ from the PDG 2015 [75].

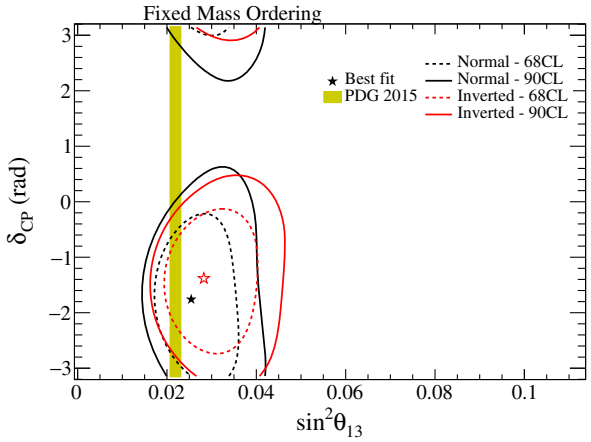

FIG. 37. Two-dimensional constant $\Delta\chi^2$ contours for oscillation parameters δ_{CP} and $\sin^2\theta_{13}$ using T2K data only. The yellow band corresponds to the reactor value on $\sin^2\theta_{13}$ from the PDG 2015 [75].

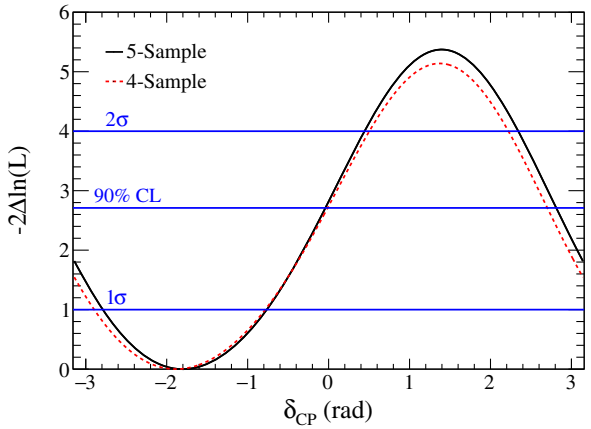

FIG. 38. A comparison of one-dimensional constant $\Delta\chi^2$ contours for normal ordering for δ_{CP} using T2K-only data for the four- and five-sample fits.

frequentist, and the Bayesian analysis are shown in Sec. XI C.

1. Results without reactor constraints

This section describes the results obtained by the frequentist analysis when only T2K data are used to estimate the oscillation parameters. The main parameters of interest in this case are δ_{CP} and $\sin^2\theta_{13}$ that can be directly compared to the reactor measurements. The point estimates for these oscillation parameters and the constant $\Delta\chi^2 = 1$ intervals are given for normal and inverted ordering in Table XXIV. The $\Delta\chi^2$ surfaces are shown in Fig. 36. These intervals have been produced via marginalization of all nuisance and oscillation parameters which are not of interest, as described in Sec. VIII A.

Two-dimensional contours of constant $\Delta\chi^2$ for the parameters δ_{CP} and $\sin^2\theta_{13}$, along with a comparison with the constraint on $\sin^2\theta_{13}$ from reactor experiments, are shown in Fig. 37. The point estimate and constant $\Delta\chi^2$ confidence intervals of $\sin^2\theta_{13}$ from T2K data only are slightly larger than what is found by the reactor experiments. However, the T2K-only measurement of $\sin^2\theta_{13}$ is still consistent with the reactor measurement at the 68% confidence level.

As mentioned above, in this analysis, a fifth sample selecting ν_e candidates at SK with one delayed Michel electron in the final state has been added for the first time. A comparison of the $\Delta\chi^2$ surface for δ_{CP} only including the four single-ring samples used in previous analyses and the results obtained with the inclusion of the fifth sample is shown in Fig. 38. As expected, a small improvement is observed when the new sample is included.

Figure 39 shows a comparison of the constraints in the δ_{CP}–$\sin^2\theta_{13}$ plane when appearance channels taken in the ν mode and in $\bar{\nu}$ mode are considered independently. Both ν- and $\bar{\nu}$-mode disappearance channels are used in both fits.

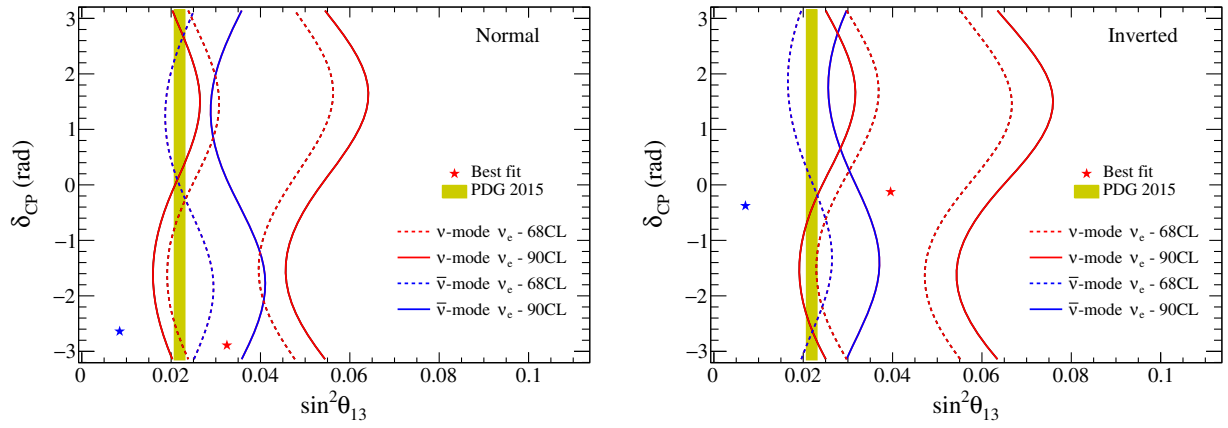

FIG. 39. Contours in the $\sin^2\theta_{13}$–δ_{CP} plane using T2K-only data, obtained by analysing either the ν- or $\bar{\nu}$-mode appearance data sets, are compared for both orderings. Both ν- and $\bar{\nu}$-mode disappearance data sets were used in all fits. The yellow band corresponds to the reactor value on $\sin^2\theta_{13}$ from the PDG 2015 [75].

TABLE XXV. Best-fit results and the 1σ confidence interval of the T2K data fit with the reactor constraint with normal and inverted hypotheses.

	Normal ordering		Inverted ordering	
Parameter	Best-fit	$\pm1\sigma$	Best-fit	$\pm1\sigma$
δ_{CP}	−1.728	[−2.538; −0.877]	−1.445	[−2.170; −0.768]
$\sin^2\theta_{23}$	0.550	[0.465;0.601]	0.5525	[0.470;0.601]
Δm^2_{32} (10^{-3} eV$^2/c^4$)	2.54	[2.460;2.621]	2.51	[2.429;2.588]

The ν- and $\bar{\nu}$-mode data sets alone prefer different values of $\sin^2\theta_{13}$, which are driven by the absolute appearance rate. It is clear that the $\bar{\nu}$-mode appearance sample does not have the power to exclude a zero value of $\sin^2\theta_{13}$ by itself. In either case, the reactor measurement of $\sin^2\theta_{13}$ sits near the upper and lower 68% confidence contours for the $\bar{\nu}$-mode and ν-mode samples, respectively.

2. Results with reactor constraints

This section describes the oscillation parameters obtained by the T2K data fit where $\sin^2\theta_{13}$ is marginalized using the reactor constraint given in Table XVIII. The best-fit values of the T2K data with the reactor constraint are summarized in Table XXV.

Figure 40 shows the 90% constant $\Delta\chi^2$ surface in the $\sin^2\theta_{23}$-Δm^2_{32} plane, assuming normal mass ordering. The interval is compared with other experiments, showing good agreement with IceCube and SK and some tension with MINOS and NOνA.

The NOνA Collaboration published ν_μ-disappearance results disfavoring maximal mixing for $\sin^2\theta_{23}$ at 2.6σ [86]. The T2K data in the ν_μ- and $\bar{\nu}_\mu$-disappearance channels, together with the T2K best fit and the expected

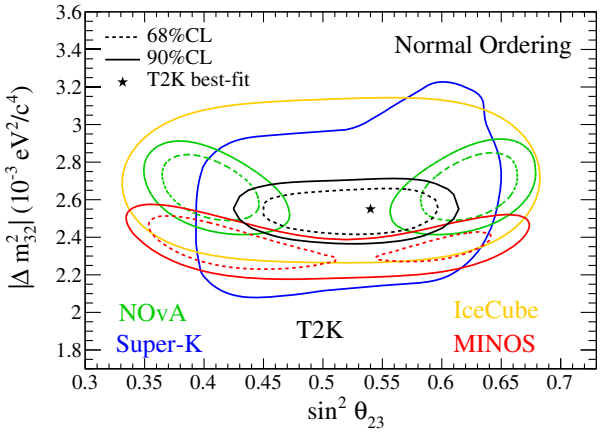

FIG. 40. Allowed region at 90% confidence level for oscillation parameters $\sin^2\theta_{23}$ and Δm^2_{32} using T2K data with the reactor constraint ($\sin^2(2\theta_{13}) = 0.085 \pm 0.005$). The normal mass ordering is assumed, and the T2K results are compared with NOνA [86], MINOS [4], Super-K [87], and IceCube [88].

spectrum produced using the NOνA best-fit value for $\sin^2\theta_{23}$ (higher octant) and Δm^2_{32}, are shown in Fig. 41.

Figure 42 shows the 2D $\sin^2\theta_{13}$–δ_{CP} confidence level contours for the data fit including the reactor constraint. The comparisons with the four-sample joint fit are also shown to demonstrate the effect of the inclusion of the CC1π^+ e-like sample in the appearance analysis. Compared to the best-fit results obtained with the T2K-only data fit in Sec. XI A 1, the inclusion of the CC1π^+ e-like sample in the data fit with the reactor constraint results in a shift of the best-fit value for the δ_{CP} phase toward the maximally violating phase of $-\pi/2$.

Since there is a physical boundary at $\delta_{CP} = \pm\frac{\pi}{2}$, calculating the coverage near the boundary using a Gaussian approximation may not produce accurate results. To solve this problem, the coverage of the one-dimensional $\Delta\chi^2$ distribution as a function of δ_{CP} is computed using the Feldman-Cousins approach, described in Sec. VIII. In order to perform the study, 10,000 toy MC experiments were generated for different values of δ_{CP} and the mass ordering. The one-dimensional $\Delta\chi^2$ surface obtained with the Feldman-Cousins approach is used to evaluate the 90% confidence intervals for δ_{CP} in both ordering cases, as shown in Fig. 43. In this analysis, CP-conserving values of $\delta_{\rm CP} = 0, \pi$ are excluded at 90% and 2σ confidence levels, respectively. Values of $\delta_{\rm CP}$ in the intervals $[-2.95, -0.44]$ ($[-1.47, -1.27]$) are allowed at 90% confidence for normal (inverted) ordering.

A useful way to visualize the results is to compare the observed number of events in the ν-mode (in both CCQE-like and CC1π^+-like samples) and $\bar{\nu}$-mode e-like samples with the expected events for different values of $\delta_{\rm CP}$, $\sin^2\theta_{23}$, and mass ordering. As is shown in Fig. 44, the T2K data fall outside the physically allowed region.

In order to quantify whether the T2K data set is consistent with the PMNS framework in terms of significance, an additional toy MC study was performed. An ensemble of 10,000 simulated data sets was obtained in the same way as described in Sec. VIII for the Feldman-Cousins method, with $\delta_{CP} = -\pi/2$ and normal mass ordering. The values of $-2\Delta\ln L$ that contain 68.3% and 95.5% of the MC toys were computed and compared to the distribution obtained with the fit of the T2K data set. As shown in Fig. 45, the T2K data $-2\Delta\ln L$ distribution shows a less extreme fluctuation than at least 5% of the toys MC

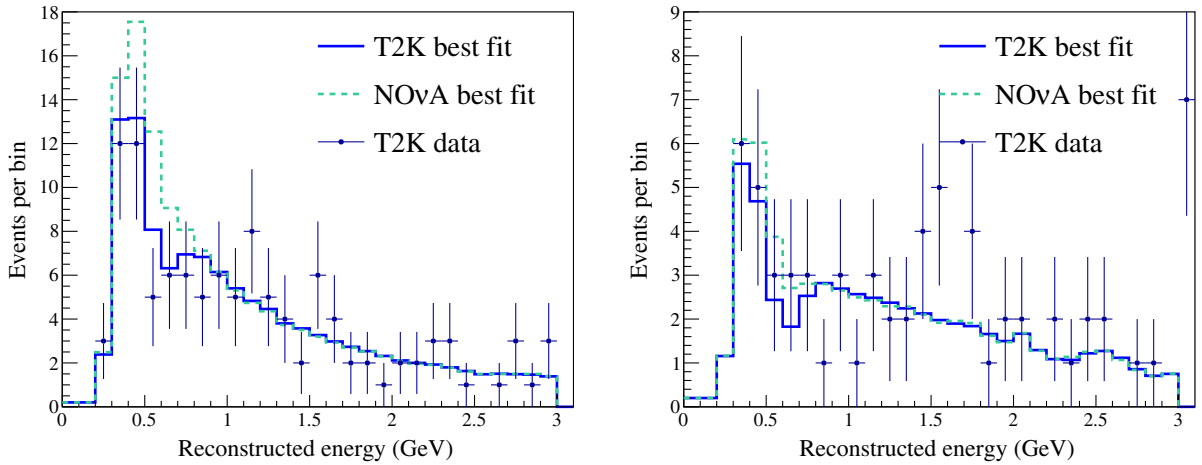

FIG. 41. Comparison of the T2K data in ν_μ (left) and $\bar{\nu}_\mu$ (right) disappearance channels with the expected spectra obtained with the T2K most probable values of the oscillation parameters and using the NOνA most probable values for $\sin^2\theta_{23}$ (higher octant) and Δm^2_{32} taken from Ref. [86].

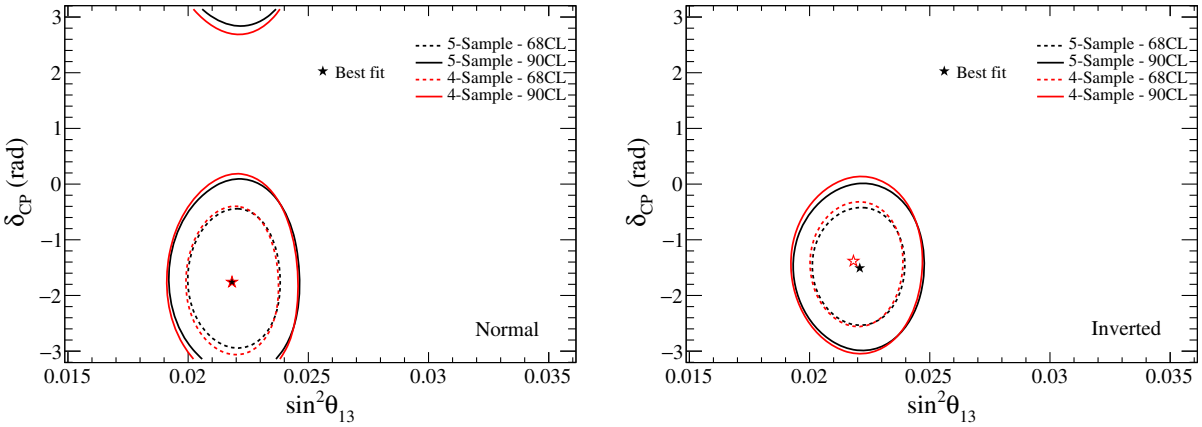

FIG. 42. A comparison of two-dimensional constant $\Delta\chi^2$ contours in the δ_{CP}–$\sin^2\theta_{13}$ plane using T2K data with the reactor constraint, for both four-sample (red) and five-sample (black) analyses with normal (left) and inverted (right) mass ordering hypotheses. The contours are produced by marginalizing the likelihood with respect to all parameters other than the parameters of interest.

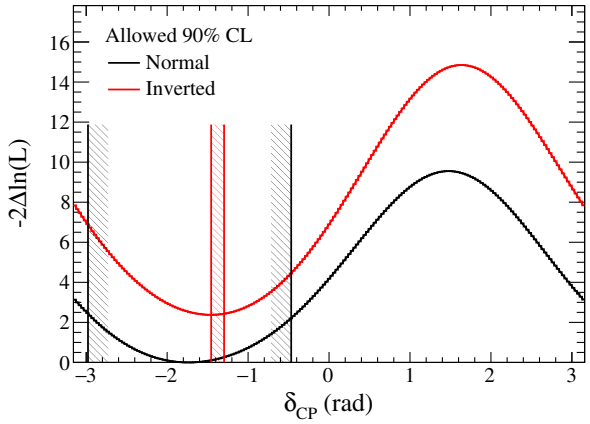

FIG. 43. One-dimensional $\Delta\chi^2$ surfaces for oscillation parameter δ_{CP} using T2K data with the reactor constraint. The critical $\Delta\chi^2$ values obtained with the Feldman-Cousins method are used to evaluate the 90% confidence level with the proper coverage.

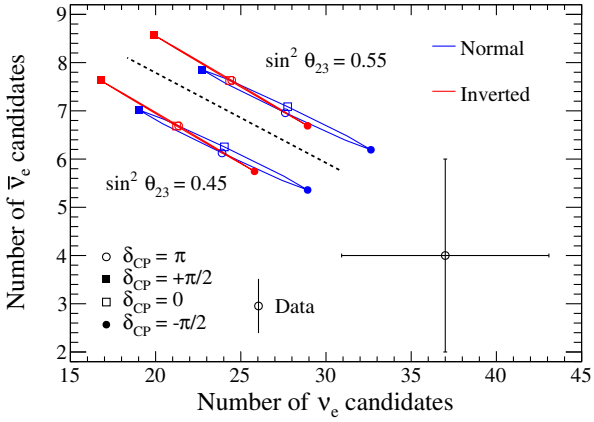

FIG. 44. Total predicted $\overset{(-)}{\nu}_e$-appearance event rates in the ν-mode samples and in the $\bar{\nu}$-mode sample as a function of δ_{CP} for different values of $\sin^2\theta_{23}$ and both mass orderings, compared to T2K data. The dashed line distinguishes the two solutions for the octant of θ_{23}.

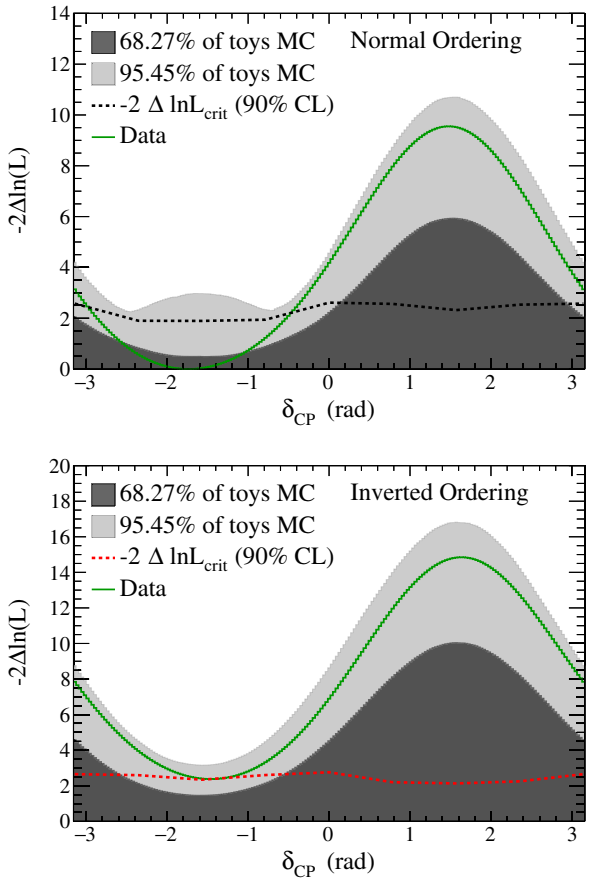

FIG. 45. One-dimensional marginal $\Delta\chi^2$ surfaces for oscillation parameters δ_{CP} and $\sin^2\theta_{13}$ using T2K data with the reactor constraint. The contour is produced by marginalizing the likelihood with respect to all parameters other than the parameter of interest. The red line shows the critical $\Delta\chi^2$ values obtained with the Feldman-Cousins method, used to evaluate the 90% confidence level with the proper coverage. The green line shows the $\Delta\chi^2$ obtained with the fit to the T2K data.

for all the values of δ_{CP} and mass ordering;, i.e. if the experiment is repeated many times and the true value is $\delta_{CP} = -\pi/2$ with normal ordering, more than 5% of the experiments are expected to show a more extreme statistical fluctuation than the current T2K data set over the whole range of δ_{CP} and mass ordering. From Fig. 45, the fraction of experiments that would exclude $\delta_{CP} = 0, \pi$ at 90% or 2σ confidence level can be estimated. Assuming a true value of δ_{CP} of-$\pi/2$ and normal ordering, 24.3% (21.3%) of toy MC experiments exclude $\delta_{\mathrm{CP}} = 0$ (π) at 90% C.L. The same can be repeated for different values of δ_{CP} and mass ordering as shown in Table XXVI.

TABLE XXVI. The fraction of toy experiments for which $\delta_{CP} = 0, \pi$ and normal and inverted ordering are excluded at 90% and 2σ confidence is shown for different true values of δ_{CP} and mass ordering. 10,000 toy experiments are used for each set of values.

True: $\delta_{CP} = -\pi/2$—normal ordering			
δ_{CP}	Ordering	90% C.L.	2σ C.L.
0	Normal	0.243	0.131
π	Normal	0.216	0.105
0	Inverted	0.542	0.425
π	Inverted	0.559	0.436
True: $\delta_{CP} = 0$—normal ordering			
δ_{CP}	Ordering	90% C.L.	2σ C.L.
0	Normal	0.104	0.0490
π	Normal	0.130	0.0591
0	Inverted	0.229	0.137
π	Inverted	0.205	0.122
True: $\delta_{CP} = -\pi/2$—inverted ordering			
δ_{CP}	Ordering	90% C.L.	2σ C.L.
0	Normal	0.124	0.0515
π	Normal	0.102	0.0413
0	Inverted	0.290	0.194
π	Inverted	0.308	0.207

B. Bayesian analysis

1. Results without reactor constraints

This section describes the results obtained by the Bayesian analysis when using only T2K data to estimate the parameters $\sin^2\theta_{23}$, Δm^2_{32}, $\sin^2\theta_{13}$, and δ_{CP} with the MCMC method described in Sec. VIII B. In contrast with the frequentist analysis presented in Sec. XI A, the Markov chain walks in a parameter space where the sign of Δm^2_{32} can flip, and results are presented for both mass orderings. The best-fit point and $\pm1\sigma$ credible interval for each parameter, obtained with the KDE method, are summarized in Table XXVII. The best-fit point is the mode of the four-dimensional histogram where the axes are the oscillation parameters.

The $\pm1\sigma$ credible intervals, which have a 68.3% probability of containing the true value, are computed, for each parameter, from the posterior probability density marginalized over all the other parameters as shown in Fig. 46. Figure 46 also shows the correlations between the oscillation parameters with the map of the marginal posterior density probability and the credible intervals in the space formed by two parameters.

TABLE XXVII. Best-fit results and the 1σ credible interval of the T2K data fit without the reactor constraint with the MCMC analyses including both mass orderings.

Parameter	Best fit	$\pm1\sigma$
δ_{CP}	-1.815	$[-2.275; -0.628]$
$\sin^2\theta_{13}$	0.0254	[0.0210; 0.0350]
$\sin^2\theta_{23}$	0.513	[0.460; 0.550]
Δm^2_{32}	$2.539\times10^{-3}\,\mathrm{eV}^2/c^4$	$[-2.628; -2.544]\times10^{-3}\,\mathrm{eV}^2/c^4$ $[2.436; 2.652]\times10^{-3}\,\mathrm{eV}^2/c^4$

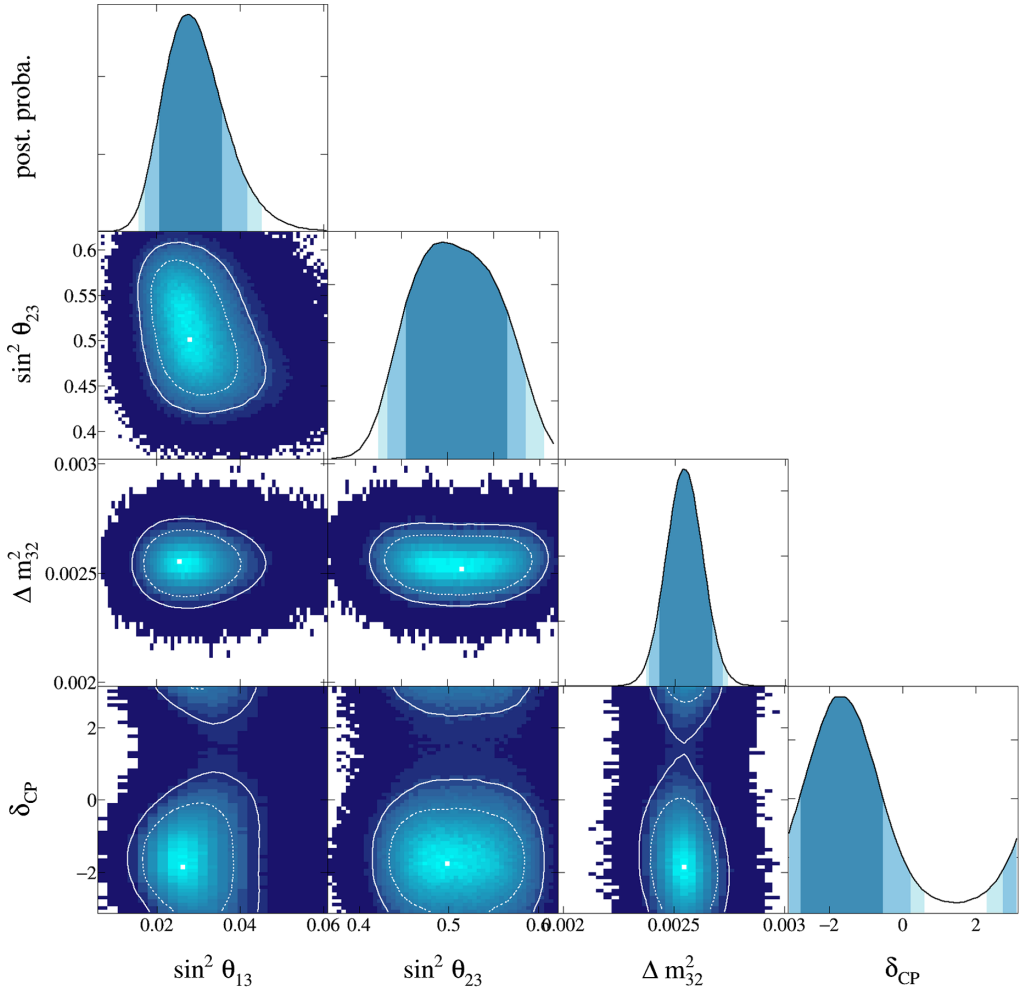

FIG. 46. The two-dimensional histograms represent the marginal posterior probability in the two-parameter space as a blue gradient. The white solid (dashed) line is the 90% (1σ) credible interval. The one-dimensional histograms represent the posterior probability density (post. proba.) of the oscillation parameter in the x axis of the column marginalized over all other parameters. The blue areas are, respectively, the 1σ (dark), 90% (medium), and 95% (light) credible interval.

The proportion of the MCMC points with $\sin^2\theta_{23} > 0.5$ or < 0.5 gives the posterior probability of the octant. Similarly, the relative proportion of steps with $\Delta m^2_{32} >$ or < 0 gives the posterior probability of each mass ordering. They are shown in Table XXVIII. A Bayes factor can be computed as a ratio of the posterior probabilities [89]. The Bayes factor for normal ordering is $B(\mathrm{NH/IH}) = 2.28$; the Bayes factor for the upper octant is $B(\sin^2\theta_{23} > 0.5/\sin^2\theta_{23} < 0.5) = 1.32$. Neither can be considered decisive.

2. Results with reactor constraints

This section presents the results obtained with the MCMC analysis when adding a Gaussian prior on $\sin^2\theta_{13}$ with the value given in Table XVIII. The posterior mode marginalized over the nuisance parameters is given in Table XXIX. Including the reactor prior on $\sin^2\theta_{13}$, the best fit is closer to that obtained by the reactor experiments compared to the T2K-only results. The δ_{CP} best fit is closer to the maximum violating value of $-\pi/2$ due to the correlations with $\sin^2\theta_{13}$ shown in Fig. 46.

The MCMC algorithm uses a flat prior on δ_{CP}, but its dependence on this choice of prior has been tested by computing the credible intervals with a flat prior on $\sin\delta_{CP}$. The two sets of intervals are in reasonable agreement as shown in Fig. 47.

The Bayes factor for the mass ordering and the θ_{23} octant can be computed with the method described in Sec. XI B 1. Using the values from Table XXX, they are found to be $B(\mathrm{NH/IH}) = 3.71$ and $B(\sin^2\theta_{23} > 0.5/\sin^2\theta_{23} < 0.5) = 2.39$, respectively. Also, in this case, these cannot be considered decisive.

C. Comparison among the oscillation analyses

The frequentist likelihood multiplied by Gaussian penalty terms for the nuisance parameters and uniform priors

TABLE XXVIII. Posterior probabilities for the mass orderings and $\sin^2\theta_{23}$ when fitting T2K data only with an MCMC method.

	$\sin^2\theta_{23} < 0.5$	$\sin^2\theta_{23} > 0.5$	Line total
Inverted ordering	0.137	0.168	0.305
Normal ordering	0.294	0.401	0.695
Column total	0.431	0.569	1

TABLE XXIX. Best-fit results and the 1σ credible interval of the T2K data fit with the reactor constraint with the MCMC analyses including both mass orderings.

Parameter	Best fit	$\pm1\sigma$
δ_{CP}	-1.789	$[-2.450; -0.880]$
$\sin^2\theta_{13}$	0.0219	[0.0208; 0.0233]
$\sin^2\theta_{23}$	0.534	[0.490; 0.580]
Δm^2_{32}	2.539×10^{-3} eV$^2/c^4$	$[-3.000;-2.952]\times10^{-3}$ eV$^2/c^4$
		$[2.424; 2.664]\times10^{-3}$ eV$^2/c^4$

for the oscillation parameters is equivalent to the Bayesian posterior density, for the same priors. In order to compare the analyses, the posterior probability densities sampled by the Bayesian analyses are converted into a $\Delta\chi^2$ function, and the intervals are recalculated to extract confidence intervals that are compared with the frequentist analyses. Figure 48 shows the constant $\Delta\chi^2$ 68% and 90% intervals for all three oscillation analyses in the $\sin^2\theta_{13}$-δ_{CP} plane, assuming normal ordering and only using T2K data. Differences exist among the three methods as the 2D templates fitted in the appearance samples are different and the Bayesian analyses do a combined fit of near and far detector samples, but no major differences are found between the contours.

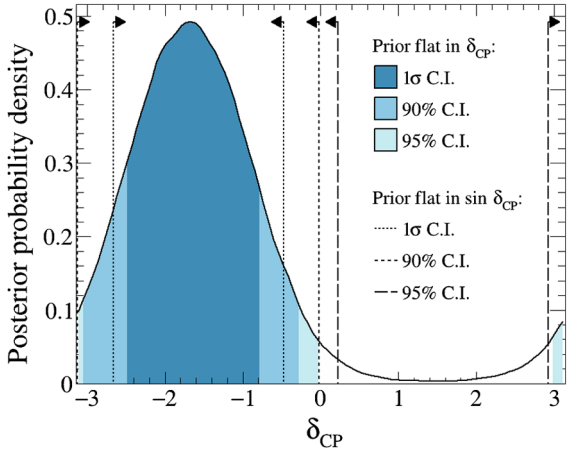

FIG. 47. δ_{CP} marginal posterior probability as obtained with the MCMC method. The credible intervals for $\pm1\sigma$, $\pm90\%$, and $\pm95\%$ are shown when using a flat prior in δ_{CP} (usual fit) and when converting to a flat prior in $\sin\delta_{CP}$.

TABLE XXX. Posterior probabilities for the mass orderings and $\sin^2\theta_{23}$ with an MCMC method when fitting T2K data with the reactor constraint.

	$\sin^2\theta_{23} < 0.5$	$\sin^2\theta_{23} > 0.5$	Line total
Inverted ordering	0.060	0.152	0.212
Normal ordering	0.235	0.553	0.788
Column total	0.295	0.705	1

Figure 49 shows the constant $\Delta\chi^2$ 68% and 90% intervals in the $\sin^2\theta_{23}$-Δm^2_{32} plane for both frequentist and Bayesian fits. Both distributions and intervals agree between fitters, validating the extrapolation of the constraints on the nuisance parameters obtained in the near detector fit to SK.

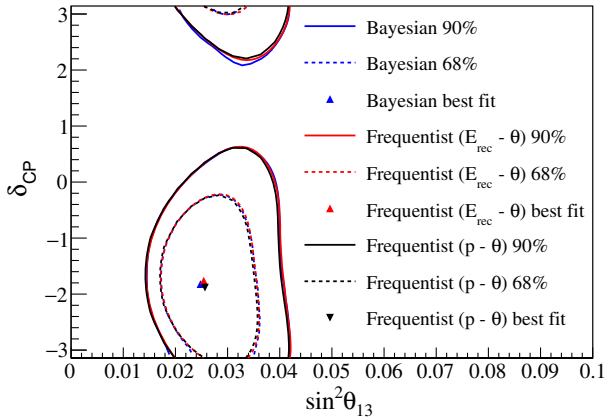

FIG. 48. Constant $\Delta\chi^2$ 68% and 90% intervals in the $\sin^2\theta_{13}$-δ_{CP} plane for both frequentist analyses and the Bayesian fit.

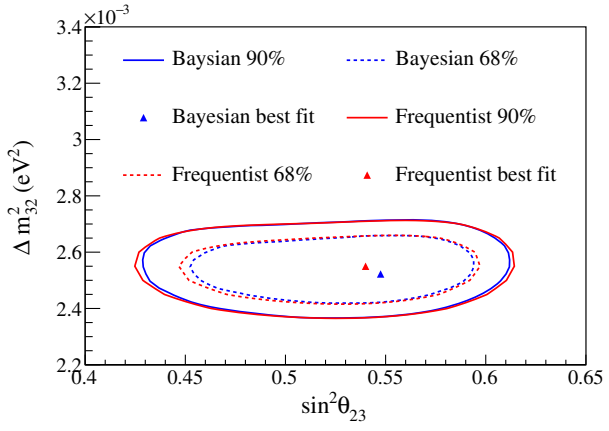

FIG. 49. Constant $\Delta\chi^2$ 68% and 90% intervals in the $\sin^2\theta_{23}$-Δm^2_{32} plane for the frequentist fit which uses 2D $\{E_\nu^{\rm rec}, \theta_{\rm lep}\}$ templates and the Bayesian fit, assuming normal ordering.

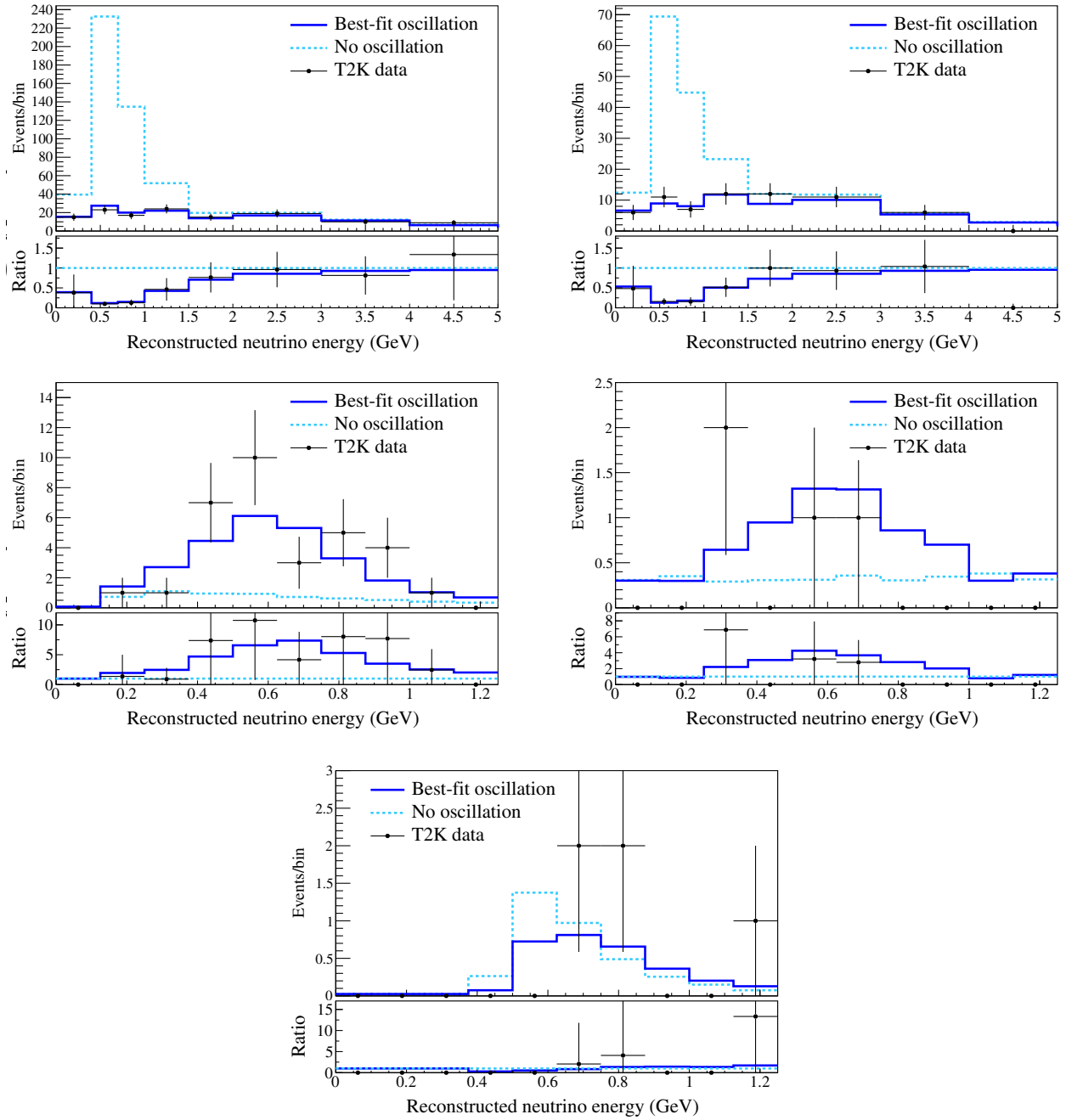

FIG. 50. Comparison of the best-fit oscillated MC energy spectra, unoscillated spectra, and T2K data for the five samples used in the fit: μ-like sample in the ν mode and $\bar{\nu}$ mode (top left and right), single-ring e-like appearance sample in the ν mode and $\bar{\nu}$ mode (middle left and right), and CC1π^+ e-like appearance sample in the ν mode (bottom). The larger unoscillated spectra in the CC1π^+ e-like sample compared to the single-ring sample is due to the relatively large background of ν_μ in the CC1π^+ sample, which does not disappear in the no-oscillation case. The ratio of the best fit to unoscillated spectra are also shown.

D. Best-fit spectra

An estimate of the oscillation parameters Δm^2_{32}, $\sin^2\theta_{13}$, and δ_{CP} has been obtained with both frequentist and Bayesian analyses. The agreement between the fit results and the data has been evaluated by comparing the expected spectra after the oscillation fit with the data points as shown in Fig. 50. The best-fit spectra are obtained by sampling 2000 points from the MCMC including the reactor constraint and fitting a Gaussian distribution to calculate the most probable value for the predicted number of events in each energy bin.

In order to extract the ratio of oscillated to unoscillated spectra, the expected spectra are also tuned to the no

oscillation case. A coarser binning than the one used in the fit has been used for readability.

XII. CONCLUSIONS

All data collected by the T2K experiment between 2010 and 2016 have been analyzed to estimate the oscillation parameters $|\Delta m^2_{32}|$, $\sin^2\theta_{23}$, $\sin^2\theta_{13}$, δ_{CP} and the mass ordering. These parameters are estimated by doing a joint fit of the ν_μ- and $\bar{\nu}_\mu$-disappearance channels and ν_e- and $\bar{\nu}_e$-appearance channels by using five samples selected at the far detector, thus including the new additional CC1π^+ sample. The data related to this measurement can be found in Ref. [90]. A comprehensive study has been performed to evaluate the sensitivity of oscillation parameter estimates to neutrino interaction modeling, showing that the impact of these uncertainties is small compared to the total uncertainties on the measurement of all the oscillation parameters.

The general approach followed in this paper, which combines separate analyses of beamline, neutrino interactions, near and far detector selections through sets of systematic parameters, and their covariances will be extended with additional data which will be collected by T2K in the coming years in both the ν and $\bar{\nu}$ modes and improved near and far detector samples. This is expected to greatly enhance the sensitivity of the T2K experiment to the measurement of the CP-violation phase δ_{CP} as well as more precise measurements of the atmospheric parameters $|\Delta m^2_{32}|$ and $\sin^2\theta_{23}$.

ACKNOWLEDGMENTS

We thank the J-PARC staff for superb accelerator performance. We thank the CERN NA61/SHINE Collaboration for providing valuable particle production data. We acknowledge the support of MEXT, Japan; NSERC (Grant No. SAPPJ-2014-00031), NRC and CFI, Canada; CEA and CNRS/IN2P3, France; DFG, Germany; INFN, Italy; National Science Centre (NCN) and Ministry of Science and Higher Education, Poland; RSF, RFBR, and MES, Russia; MINECO and ERDF funds, Spain; SNSF and SERI, Switzerland; STFC, UK; and DOE, USA. We also thank CERN for the UA1/NOMAD magnet, DESY for the HERA-B magnet mover system, NII for SINET4, the WestGrid and SciNet consortia in Compute Canada, and GridPP and the Emerald High Performance Computing facility in the United Kingdom. In addition, participation of individual researchers and institutions has been further supported by funds from ERC (FP7), H2020 Grant No. RISE-GA644294-JENNIFER, EU; JSPS, Japan; Royal Society, UK; and the Alfred P. Sloan Foundation and the DOE Early Career program, USA.

[1] Y. Fukuda *et al.*, Evidence for Oscillation of Atmospheric Neutrinos, Phys. Rev. Lett. **81**, 1562 (1998).
[2] Q. R. Ahmad *et al.*, Direct Evidence for Neutrino Flavor Transformation from Neutral Current Interactions in the Sudbury Neutrino Observatory, Phys. Rev. Lett. **89**, 011301 (2002).
[3] M. H. Ahn *et al.*, Measurement of neutrino oscillation by the K2K experiment, Phys. Rev. D **74**, 072003 (2006).
[4] P. Adamson *et al.*, Combined Analysis of ν_μ Disappearance and $\nu_\mu \to \nu_e$ Appearance in MINOS using Accelerator and Atmospheric Neutrinos, Phys. Rev. Lett. **112**, 191801 (2014).
[5] K. Eguchi *et al.*, First Results from KamLAND: Evidence for Reactor Anti-Neutrino Disappearance, Phys. Rev. Lett. **90**, 021802 (2003).
[6] K. Abe *et al.*, Indication of Electron Neutrino Appearance from an Accelerator-produced Off-axis Muon Neutrino Beam, Phys. Rev. Lett. **107**, 041801 (2011).
[7] K. Abe *et al.*, Observation of Electron Neutrino Appearance in a Muon Neutrino Beam, Phys. Rev. Lett. **112**, 061802 (2014).
[8] F. P. An *et al.*, Observation of Electron-Antineutrino Disappearance at Daya Bay, Phys. Rev. Lett. **108**, 171803 (2012).
[9] Soo-Bong Kim *et al.*, Observation of Reactor Electron Antineutrino Disappearance in the RENO Experiment, Phys. Rev. Lett. **108**, 191802 (2012).
[10] Y. Abe *et al.*, Indication for the Disappearance of Reactor Electron Antineutrinos in the Double Chooz Experiment, Phys. Rev. Lett. **108**, 131801 (2012).
[11] P. Adamson *et al.*, First Measurement of Electron Neutrino Appearance in NOvA, Phys. Rev. Lett. **116**, 151806 (2016).
[12] K. Abe *et al.*, Combined Analysis of Neutrino and Antineutrino Oscillations at T2K, Phys. Rev. Lett. **118**, 151801 (2017).
[13] T. Sekiguchi *et al.*, Development and operational experience of magnetic horn system for T2K experiment, Nucl. Instrum. Methods Phys. Res., Sect. A **789**, 57 (2015).
[14] K. Suzuki *et al.*, Measurement of the muon beam direction and muon flux for the T2K neutrino experiment, Prog. Theor. Exp. Phys. **2015**, 53C01 (2015).
[15] K. Abe *et al.*, The T2K experiment, Nucl. Instrum. Methods Phys. Res., Sect. A **659**, 106 (2011).
[16] K. Abe *et al.*, T2K neutrino flux prediction, Phys. Rev. D **87**, 012001 (2013).
[17] A. Ferrari, P. R. Sala, A. Fasso, and J. Ranft, Report Nos. CERN-2005-010, SLAC-R-773, INFN-TC-05-11.

[18] T. T. Bohlen, F. Cerutti, M. P. W. Chin, A. Fasso, A. Ferrari, P. G. Ortega, A. Mairani, P. R. Sala, G. Smirnov, and V. Vlachoudis, The FLUKA Code: Developments and challenges for high energy and medical applications, Nucl. Data Sheets **120**, 211 (2014).

[19] N Abgrall *et al.*, Measurements of cross sections and charged pion spectra in proton-carbon interactions at 31 GeV/c, Phys. Rev. C **84**, 034604 (2011).

[20] N. Abgrall *et al.*, Measurement of production properties of positively charged kaons in proton-carbon interactions at 31 GeV/c, Phys. Rev. C **85**, 035210 (2012).

[21] N. Abgrall *et al.*, Measurements of $\pi^{\pm}$, $K^{\pm}$, K^0_S, Λ and proton production in proton-carbon interactions at 31 GeV/c with the NA61/SHINE spectrometer at the CERN SPS, Eur. Phys. J. C **76**, 84 (2016).

[22] T. Eichten *et al.*, Particle production in proton interactions in nuclei at 24 GeV/c, Nucl. Phys. **B44**, 333 (1972).

[23] J. V. Allaby *et al.*, CERN Technical Report 70-12, 1970.

[24] I. Chemakin *et al.*, Pion production by protons on a thin beryllium target at 6.4-Ge, 12.3-GeV/c, and 17.5-GeV/c incident proton momenta, Phys. Rev. C **77**, 015209 (2008).

[25] R. Brun, F. Carminati, and S. Giani CERN-W5013, 1994.

[26] C. Zeitnitz and T. A. Gabriel, in *Proceedings of International Conference on Calorimetry in High Energy Physics* (World Scientific, Corpus Christi, Texas, 1992), ISBN:9789810213039, pp. 394–404.

[27] K. Abe *et al.*, Measurements of neutrino oscillation in appearance and disappearance channels by the T2K experiment with 6.6E20 protons on target, Phys. Rev. D **91**, 072010 (2015).

[28] Y. Hayato, A neutrino interaction simulation program library NEUT, Acta Phys. Pol. B **40**, 2477 (2009).

[29] A. M. Ankowski and C. Mariani, Systematic uncertainties in long-baseline neutrino-oscillation experiments, J. Phys. G **44**, 054001 (2017).

[30] M. Martini, M. Ericson, and G. Chanfray, Neutrino energy reconstruction problems and neutrino oscillations, Phys. Rev. D **85**, 093012 (2012).

[31] J. Nieves, F. Sanchez, I. Ruiz Simo, and M. J. Vicente Vacas, Neutrino energy reconstruction and the shape of the CCQE-like total cross section, Phys. Rev. D **85**, 113008 (2012).

[32] P. Coloma and P. Huber, Impact of Nuclear Effects on the Extraction of Neutrino Oscillation Parameters, Phys. Rev. Lett. **111**, 221802 (2013).

[33] A. M. Ankowski, O. Benhar, P. Coloma, P. Huber, C.-M. Jen, C. Mariani, D. Meloni, and E. Vagnoni, Comparison of the calorimetric and kinematic methods of neutrino energy reconstruction in disappearance experiments, Phys. Rev. D **92**, 073014 (2015).

[34] O. Lalakulich, U. Mosel, and K. Gallmeister, Energy reconstruction in quasielastic scattering in the MiniBooNE and T2K experiments, Phys. Rev. C **86**, 054606 (2012).

[35] C. Wilkinson *et al.*, Testing charged current quasi-elastic and multinucleon interaction models in the NEUT neutrino interaction generator with published data sets from the MiniBooNE and MINERνA experiments, Phys. Rev. D **93**, 072010 (2016).

[36] C. H. Llewellyn Smith, Neutrino reactions at accelerator energies, Phys. Rep. **3**, 261 (1972).

[37] R. Bradford, A. Bodek, H. Budd, and J. Arrington, A new parameterization of the nucleon elastic form factors, Nucl. Phys. **B159**, 127 (2006).

[38] E. J. Moniz and R. A. Smith, Neutrino reactions on nuclear targets, Nucl. Phys. **B101**, 605 (1972).

[39] O. Benhar and A. Fabrocini, Two nucleon spectral function in infinite nuclear matter, Phys. Rev. C **62**, 034304 (2000).

[40] J. Nieves, I. Ruiz Simo, and M. J. Vicente Vacas, Inclusive charged–current neutrino–nucleus reactions, Phys. Rev. C **83**, 045501 (2011).

[41] R. Gran, J. Nieves, F. Sanchez, and M. J. Vicente Vacas, Neutrino-nucleus quasi-elastic and 2p2h interactions up to 10 GeV, Phys. Rev. D **88**, 113007 (2013).

[42] A. A. Aguilar-Arevalo *et al.*, First measurement of the muon neutrino charged current quasielastic double-differential cross section, Phys. Rev. D **81**, 092005 (2010).

[43] A. A. Aguilar-Arevalo *et al.*, First measurement of the muon antineutrino double-differential charged current quasi-elastic cross section, Phys. Rev. D **88**, 032001 (2013).

[44] G. A. Fiorentini *et al.*, Measurement of Muon Neutrino Quasi-Elastic Scattering on a Hydrocarbon Target at $E_\nu \sim 3.5$ GeV, Phys. Rev. Lett. **111**, 022502 (2013).

[45] L. Fields *et al.*, Measurement of Muon Antineutrino Quasi-Elastic Scattering on a Hydrocarbon Target at $E_\nu \sim 3.5$ GeV, Phys. Rev. Lett. **111**, 022501 (2013).

[46] D. Rein and L. M. Sehgal, Neutrino-excitation of baryon resonances and single pion production, Ann. Phys. (N.Y.) **133**, 79 (1981).

[47] K. M. Graczyk and J. T. Sobczyk, Form factors in the quark resonance model, Phys. Rev. D **77**, 053001 (2008).

[48] G. M. Radecky *et al.*, Study of single pion production by weak charged currents in low-energy neutrino d interactions, Phys. Rev. D **25**, 1161 (1982).

[49] T. Kitagaki *et al.*, Charged current exclusive pion production in neutrino deuterium interactions, Phys. Rev. D **34**, 2554 (1986).

[50] C. Wilkinson, P. Rodrigues, S. Cartwright, L. Thompson, and K. S. McFarland, Reanalysis of bubble chamber measurements of muon-neutrino induced single pion production, Phys. Rev. D **90**, 112017 (2014).

[51] A. A. Aguilar-Arevalo *et al.*, Measurement of ν_μ and $\bar{\nu}_\mu$ induced neutral current single π^0 production cross sections on mineral oil at $E_\nu \sim \mathrm{O}(1\ \mathrm{GeV})$, Phys. Rev. D **81**, 013005 (2010).

[52] A. A. Aguilar-Arevalo *et al.*, Measurement of ν_μ-induced charged-current neutral pion production cross sections on mineral oil at $E_\nu \in 0.5$–2.0 GeV, Phys. Rev. D **83**, 052009 (2011).

[53] A. A. Aguilar-Arevalo *et al.*, Measurement of neutrino-induced charged-current charged pion production cross sections on mineral oil at $E_\nu \sim 1$ GeV, Phys. Rev. D **83**, 052007 (2011).

[54] B. Eberly *et al.*, Charged pion production in ν_μ interactions on hydrocarbon at $\langle E_\nu \rangle = 4.0$ GeV, Phys. Rev. D **92**, 092008 (2015).

[55] Y. Kurimoto *et al.*, Measurement of inclusive neutral current neutral pion production on carbon in a few-GeV neutrino beam, Phys. Rev. D **81**, 033004 (2010).

[56] S. Nakayama, Measurement of single π^0 production in neutral current neutrino interactions with water by a 1.3-GeV wide band muon neutrino beam, Phys. Lett. B **619**, 255 (2005).
[57] D. Rein and L. M. Sehgal, Coherent π^0 production in neutrino reactions, Nucl. Phys. **B223**, 29 (1983).
[58] D. Rein and L. M. Sehgal, PCAC and the deficit of forward muons in π^+ production by neutrinos, Phys. Lett. B **657**, 207 (2007).
[59] A. Higuera *et al.*, Measurement of Coherent Production of $\pi^{\pm}$ in Neutrino and Antineutrino Beams on Carbon from E_{ν} of 1.5 to 20 GeV, Phys. Rev. Lett. **113**, 261802 (2014).
[60] Ch. Berger and L. M. Sehgal, PCAC and coherent pion production by low energy neutrinos, Phys. Rev. D **79**, 053003 (2009).
[61] M. Glück, E. Reya, and A. Vogt, Dynamical parton distributions revisited, Eur. Phys. J. C **5**, 461 (1998).
[62] A. Bodek and U. K. Yang, Modeling neutrino and electron scattering cross sections in the few-GeV region with effective LO PDFs, AIP Conf. Proc. **670**, 110 (2003).
[63] T. Sjstrand, High-energy-physics event generation with PYTHIA 5.7 and JETSET 7.4, Comput. Phys. Commun. **82**, 74 (1994).
[64] P. Adamson *et al.*, Neutrino and antineutrino inclusive charged-current cross section measurements with the MINOS near detector, Phys. Rev. D **81**, 072002 (2010).
[65] E. Wang, L. Alvarez-Ruso, Y. Hayato, K. Mahn, and J. Nieves, Photon emission in neutral current interactions at the T2K experiment, Phys. Rev. D **92**, 053005 (2015).
[66] E. Wang, L. Alvarez-Ruso, and J. Nieves, Photon emission in neutral current interactions at intermediate energies, Phys. Rev. C **89**, 015503 (2014).
[67] R. D. Woods and D. S. Saxon, Diffuse surface optical model for nucleon-nuclei scattering, Phys. Rev. **95**, 577 (1954).
[68] D. S. Baranov *et al.*, Measurements of the $\nu_{\mu}N$ total cross section at 2-GeV–30-GeV in SKAT neutrino experiment, Phys. Lett. **81B**, 255 (1979).
[69] M. Day and K. S. McFarland, Differences in quasi-elastic cross sections of muon and electron neutrinos, Phys. Rev. D **86**, 053003 (2012).
[70] M. Martini, M. Ericson, and G. Chanfray, Neutrino quasielastic interaction and nuclear dynamics, Phys. Rev. C **84**, 055502 (2011).
[71] K. Abe *et al.*, Measurements of the T2K neutrino beam properties using the INGRID on-axis near detector, Nucl. Instrum. Methods Phys. Res., Sect. A **694**, 211 (2012).
[72] N. Abgrall *et al.*, Time projection chambers for the T2K near detectors, Nucl. Instrum. Methods Phys. Res., Sect. A **637**, 25 (2011).
[73] P. A. Amaudruz *et al.*, The T2K fine-grained detectors, Nucl. Instrum. Methods Phys. Res., Sect. A **696**, 1 (2012).
[74] S. Fukuda *et al.*, The Super-Kamiokande detector, Nucl. Instrum. Methods Phys. Res., Sect. A **501**, 418 (2003).
[75] K. A. Olive *et al.*, Review of particle physics, Chin. Phys. C **38**, 090001 (2014) and 2015 update.
[76] Z. Maki, M. Nakagawa, and S. Sakata, Remarks on the unified model of elementary particles, Prog. Theor. Phys. **28**, 870 (1962).
[77] B. Pontecorvo, Neutrino experiments and the problem of conservation of leptonic charge, Zh. Eksp. Teor. Fiz. **53**, 1717 (1967) [Sov. Phys. JETP **26**, 984 (1968)].
[78] J. Arafune, M. Koike, and J. Sato, *CP* violation and matter effect in long baseline neutrino oscillation experiments, Phys. Rev. D **56**, 3093 (1997); Erratum, Phys. Rev. D **60**, 119905(E) (1999).
[79] R. D. Cousins and V. L. Highland, Incorporating systematic uncertainties into an upper limit, Nucl. Instrum. Methods Phys. Res., Sect. A **320**, 331 (1992).
[80] G. J. Feldman and R. D. Cousins, Unified approach to the classical statistical analysis of small signals, Phys. Rev. D **57**, 3873 (1998).
[81] W. K. Hastings, Monte Carlo sampling methods using Markov chains and their applications, Biometrika **57**, 97 (1970).
[82] P. Mills, Efficient statistical classification of satellite measurements, International Journal of Remote Sensing **32**, 6109 (2011).
[83] K. Cranmer, Kernel estimation in high-energy physics, Comput. Phys. Commun. **136**, 198 (2001).
[84] F. James and M. Roos, Minuit—A system for function minimization and analysis of the parameter errors and correlations, Comput. Phys. Commun. **10**, 343 (1975).
[85] L. Demortier, P values and nuisance parameters, 2008.
[86] P. Adamson *et al.* (unpublished).
[87] R. Wendell, Atmospheric Neutrino Oscillations at Super-Kamiokande, *Proc. Sci.*, ICRC2015 (2016) 1062.
[88] M. G. Aartsen *et al.*, Neutrino oscillation studies with IceCube-DeepCore, Nucl. Phys. **B908**, 161 (2016).
[89] H. Jeffreys, *The Theory of Probability* (Oxford University, New York, 1998).
[90] K. Abe *et al.*, T2K public data, http://t2k-experiment.org/results/2016-nu-nubar-oa-longpaper/.